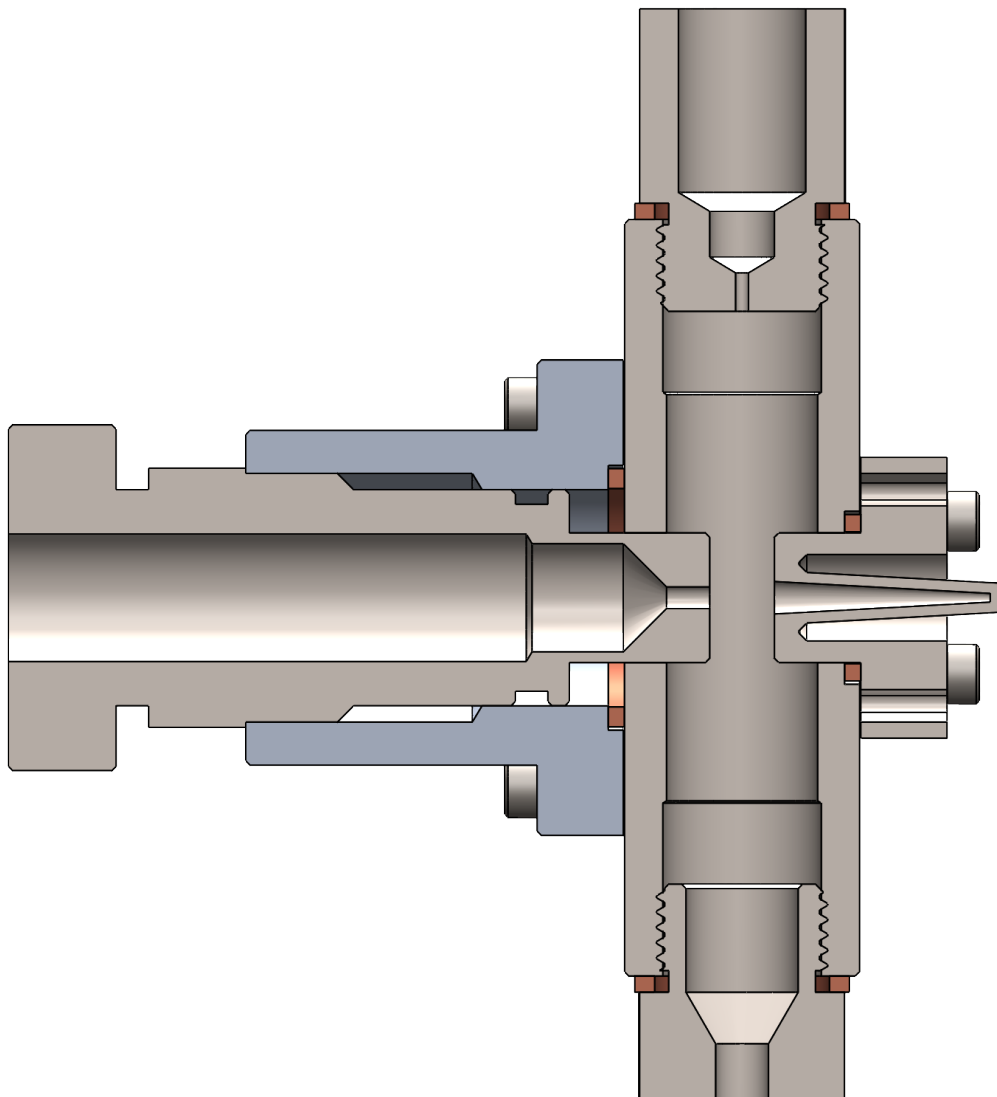


Development of a Non-Pre-Mixed GOx/Methane Resonance Igniter

Experimental Analysis and Computational
Modelling

Jonathan Neeser



Development of a Non-Pre-Mixed GOx/Methane Resonance Igniter

Experimental Analysis and Computational
Modelling

by

Jonathan Neeser

to obtain the degree of Master of Science

at the Delft University of Technology,

to be defended publicly on Tuesday September 24, 2024 at 9:00 AM.

Student number: 4657551
Project duration: October 2023 – September 2024
Thesis committee: Dr. F. De Domenico, TU Delft, Supervisor
Dr. M. Pini, TU Delft, Chair
Dr. A. Cervone, TU Delft, Examiner

An electronic version of this thesis is available at <http://repository.tudelft.nl/>.

Preface

This thesis marks the culmination of seven years of studying at TU Delft. Probably the most significant impact on me and on my work as an engineer was the time I spent as part of Delft Aerospace Rocket Engineering (DARE). I had the chance to work on the development of several liquid propellant rocket engines, support rocket launches and be part of many engine tests. Every successful test, or painstaking forensic analysis of a debris field, is a fantastic opportunity to learn and to improve as an engineer. I doubt that any of the practical work performed as part of this thesis would have been possible without it. I have come to appreciate DARE as a place, that challenged me to explore many different aspects of engineering and where learning from failures is possible. Throughout my time in DARE I have seen a shift towards a more open and collaborative environment within student rocketry. I hope to see this trend continue for a long time to come, producing a generation of rocket engineers that support open source projects and international cooperation.

First of all I would like to thank my thesis supervisor, Francesca for her guidance and support throughout this project. I greatly appreciate her enthusiasm for the project and for helping me focus my research, while giving me the freedom to explore a topic I am deeply interested in.

I would like to thank Thomas and AGF Machining Solutions Inc. for kindly manufacturing several resonators and test prints for this project. Thomas provided valuable advice on metal additive manufacturing and helped with the design of the printed parts.

I would also like to thank all of the wonderful people from DARE who helped me during the three test campaigns with this resonance igniter. Despite long, exhausting days, and sometimes terrible weather, they came to help. Special thanks go to Nick, Miguel, Sari, Dionysios, Nathaniel, Leo, Roderick and Jan. Without them, none of these tests would have been possible. Special thanks also goes to Nathaniel and Lasse for their input on the project and for all of the interesting discussions that helped raise the quality of my work.

I would also like to thank the staff of TU Delft that helped me during this thesis. In particular, the Gas Team for their help with transporting gas cylinders and lending me several gas regulators and Johan Bijleveld for his support when manufacturing parts for the igniter and test bench.

Finally, I would like to thank Aida, my partner, for her continued support and for maintaining my sanity throughout this project. She was there to help with every test campaign and translated two Japanese research papers, that were very important to this study. This thesis would have been significantly harder without the support and encouragement of my parents, my brother and my friends.

*Jonathan Neeser
Delft, September 2024*

Summary

The objective of this thesis is to investigate the performance envelope of a non-pre-mixed oxygen / methane resonance igniter experimentally, and develop a numerical model capable of predicting the operating mode of the igniter based on nozzle gap spacing and operational parameters. Resonance igniters can provide a simple and effective ignition system for liquid propellant rocket engines. Instead of using a separate ignition source, such as a glow or spark plug, these igniters rely on acoustic resonance to generate enough heat to initiate combustion. This not only simplifies the ignition system but extends the possible number of ignition cycles. In recent years the development of in-space propulsion systems has increasingly shifted towards rocket propellants that can replace the highly toxic hydrazine-derivatives currently in widespread use. Many of the proposed alternatives require external ignition sources, leading to the need for light-weight, highly reliable ignition systems capable of a high number of ignition cycles. Despite the advantages of resonance igniters, none have been used as flight hardware as part of a launch vehicle or in-space propulsion system.

In this thesis a resonance igniter is designed and tested using non-pre-mixed gaseous oxygen and methane as propellants. Extensive thermo-acoustic heating experiments are performed using both oxygen and nitrogen as driving gases. Several parametric sweeps over different nozzle gap distances are conducted, to investigate the switch between different operating modes of thermo-acoustic interaction. The jet regurgitant mode is characterised by flow oscillations at the natural frequency of the acoustic cavity and produces intense heating at the cavity tip. The much higher frequency jet screech mode is shown not to produce significant resonance heating in this study. A total of 95 resonance heating tests are performed and analysed.

The switch from the jet screech mode to the regurgitant mode is observed near the first shock structure of the under expanded jet. The highest rates of resonance heating is found at $s/d_{throat} = 3$ for nitrogen and $s/d_{throat} = 2.75$ for oxygen at a nozzle pressure ratio of 6.8 and 6.4, respectively. With a pressure ratio of 7, the optimum point for oxygen shifts to $s/d_{throat} = 3$. The use of a choked exhaust nozzle serves to stabilise the resonance heating with respect to increasing upstream pressure, by maintaining a near constant nozzle pressure ratio. This is demonstrated to be effective between 14 bar and 23 bar, with increasing back pressure consistently resulting in higher rates of thermo-acoustic heating. The use of a conical resonance cavity inlet is shown to delay the onset of the jet regurgitant mode, compared to a cylindrical, blunt inlet.

Six non-pre-mixed combustion experiments are performed in this study. The flow failed to ignite during every test, despite achieving favourable mixture ratios in the combustion chamber and temperatures in excess of $470^{\circ}C$ at the outer wall of the resonator. Frequency data from these experiments shows that the injection of methane into the combustion chamber destabilises the ongoing resonance and causes rapid cooling of the resonator tip.

A two dimensional, non-ideal, compressible, URANS simulation of the flow inside the resonance cavity is presented, using the Open Source CFD software SU2. Simulation cases are run for the same nozzle gap distances and driving gases used in the parametric sweeps. These are used to validate the simulation against the experimental results. A comparison of the predicted fundamental frequency of the cavity and its overtones shows close agreement between the simulations and experiments. The simulation is shown to be capable of predicting the switch in operating mode of the igniter over two different resonator inlet shapes. The set points resulting in the highest rates of acoustic heating are predicted by this simulation when using nitrogen as the driving gas. The resonance frequency, predicted by the simulation, for each set point differs by less than 10% (and as low as 2.6%) from experimental results. The comparatively low computational cost of the simulation lends itself to CFD based design optimisation or to use as part of the design process of a resonance igniter.

Contents

Preface	i
Summary	ii
Nomenclature	vi
1 Introduction	1
1.1 The Move Towards Green Propellants	2
1.2 Rocket Engine Ignition Systems	2
1.3 Report Structure	3
2 Theoretical Background	4
2.1 Jet Driven Acoustic Resonance	4
2.2 Operating Modes	6
2.2.1 Jet Instability Mode	6
2.2.2 Jet Regurgitant Mode	7
2.2.3 Jet Screech Mode	8
2.2.4 Switch Between Operating Modes	9
2.3 Shock Tube Analogy	10
2.4 Energy Balance and Loss Accounting	13
2.4.1 Heating over a Normal Shock	14
2.4.2 Friction	15
2.4.3 Heat Loss to the Cavity Walls	15
2.4.4 Entrainment Loss	16
2.5 Thermo-Acoustic Igniter Design	16
2.6 Parameters Influencing Acoustic Resonance	17
2.6.1 Driving Gas	17
2.6.2 Nozzle Gap Spacing and NPR	18
2.6.3 Non-Dimensional Cavity Length	20
2.6.4 Resonator Inlet Diameter	21
2.6.5 Cavity Shape	22
2.7 Resonance Ignition	22
2.7.1 Propellant Mixing	22
2.7.2 Ignition Characteristics of Methane	23
2.8 Numerical Models of Resonance Heating	24
2.8.1 Zero-Dimensional Models	24
2.8.2 One-Dimensional Models	24
2.8.3 Multi-Dimensional Euler Models	25
2.8.4 Multi-Dimensional RANS Models	25
2.9 Numerical Discretisation	26
2.9.1 Spatial Discretisation and Convective Schemes	26
2.9.2 Time Discretisation	27
3 Research Objectives	28
3.1 Research Gap	28
3.2 Research Objectives	29
3.3 Research Questions	29
4 Experimental Approach and Simulation	31
4.1 Experimental Approach	31
4.2 Numerical Approach	32

5	Thesis Paper	34
5.1	Introduction	34
5.2	Thermo-acoustic Resonance	35
5.2.1	Inlet and Exhaust Nozzles	36
5.2.2	Fuel Injection and Ignition	37
5.3	Thermo-Acoustic Igniter Design	37
5.3.1	Igniter Design	37
5.3.2	Resonator	39
5.3.3	Modified Resonator Inlet Geometry	39
5.3.4	Resonance Frequency	40
5.3.5	Chamber Natural Frequencies and Secondary Resonance	41
5.3.6	Propellant Feed System	41
5.3.7	Sensors and Data Acquisition	42
5.4	Simulation Setup	43
5.4.1	Simulation Domain and Boundary Conditions	43
5.4.2	Time Scales	44
5.4.3	Solver Setup	44
5.4.4	Gas Model	45
5.4.5	Mesh Refinement Study	46
5.4.6	Simulation Cases	47
5.5	Experimental Method	47
5.5.1	Resonance Heating Experiments	47
5.5.2	Combustion Experiments	48
5.6	Resonance Heating Results	49
5.6.1	Description of Operating Modes	49
5.6.2	Switch Between Operating Modes	50
5.6.3	Experimental Validation of Numerical Model	52
5.6.4	Tip Temperature and Heat Flux	54
5.6.5	Effect of Upstream Pressure	56
5.6.6	Effect of Inlet Geometry	58
5.7	Non-Pre-Mixed Ignition Tests	59
5.7.1	Temperature Profile and Decay of Resonance	59
5.7.2	Mixture Ratio	60
5.8	Conclusion	61
6	Conclusions	63
7	Recommendations	65
7.1	Thermo-Acoustic Heating Experiments	65
7.2	Pre-Mixed Operation	65
7.3	Instrumentation	66
7.4	Numerical Model	66
A	Igniter Requirements	67
A.1	Safety Requirements	67
A.2	Design Requirements	68
A.3	Sensor Requirements	68
B	Additional Validation Cases	69
B.1	Shock Tube Model	69
B.2	Validation Against Shock Tube Model	70
B.3	Conical Inlet Geometry	72
C	Experimental Results	74
C.1	Data Acquisition Module	74
C.2	Thermocouple Response Time Correction	74
C.3	Estimating Inner Wall Temperature	75
C.4	Shifting Natural Frequency with Tip Temperature	76
C.5	Pressure Measurements During Combustion Tests	77

C.6	Temperature Measurements	78
C.7	Test Setup and Sensor Placement	79
D	Numerical Results	81
D.1	Mesh Parameters and Convergence	81
D.2	Additional Simulation Results	82
D.3	Time Scales for Conjugate Heat Transfer Simulations	84
E	Manufacturing and Technical Drawings	87
E.1	Critical Dimensions and Manufacturing Tolerance	87
E.2	Drawings	88
F	Risk Assessment	97
F.1	Igniter Design and Safety	97
F.2	Risk Maps	98
G	Test Procedures	102

List of Figures

2.1	Overview of critical parameters for thermo-acoustic heating.	4
2.2	Schlieren images of under-expanded jets at different NPR. Taken from Samsam-Khayani et al. [18]	5
2.3	Illustrations of under-expanded jet flows, taken from Duronio, Villante, and Vita [19]	6
2.4	Illustration of the four phases of a jet regurgitant mode. A shock wave is denoted as a thick blue line, expansion waves as a set of dashed red lines. A solid arrow indicates flow direction, while a dashed arrow shows the movement of a shock wave. (1) shows the inflow phase, (2) and (3) show the two transitional phases and (4) the end of the outflow phase.	7
2.5	Illustration of resonating flow during the jet screech mode. Pressure waves are denoted as solid blue lines. A solid arrow indicates flow direction, while a dashed arrow shows the movement of a pressure wave. (1) and (2) show several pressure waves moving in different directions simultaneously. The Mach disk is close to the cavity entrance and moves very little during the cycles of entering and reflected pressure waves.	9
2.6	Simplified diagram of a shock tube and flow pattern. The blue line indicates the location of the shock wave over time, with the red line describing the interface between the gas in the left and right chamber.	11
2.7	Figure taken from Thompson [30]. Illustration of time dependent velocity inside the resonance cavity. The incident and reflected shock wave is indicated as a thick black line, with expansion waves indicated as thin lines.	12
2.8	Illustration of temperature, pressure and particle velocity inside a shock tube. Note that both p and T in reality are closely linked and do not have the same value, as indicated in this figure. The sign of the velocity indicates if the velocity vector is pointed in positive or negative x -direction. Solid, blue, lines indicate the inflow phase, while dashed, red, lines indicate the outflow phase.	13
2.9	Temperature-entropy diagram of the entrained gas in JRM. The flow is modelled as a shock tube, with NPR = 6, using oxygen at an inlet pressure of 10 bar.	14
2.10	Pre-mixed igniter configuration, taken from Marchan [28]. (1) denotes the injector and (2) the resonance cavity.	16
2.11	Non-pre-mixed igniter configuration, taken from Marchan [28]. (1) denotes the oxygen injector, (2) the resonance cavity and (3) the combustion chamber.	17
2.12	A comparison of highest attained gas temperatures with different driving gases. Oxygen is not shown here, but is expected to perform similarly to nitrogen, being a diatomic gas with similar molecular weight. Taken from E. Rakowsky [35]	18
2.13	Sound pressure level measurements as a function of s/d_{throat} and NPR. The white areas denote spacing at which resonance was observed, with the black vertical lines indicating the expected length of shock structures X_s . Taken from Sarpotdar, Raman, and Cain [23]	19
2.14	Comparison of nozzle gap spacing and NPR associated with high tip temperatures, taken from Bauer et al. [12], Bouch & Cutler [25] and Phillips & Pavli [33]. The green area represents the region, in which JRM has been identified as dominant, by Sarohia & Back [21]. The length of the first and second shock structure are determined using Equation 5.1.	20
2.15	Comparison of heating performance for different cavity lengths, taken from Phillips and Pavli [33]. The cavity lengths tested here are equivalent to $L/d_{throat} = 9.37, 19.06, 27.5$ and 37.18	21
2.16	Heating performance in a cylindrical cavity compared to an equivalent cavity with a 3° half angle. Taken from Phillips and Pavli [33]	22
2.17	Adiabatic flame temperature of O_2/CH_4 as a function of oxidiser to fuel ratio, calculated under frozen equilibrium conditions at a pressure of 10 bar.	23

2.18 Comparison of the pressure evolution of 2D and 3D URANS simulations, taken from Bauer and Haidn [50]	26
4.1 Overview of the test setup developed as part of this thesis.	32
4.2 Simulated Mach number during the inflow cycle of JRM (above), with visualisation of the computational grid at 50% of the nominal number of nodes (below).	32
5.1 Illustration of the structure of the shock structure of a single cell in an under-expanded jet at $4 < \text{NPR} < 7$. Based on the description by Duronio, Villante, and Vita [19]. X_m denotes the distance between the nozzle exit and the Mach disk and X_c the distance to the end of the first shock cell.	36
5.2 Section View of the igniter assembly, (1) oxygen injector support, (2) oxygen injector, (3) combustion chamber, (4) resonator, (5) methane injector, (6) exhaust nozzle.	38
5.3 Microscope images of SLM printed resonance cavity.	39
5.4 Comparison between the conical (left) and cylindrical resonator (right).	40
5.5 Temperature dependent quarter wave frequencies of a truncated cone for the given resonator dimensions using oxygen and nitrogen.	41
5.6 P&ID of the fluid system for combustion tests. Note that for heating tests the line to the methane cylinder is removed.	42
5.7 Critical mesh regions and boundary conditions.	43
5.8 Non-ideal gas effects for conditions in the resonator cavity.	45
5.9 Mesh verification	47
5.10 Processing of microphone data for heating test results.	48
5.11 Processing of pressure and temperature data for ignition attempts.	49
5.12 Simulated flow cycle in JRM, showing density and velocity stream lines, taken at $s/d_{throat} = 3.25$ and $\text{NPR} = 6.8$. (1) shows the beginning of the inflow phase with a shock wave moving into the resonance cavity. (2) and (3) show the transitional phases, as first the reflected shock wave leaves, followed by the mach disk reaching its closest point to the nozzle. (4) shows the end of the outflow phase, just before the start of the next flow cycle.	50
5.13 Simulated flow cycle in JSM, showing density and velocity stream lines, taken at $s/d_{throat} = 2$ and $\text{NPR} = 6.8$. (1) Shows a pressure wave entering, (2) shows this pressure wave reflected, while another is entering the cavity. The interval between (1) and (2) represents the full movement of the Mach disk.	50
5.14 Spectra of parametric sweeps with oxygen and nitrogen.	51
5.15 Model validation at $s/d_{throat} = 2.0$.	52
5.16 Model validation at $s/d_{throat} = 3.0$, using different gases.	53
5.17 Qualitative model validation using wall temperature and heat flux.	54
5.18 Normalised simulated heating power and experimentally determined maximum tip temperature.	55
5.19 $s/d_{throat} = 3.0$ and $s/d_{throat} = 3.25$, both at $\text{NPR} = 6.8$, nitrogen.	56
5.20 Maximum tip temperature when as a function of oxygen total pressure. Two tests were conducted for the first two pressure settings and only a single one for the highest pressure.	57
5.21 Tip temperature as a function of s/d_{throat} using nitrogen at 16.6 bar upstream pressure after 6 seconds of resonance heating.	57
5.22 Frequency spectrum for different s/d_{throat} for nitrogen, using the modified conical resonator inlet. $\text{NPR} = 6.8$	58
5.23 System behaviour during ignition attempt	59
5.24 Equivalence ratios and maximum measured tip temperature for each ignition attempt. Fuel and oxidiser mass flow are determined based on measured upstream pressure and orifice size. Error is based on fluctuations in measured pressure sensor data.	61
B.1 Simulation of cylindrical resonance cavity for comparison with shock tube model.	71
B.2 Validation against 0D shock tube model	71
B.3 Front view of resonator with conical inlet under a digital microscope, comparable to Figure 5.3a.	72
B.4 Model validation for a conical resonator inlet.	72

C.1	Measured and corrected tip temperature at $s/d_{throat} = 3$ and NPR = 7.2 for oxygen . . .	75
C.2	Time dependent frequency for a 15 second resonance heating test at $s/d_{throat} = 3$ and NPR = 7.2 using oxygen.	77
C.3	Filtered oxygen, methane and chamber pressure data for all six combustion experiments.	78
C.4	Temperature profiles for select heating experiments.	79
C.5	Top view of the propellant feed system. Note the placement of the microphone to the left of the igniter. Three pressure transducers are visible. The methane PT and oxygen PT are attached directly to their respective propellant lines, with the chamber PT being mounted on a stand-off pipe.	79
C.6	Overview of the test setup showing the gas cylinders and data acquisition system.	80
D.1	Residuals of flow and turbulence variables for a simulation of $s/d_{throat} = 2$ and NPR = 6.8.	82
D.2	Pressure and FFT of pressure at the resonator tip for $s/d_{throat} = 3$ and NPR = 6.8.	83
D.3	Temperature and dimensionless wall distance near $x/L = 0.99$ for $s/d_{throat} = 3$ and NPR = 6.8.	83
D.4	Pressure and FFT of pressure at the resonator inlet for $s/d_{throat} = 3$ and NPR = 6.8.	84
D.5	Temperature and dimensionless wall distance near $x/L = 0.05$ for $s/d_{throat} = 3$ and NPR = 6.8.	84
D.6	Example of reduction in conductive time scale while maintaining a constant Fourier number.	85
E.1	Machining the bore that interfaces with both the oxygen injector and the resonator.	87
E.2	Measuring concentricity between the cavity inlet and the interface between the resonator and combustion chamber using a small dial indicator.	88
F.1	Diagram of side view of the test setup including blast shielding, gas cylinders and data acquisition system. Note that the plexiglass shielding covers all lines of sight to the test setup.	98

List of Tables

2.1	Summary of Characteristics of Resonator Operating Modes	10
5.1	Igniter Design and Operational Parameters	38
5.2	Design and Measured Resonator Dimensions	39
5.3	Elements of the Data Acquisition System	42
5.4	Peng-Robinson EOS Critical Parameters and Acentric Factors from [62]	46
5.5	Error in Fundamental Frequency between Simulation and Experiment	53
A.1	Safety Requirements	67
A.2	Design Requirements	68
A.3	Sensor Requirements	68
B.1	Error in Fundamental Frequency between Simulation and Experiment for Conical Resonator	73
C.1	Elements of the Data Acquisition System	74
D.1	Mesh quality parameters at nominal refinement	81
F.1	Igniter Failure Modes	97
F.2	Severity Categories for Risk Maps	99
F.3	Severity Categories for Risk Maps	99

Nomenclature

Abbreviations

Abbreviation	Definition
GOx	Gaseous Oxygen
NPR	Nozzle Pressure Ratio p_t/p_∞
SPL	Sound Pressure Level
TRL	Technology Readiness Level
JRM	Jet Regurgitant Mode
JSM	Jet Screech Mode
MMH	Monomethyl Hydrazine
UDMH	Unsymmetrical Dimethylhydrazine
MON	Mixes of Nitrogen (mixes of dinitrogen tetroxide and nitric oxide)
RP-1	Rocket Propellant-1 or Refined Petroleum-1
URANS	Unsteady Reynolds-Averaged Navier-Stokes
SST	Shear Stress Transport Model
MUSCL	Monotonic Upstream-centered Scheme for Conservation Laws
AUSM	Advection Upstream Splitting Methods
CFD	Computational Fluid Dynamics
CEA	NASA Chemical Equilibrium Applications
DARE	Delft Aerospace Rocket Engineering
LPRE	Liquid Propellant Rocket Engine
REACH	Registration, Evaluation, Authorisation of Chemicals
TEA	Triethylaluminum
TEB	Triethylboron
OTV	Orbital Transfer Vehicle
PT	Pressure Transducer
TC	Thermocouple
CFL	Courant-Friedrichs-Lewy Condition
FKM	Fluorine Kautschuk Material
CGR	Compressed Gas Regulator

Symbols

Symbol	Definition	Unit
t	Time	[s]
u	Velocity	[m/s]
a	Local Speed of Sound	[m/s]
f	Frequency	[Hz]
p	Pressure	[Pa]
T	Temperature	[K]
M	Mach Number	[-]
R	Specific Gas Constant	[J/kg/K]
C_p	Specific Heat Capacity at Constant Pressure	[J/kg/K]
C_v	Specific Heat Capacity at Constant Volume	[J/kg/K]
\dot{Q}	Heat Transferred	[W]
\dot{q}	Heat Flux	[W/m ²]

Symbol	Definition	Unit
h	Heat Transfer Coefficient	[W/m ² /K]
k	Thermal Conductivity	[W/m/K]
x	Distance from the Nozzle Exit	[m]
D	Diameter	[m]
L	Length	[m]
A	Surface Area	[m ²]
V	Volume	[m ³]
F	Force	[N]
C_d	Discharge Coefficient	[-]
y^+	Dimensionless Wall Distance	[-]
ρ	Density	[kg/m ³]
γ	Ratio of Specific Heats	[-]
τ	Time Scale	[s]
α	Thermal Diffusivity	[m ² /s]
ω	Acentric Factor	[-]
ϕ	Equivalence Ratio	[-]
ϵ	Emissivity	[-]
σ	Stress	[Pa]

Subscripts and Superscripts

Symbol	Definition
t	Total condition
s	Static condition
e	Exit condition
$*$	Critical condition (sonic condition)
∞	Ambient conditions
p	Particle property
i	Inner
o	Outer
R	Reflected Shock Wave
S	Incident Shock Wave
r	Recovery condition
f	Friction
sw	Shock Wave
$conv$	Convective
$cond$	Conductive
w	Wall
TC	Thermocouple
m	Mach Disk
c	Shock Cell
$throat$	Nozzle Throat
y	Yield

1

Introduction

A chemical rocket motor converts the energy released from the combustion of a fuel and an oxidiser into kinetic energy to generate thrust. Rocket propellants are therefore chosen based on their high energy release upon combustion as well as a high propellant density. The latter is critical for reducing the mass of propellant tanks and other fluid system components, directly increasing the payload mass that can be delivered into orbit [1] [2]. Reactants used in liquid propellant rocket engines (LPRE) can be broadly divided into two categories. Those that react spontaneously when coming into contact, known as *hypergolic* propellants, and those that require an external ignition source. The choice between these two types of propellants is based on considerations of safety, system complexity, storage requirements and performance, among others [1].

Storable, hypergolic propellants tend to be preferred for long-duration space missions. These missions require multiple ignition cycles, for reaction control or orbit adjustment and maintenance. Ignition reliability is therefore critical to mission success. Hypergolic propulsion systems have no artificial limit on the amount of restarts that can be performed. This makes their use very attractive for reaction control thrusters, or other applications where repeated pulsing of the motor may be required [1]. Long mission durations further require propellants to be chemically and thermally stable over many months or years. Hypergolic propellants for these applications, such as mono-methyl hydrazine (MMH) and mixes of dinitrogen tetroxide and nitric oxide (MON), have demonstrated exceptional reliability [1]. They are liquid at room temperature and can be kept inside a propellant tank for several years without degradation (if the vessel is appropriately cleaned and chemically resistant). This makes them particularly attractive for missions into deep space.

The majority of rocket propellants currently in use (in a civilian context) are non-hypergolic. Liquid oxygen is one of the most common oxidisers used in LPREs [1] and is frequently paired with either RP-1, liquid hydrogen or, more recently, liquid methane. The combination of liquid oxygen with liquid hydrogen has been used in applications that require high specific impulse, such as upper stage propulsion systems [2]. More recently, engine development has shifted more towards using liquid methane as a fuel. It offers high performance and has a similar boiling point to liquid oxygen, simplifying tank design [1]. With the exception of RP-1, the propellants introduced above are stored onboard at cryogenic temperatures. All cryogenic propellants are prone to boil-off over time as radiation from the sun heats up the vehicle and its propellant tanks. Typically the tanks onboard the satellite need to be kept significantly colder than the other system on the satellite bus [1], introducing additional challenges for thermal management systems. Upper stages of launch vehicles and orbital transfer vehicles (OTV) tend to have relatively short operational lifetime compared to the satellites they are carrying, making long-term storage of propellants is less critical. The high performance required for these applications lends itself well to cryogenic propellants, such as liquid oxygen in combination with hydrogen or methane.

Non-hypergolic propellants require an external source of heat to initiate combustion. Many rocket engine ignition systems have been developed, varying in complexity and in the number of re-ignitions that can be performed [2]. Reliability of ignition is the primary design objective, especially when a high

number of ignition cycles is required over the course of a mission. As the ignition system remains passive for most of the flight, low system mass is desirable.

1.1. The Move Towards Green Propellants

In the context of rocket propulsion the term *green* propellants refer to combinations of fuel and oxidiser that are less toxic and less environmentally hazardous than many of the currently used storable propellants [1]. In 2011 hydrazine was added to a European Union candidate list of substances of very high concern through REACH (registration, evaluation, authorisation of chemicals) [3]. The high carcinogenic potential of hydrazine and its derivatives being the primary motivation. Oxidisers based on dinitrogen tetroxide are also known to be highly corrosive and highly toxic. This leads to any test or integration facility requiring specialised personal protective equipment, trained operators and environmental permits to work with these propellants [4].

The EU is considering banning the use of hydrazine and its derivatives. In addition to the difficulties associated with propellant handling this has led to an increased interest in developing less toxic alternatives [1]. Very few propellant combinations exist that can be classified as hypergolic and non-toxic. A promising candidate for a storable oxidiser is hydrogen peroxide. This can be used as a hypergolic propellant in combination with an ionic liquid [5] or an otherwise non-hypergolic fuel with a highly reactive additive [6]. While these are promising alternatives to MON and MMH, concerns about the long term storability of hydrogen peroxide need to be addressed before it can be considered a direct substitute for current satellite propellants [7].

An alternative approach in the search for green propellants is to focus on non-hypergolic propellant combinations. This research usually centres around the viability of cryogenic propellants for longer duration space missions [8]. This also necessitates the development of simple and highly reliable ignition systems, which can last for several ignition cycles.

1.2. Rocket Engine Ignition Systems

The ignition source for a liquid propellant rocket engine must supply enough power to evaporate a small part of the propellant flow and raise its temperature beyond auto-ignition [2]. Once this part of the propellant flow ignites, the reaction is self-sustaining and combustion continues as more propellant is supplied to the thrust chamber.

Several different types of igniters are currently in use. For a system that requires only a single ignition cycle, pyrotechnic devices offer a very simple and effective solution. They are typically electrically-initiated, slow burning devices that incorporate at least one solid-propellant charge [2]. Organometallic-hypergols are frequently employed for similar applications and can, in some cases, be used for a small number of re-ignitions. Here a combination of triethylaluminum (TEA) and triethylboron (TEB) is injected ahead of the main fuel flow, where its pyrophoric reaction with liquid oxygen initiates combustion [2]. If the propulsion system requires a higher number of ignition cycles, spark torch igniters tend to be preferred. This also allows for greater mission flexibility as the same system can be used for many different mission types.

In a spark torch igniter, gaseous oxygen and fuel are brought together in a small combustion chamber. A spark is then used to ignite the propellant mixture. This produces high temperature exhaust gas that travels into the main combustion chamber of the engine, where it can ignite the main of the propellant flow. Such designs have been extensively used both for rocket engine test stands and as flight hardware [9] [10] [11]. A spark torch offers repeated ignition and very high thermal power at the cost of high system complexity compared to other ignition sources [2]. The high voltage required for the spark also places additional requirements on the electrical system of the vehicle. Spark torches can provide reliable ignition in a vacuum and under a large range of flow rates and mixture ratios. A point of vulnerability of torch igniters remains the spark source itself. The high temperature and oxygen rich environment of the igniter can cause corrosion of the spark plug. The inherent complexity of the system also creates multiple potential points of failure.

A promising solution to overcome these deficiencies could be the use of a thermo-acoustic igniter. Unlike a spark torch, a thermo-acoustic igniter does not require a spark source to initiate combustion.

Instead, the interaction between a supersonic flow and an acoustic cavity is used to generate heat. For certain propellant combinations these igniters could provide a very high number of ignition cycles with lower system complexity. To date no resonance igniter has been flown in a spacecraft or rocket propulsion system [12]. This is primarily due to the complexity in finding and maintaining a stable operating point for resonance heating [12]. Sustaining resonance and by extension generating a lot of heat directly depend on the choice of upstream pressure and a narrow range for certain geometrical parameters, further outlined in [section 2.6](#). This means that any deviation in upstream pressure may result in the chosen design parameters no longer being optimal for heat generation and ignition. A rocket engine might experience significant changes in propellant supply pressure over the course of a mission, especially if the propellant is pressure fed [1]. This means that the optimal values for design parameters may shift over the course of the flight, leading to potentially low ignition reliability. Attempts have been made to stabilise igniter performance with regard to upstream pressure, one of which will be further demonstrated in the thesis project.

A compounding issue for ignition system designers is the limited availability of literature on thermo-acoustic igniters. No comprehensive set of design guidelines exists that will guarantee high rates of resonance heating. Many of the existing studies on the mechanisms by which heat is generated in the igniter are somewhat contradictory. The large variation in possible geometrical parameters also means that studies, which perform experimental analyses, are rarely overlapping. Further experimentation and the development of better models for thermo-acoustic heating are required to raise the technology readiness level (TRL) of these systems and create viable igniter designs.

1.3. Report Structure

This thesis aims to improve the understanding of thermo-acoustic igniters through experimentation and numerical modelling. An experimental setup is designed and manufactured that supports resonance heating tests with both oxygen and nitrogen. Experiments are performed over different geometrical parameters and upstream pressure for both gases. A two dimensional fluid dynamic model is developed to efficiently simulate resonance heating and predict the operating conditions that result in the highest rates of heat generation. The simulation is extensively validated using the obtained experimental data and is shown to be able to predict both the operating mode of the igniter, as well as the parameters that lead to effective resonance heating. Finally, the experimental setup is used to demonstrate a prototype of a non-pre-mixed resonance igniter using gaseous oxygen and methane.

In [chapter 2](#) the theory behind thermo-acoustic resonance is introduced and how this can be used as an ignition source. This includes a summarised version of a literature review on the most relevant parameters initiating resonance, as well as a summary of some more common igniter designs. Existing approaches to numerical modelling of resonance heating are introduced.

The research objectives are introduced in [chapter 3](#), together with the requirements set for prototype igniter developed for this study.

The main methodology and results of this study are presented in [chapter 5](#) in the style of a research paper, with the goal of eventually submitting this paper to a journal. In [chapter 5](#) the most important background information on acoustic resonance is summarised, followed by a detailed description of the design of the igniter and test setup in [section 5.3](#). The numerical simulation is described in [section 5.4](#). The results of the resonance heating tests are presented in [section 5.6](#), together with the validation of the numerical model. The results from several combustion experiments with gaseous oxygen and methane are outlined in [section 5.7](#).

Further validation cases for the numerical model are documented in [Appendix B](#), with additional experimental results shown in [Appendix C](#). Additional results from the numerical model are shown in [Appendix D](#). The remaining appendices provide additional information on the risk assessment performed and the procedures developed for the experimental campaigns, as well as technical drawings for all parts of the igniter prototype.

2

Theoretical Background

Thermo-acoustic igniters are capable of initiating combustion between non-hypergolic propellants without the use of an external energy source. They rely on the interaction of an under-expanded gas flow with an acoustic cavity to create cycles of expansion and compression inside the cavity. Under the correct circumstances this process can rapidly increase the temperature of the entrained gas with each passing cycle. Sustaining this resonance is critical for achieving high gas temperatures and reliable ignition. Introducing a mixture of fuel and oxidiser into the resonance cavity can cause it to ignite and allow the reaction to propagate into the combustion chamber.

This chapter introduces the principles behind the initiation and sustainment of acoustic resonance. The various operating regimes of gas driven resonance are discussed. The sources of heat generation and loss mechanisms are expanded upon, followed by an analysis of the geometrical and operating parameters that influence thermo-acoustic heating. Approaches to modelling the heat generated by acoustic resonance are introduced.

2.1. Jet Driven Acoustic Resonance

The acoustic phenomena associated with under-expanded jets interacting with a resonance cavity were first discovered by Hartmann in the early 1920s [13]. These were primarily studied as acoustic generators, with the thermal properties of jet driven resonance discovered in 1954 [14]. Conrad and Pavli first proposed the use of such devices as an ignition source for hydrogen-oxygen rocket engines in 1967 [15]. Here the acoustic resonance was driven by a mixture of gaseous oxygen and hydrogen, with combustion initiating once the temperature inside the resonance cavity reached the auto-ignition temperature of the mixture. In literature such devices are often referred to as *Hartmann-Sprenger tubes*, or if specifically used as an ignition source, *thermo-acoustic igniters*. These terms are often used interchangeably. A schematic of a Hartmann-Sprenger tube is shown in [Figure 2.1](#).

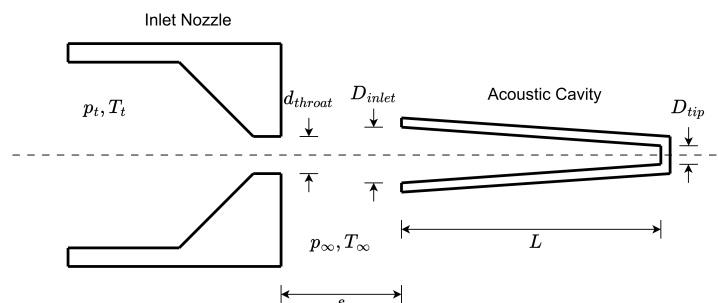


Figure 2.1: Overview of critical parameters for thermo-acoustic heating.

Gas enters from the left of [Figure 2.1](#). It is forced through a nozzle with a throat diameter (d_{throat}). If

the pressure ratio over this nozzle is larger than the critical pressure ratio of the gas, this flow becomes sonic ($M^* = 1.0$) at the nozzle throat. An acoustic cavity (sometimes referred to as the resonance cavity) is placed with its entrance in line with the under-expanded gas flow. Often this cavity is tapered towards the closed end. Its semi-conical shape can be defined by its inlet and tip diameters, D_{inlet} and D_{tip} , as well as its length, L . The gap between the nozzle and the entrance to the resonance cavity is denoted by a distance s .

The gap between the two components is fundamental to the working principle of the igniter. In this gap the sonic jet leaving the nozzle throat expands abruptly, creating a series of oblique shock- and expansion waves. The interaction of this shock structure with the entrance to the resonance cavity is responsible for sustaining the acoustic resonance. The shape of this shock structure is in turn determined by the total to static pressure ratio p_t/p_∞ over the nozzle throat, referred to as the nozzle pressure ratio (NPR). At a minimum, this NPR needs to be equal to the critical pressure ratio to guarantee sonic flow through the nozzle throat. The critical, total to static, pressure ratio can be determined using Equation 2.1 [16].

$$\frac{p^*}{p_t} = \left(\frac{2}{\gamma + 1} \right)^{\frac{\gamma}{\gamma - 1}} \quad (2.1)$$

Where $\gamma = C_p/C_v$ and p^* is the static pressure at the nozzle throat. p_t denotes the upstream total pressure. C_p and C_v are the specific heat capacity at constant pressure and constant volume, respectively. In the case of room temperature air, with $\gamma = 1.4$, the critical pressure ratio is 1.894. If the static pressure of the sonic jet at the exit of the orifice is higher than the ambient pressure, it is considered *under-expanded* [17]. A series of Schlieren images of under-expanded jets (without the presence of an acoustic cavity) at different total-to-static pressure ratios are shown in Figure 2.2.

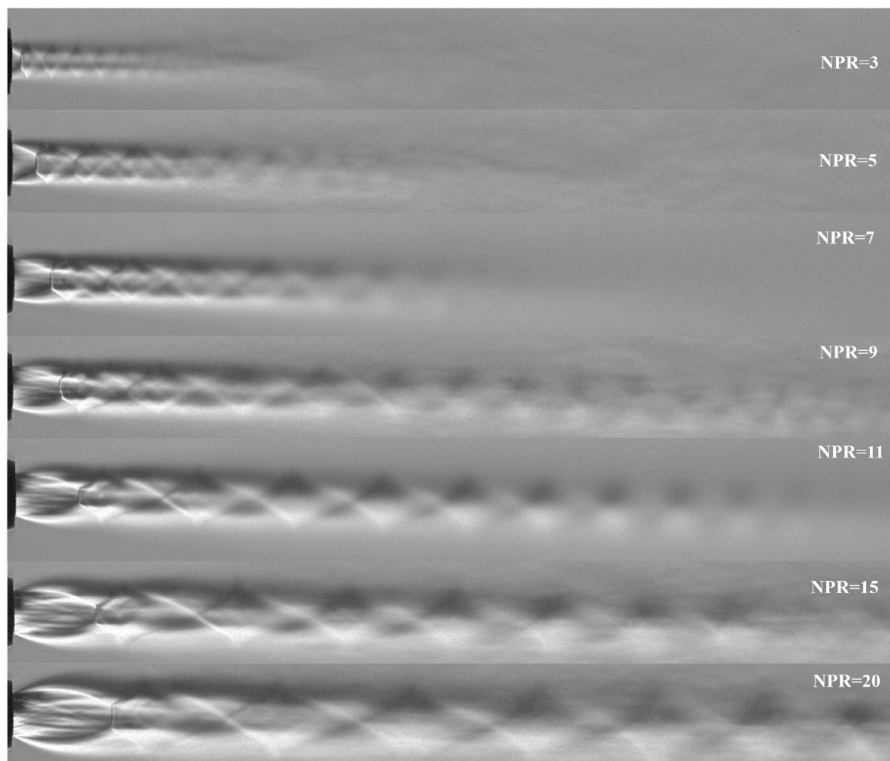


Figure 2.2: Schlieren images of under-expanded jets at different NPR. Taken from Samsam-Khayani et al. [18]

A jet that is moderately under-expanded features a *diamond* pattern of oblique shock waves. This generally occurs at $2 < \text{NPR} < 4$ (for a gas with $\gamma = 1.4$) [19]. The flow inside the jet remains weakly

supersonic after the oblique shock waves. An illustration of this structure is shown in Figure 2.3a. The gas is expanded at the nozzle exit by a series of Prandtl-Mayer expansion fans (C). These are reflected as compression waves once they reach the area where the static pressure inside the jet matches the surrounding ambient pressure (D). The reflected waves converge onto the centreline of the jet forming an oblique shock (E) [19].

If the pressure ratio increases to $4 < NPR < 7$ (for a gas with $\gamma = 1.4$) [19] a *barrel* structure with a *Mach disk* appears (shown at location (F) in Figure 2.3b). This occurs as the oblique shock waves coalesce into a normal shock near the centreline of the jet. An illustration of this highly under-expanded jet is shown in Figure 2.3b. Due to the presence of a normal shock, the flow in the centreline of the jet becomes periodically subsonic after the Mach disk. The flow then accelerates again and becomes supersonic in the following expansion region.

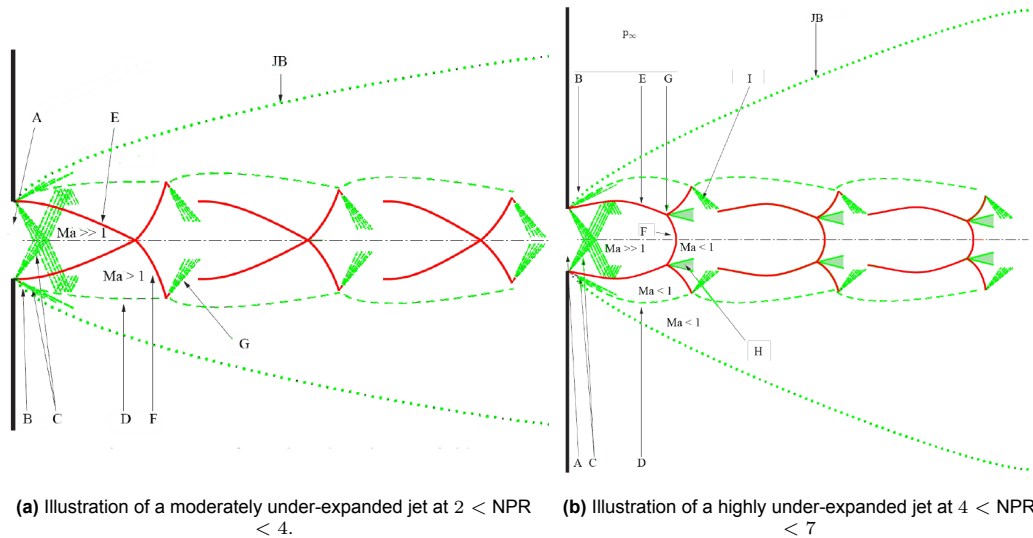


Figure 2.3: Illustrations of under-expanded jet flows, taken from Duronio, Villante, and Vita [19]

For all cases of under-expanded jet flows, the core flow experiences periodic expansion and compression, as it passes through the shock- and expansion waves. Smith and Powell described the zones of pressure recovery inside the jet as instability regions due to their adverse (positive) pressure gradients [20]. The shock structure and its associated pressure field are responsible for initiating and maintaining acoustic resonance [21].

2.2. Operating Modes

The exact location of the entrance of the acoustic cavity in this pressure field determines the operating mode of this thermo-acoustic interaction. It directly impacts the mechanisms by which heat can be generated and the effectiveness of a resonator as an ignition source. Three distinct operating modes have been identified by Sarohia and Back [21] that can initiate and sustain acoustic resonance. These modes have been further investigated by Bauer et al. [12] [22], Sarpotdar et al. [23], Sobieraj & Szumowski [24], Bouch & Cutler [25] and Iwamoto [26]. The most important operating modes for generating high gas temperature are known as the *Jet Regurgitant Mode* and the *Jet Screech Mode*. The remaining mode, the *Jet Instability Mode* does not result in significant flow heating and is therefore not covered extensively in this review.

2.2.1. Jet Instability Mode

The Jet Instability Mode (JIM) has been identified by Sarohia and Back [21] in subsonic jets with $NPR < \frac{p^*}{p_t}$. It is characterised by the formation of large, periodic, vortex structures at the nozzle exit. These cause weak pressure waves travelling into the resonance cavity, which are then reflected off of the closed cavity tip and travel back towards the nozzle. This has been shown to cause some

noise generation but does not have any measurable effect on gas temperature inside the cavity [21].

2.2.2. Jet Regurgitant Mode

If the NPR is increased beyond the critical pressure ratio, the flow leaving the nozzle throat becomes sonic and the acoustic cavity can enter the Jet Regurgitant Mode (JRM). The resonance frequency of JRM coincides with the quarter wave natural frequency of the cavity, and is therefore directly related to cavity shape. This mode is characterised by periodic oscillations in gas pressure and temperature at the tip of the resonance cavity. A diagram of the flow patterns associated with JRM are shown in Figure 2.4.

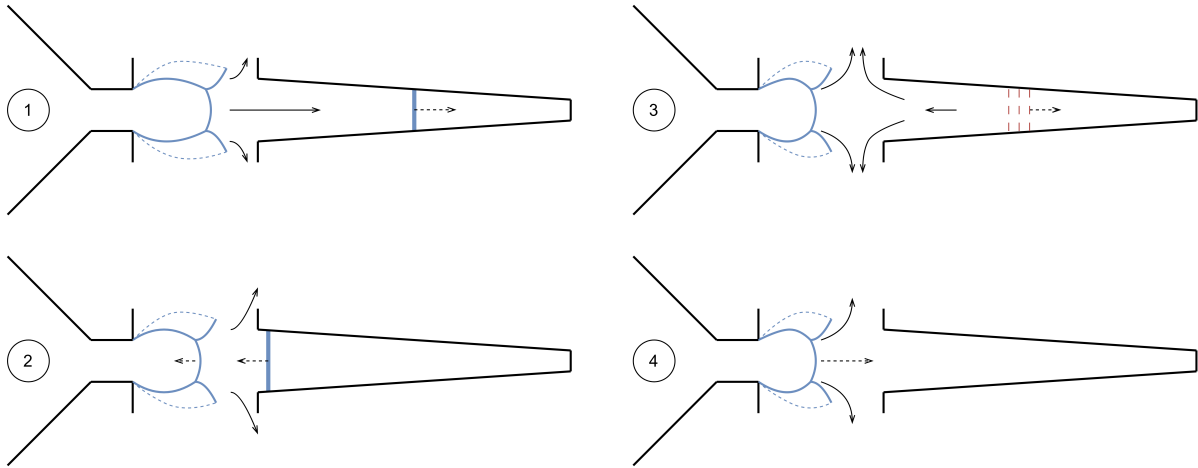


Figure 2.4: Illustration of the four phases of a jet regurgitant mode. A shock wave is denoted as a thick blue line, expansion waves as a set of dashed red lines. A solid arrow indicates flow direction, while a dashed arrow shows the movement of a shock wave. (1) shows the inflow phase, (2) and (3) show the two transitional phases and (4) the end of the outflow phase.

The detailed description of the jet regurgitant mode are based on observations by Sarohia & Back [21] and Sobieraj & Szumowski [24]. These, in turn, are based on pressure measurements inside the resonance cavity, as well as shadowgraph or Schlieren imaging of the gap between nozzle and resonator. The visualisation of the flow field provides important information on the behaviour of the under-expanded jet and its interaction with the cavity, while the instantaneous pressure measurements provide insights on the cyclic compression and expansion inside the cavity.

1. **Inflow Phase:** The inflow phase begins with a pressure difference between the gas behind the Mach disk and the gas already inside the acoustic cavity. Most of the flow passing through the under-expanded jet begins to enter the cavity [21]. The pressure difference results in a series of compression waves travelling down the length of the cavity. If the length to diameter ratio of the tube is large enough, these pressure waves can coalesce into a single, strong, shock wave. This incident shock wave raises both pressure and static temperature as it passes over the gas already inside the cavity. Upon reaching the closed end-wall of the cavity, the shock wave is reflected and travels back towards the nozzle. The reflected shock wave again increases the temperature and pressure of the entrained gas. At the same time as the shock waves pass over the entrained gas, the motion of the driving gas compresses the entrained gas further, increasing temperature and pressure. In many cases this results in end wall pressures that are higher than the total pressure of the under-expanded jet [12]. The shock waves are responsible for a large increase in static temperature of the entrained gas, along with some contribution from wall friction as the pressure waves enter the cavity. By leaving the cavity the shock wave induces a series of expansion waves that travel down the length of the cavity. This marks the beginning of the transitional phases.
2. **First Transitional Phase:** The expansion waves travelling inwards begins to reduce pressure at the inlet of the cavity. This low pressure region follows the expansion wave inwards and results in gas leaving the cavity. The flow moving out of the resonance cavity collides with the under-expanded jet flow and pushes the fluid interface between the two flows towards the nozzle. If

the NPR > 4 (for $\gamma = 1.4$) the flow upstream of the cavity entrance (just after the Mach disk) is subsonic. This means that the flow exiting the cavity can push against the under-expanded gas flow and cause the Mach disk to recede. At a lower nozzle pressure ratio, this does not occur, as the flow remains supersonic after passing through the oblique shock waves. The location of the shock structure is therefore not influenced by the outflow from the cavity [24].

3. **Second Transitional Phase:** The transitional phase ends when the Mach disk is pushed as far back as possible by the outflow from the cavity, when the fluid interface between the outflow of the cavity and the under-expanded jet comes to a standstill. Sarohia and Back [21] note that this phase, where the interface between the two flows remains stationary, is almost as long as the inflow phase.
4. **Outflow Phase:** There exists some overlap between the transitional phases and the outflow phase. The transitional phases focus largely on the interaction between the outflow from the cavity and the Mach disk, while the outflow phase describes the evacuation of the cavity. The outflow is driven by the expansion wave that follows the exit of the reflected shock wave. Outflow continues as the expansion wave is itself reflected at the cavity end-wall. This causes the pressure inside the cavity to drop even further. The outflow phase is complete when the reflected expansion wave has left the cavity. As the reflected expansion wave reaches the cavity inlet it suddenly reduces the pressure at the interface between the under-expanded jet and the outflow from the cavity. The Mach disk is again able to move towards the cavity inlet, beginning the next inflow cycle.

An important conclusion drawn in the study by Sarohia and Back [21] is that strong flow heating in JRM can only occur when the cavity is long enough to allow for the pressure waves in the inflow phase to coalesce into a shock wave before reaching the end wall. A significant part of the heat generated by the passing shock waves is transferred to the cavity wall through convection and radiation [27]. Over the course of several seconds of resonance heating this can cause cavity tip temperatures in excess of 600 °C, with corresponding gas temperatures estimated at up to 1600 °C during the compression cycle [12]. Loss of heat to the environment, as well as mixing losses with the incoming jet flow, cause the heating inside the resonance cavity to reach an equilibrium point after many JRM cycles. This is further elaborated on in [section 2.4](#).

2.2.3. Jet Screech Mode

The third operating mode for thermo-acoustic resonators described by Sarohia and Back is the Jet Screech Mode (JSM) [21]. The JSM is characterised by oscillations significantly above the natural frequency of the cavity. Schlieren images show the Mach disk of the under-expanded jet very close to the entrance to the cavity, nearly completely encompassing it [24]. An illustration of the flow patterns during JSM are shown in [Figure 2.5](#). The Mach disk in front of the tube entrance acts like a membrane weakly compressing and expanding the gas inside the resonance cavity [21]. With every back and forth motion, weak pressure waves travel down the length of the cavity. Unlike in JRM, many more compression waves enter before the first is reflected off of the end-wall of the cavity. These waves are not able to coalesce into a single shock wave. The primary mechanism generating heat in JSM are dissipative processes. Each incoming and reflected pressure wave causes gas to move along the cavity wall and increases both gas and wall temperature through friction. Most of the gas flow escapes around the inlet of the cavity rather than entering it. Very little mixing occurs between the flow entrained inside the cavity tip and the incoming flow. This allows for heat to accumulate with every pressure wave [24].

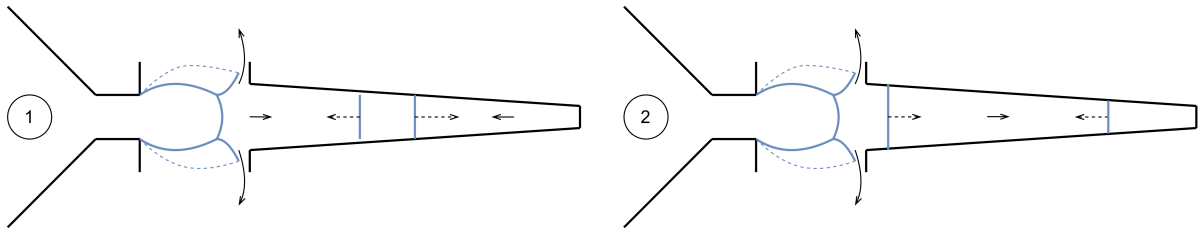


Figure 2.5: Illustration of resonating flow during the jet screech mode. Pressure waves are denoted as solid blue lines. A solid arrow indicates flow direction, while a dashed arrow shows the movement of a pressure wave. (1) and (2) show several pressure waves moving in different directions simultaneously. The Mach disk is close to the cavity entrance and moves very little during the cycles of entering and reflected pressure waves.

Compared to JRM the flow in front of the tube inlet appears almost static. The Mach disk in front of the tube moves towards the tube entrance and back at very high frequencies and over a very short distance. The dominant resonance frequency of these pressure waves do not initially appear to dependent on cavity shape, but instead only on jet pressure ratio and nozzle gap spacing [25]. Despite this, the harmonics of the cavity itself appear to influence the jet screech mode. Highest rates of resonance heating in JSM have been observed when the dominant frequency coincides with an overtone of the natural frequency for the cavity [25].

2.2.4. Switch Between Operating Modes

An acoustic cavity experiencing JRM as opposed to JSM primarily depends on a combination of NPR and s/d_{throat} , and to a lesser extent other geometrical parameters shown in Figure 2.1. Sarohia and Back observed the transition from JRM to JSM occurring at distinct pressure ratios and nozzle gap distances [21], identifying a region in which the jet regurgitant mode is stable. Once inside this stable regime the increase of nozzle pressure ratio or the decrease in nozzle gap size can cause the switch to the screech mode. An overview of where various authors have observed a stable JRM is discussed in section 2.6. Table 2.1 serves as a brief summary of the regurgitant and screech operating modes. The table is based on common observations for each mode, showing some similarities and differences.

Table 2.1: Summary of Characteristics of Resonator Operating Modes

Attribute	JRM	JSM
Resonance Frequency	Dominant frequency at the quarter wave natural frequency of the cavity	Dominant frequency significantly higher than the quarter wave natural frequency
Flow Cycle	Characterised by a single shock wave moving along the length of the cavity and being reflected off of the cavity end wall	Characterised by several weak compression waves travelling into the cavity at a very high frequency
Heating Mechanism	Heat generation in the fluid predominantly through incoming and reflected shock wave. Accompanied by volumetric compression of the entrained gas. Additional heating through friction at the cavity wall	Heat generation primarily through friction at the cavity wall caused by the travelling compression waves
Flow inside the cavity	A large amount of gas moves into the cavity following the incident shock wave. The reflected shock wave brings the flow to a standstill. Gas is expelled once the reflected shock exits the cavity	The weak compression waves cause less movement of gas inside the cavity. Each incoming wave causes some gas to move towards the cavity tip. reflected waves cause some gas to leave the cavity again.
Mach disk movement	Large variation in mach disk location during one flow cycle. During inflow, the mach disk can move into the resonance cavity.	Very small variation in mach disk location. The mach disk oscillates around a single point very close to the cavity entrance.

The distinction between JRM and JSM is helpful for categorising the operating envelope of a thermoacoustic igniter. Experimental spectra from several studies indicate a degree of overlap or coexistence of these two modes [12] [25]. As such the exact operating conditions under which JRM occurs are not always easy to identify. Some authors also disagree about which operating mode causes the higher rates of heat generation. Sarohia and Back, as well as Marchan attribute this to JSM [21] [28]. Bauer et al., on the other hand, only observe high end wall temperatures in JRM [12]. A fundamental problem with comparing test results from various authors is the different operating conditions and resonance cavity shapes used for these experiments. The experiments conducted by the three groups cited above use different resonance cavity shapes and test at different combinations of s/d_{throat} and NPR, with very little overlap. As such more experimental and numerical studies are required for a better understanding of this switch between operating modes and its dependence on resonator geometry.

2.3. Shock Tube Analogy

The temperature, pressure and velocity during the compression part of the JRM cycle can be approximated using analytical models developed for shock tubes. A shock tube is a device that contains high pressure gas on one side of a tube and low pressure gas on the other side. The two gases are separated by a diaphragm. Once this diaphragm is burst, a normal shock travels into the low pressure region. This shock wave is reflected by the closed end-wall of the shock tube and returns back towards the incoming, high pressure, flow [17]. A simplified diagram of a shock tube and time dependent flow pattern are shown in [Figure 2.6](#) [29].

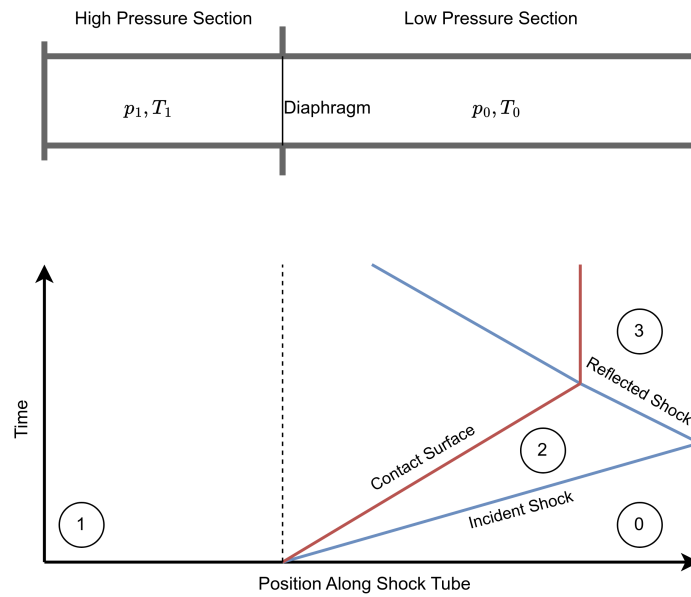


Figure 2.6: Simplified diagram of a shock tube and flow pattern. The blue line indicates the location of the shock wave over time, with the red line describing the interface between the gas in the left and right chamber.

At $t = 0$ the diaphragm is broken, causing pressure waves to propagate into the low pressure region. These coalesce into a shock wave [17]. As the shock wave passes over the contact surface between the high and low pressure gas, this contact surface begins to move in the direction of the right chamber with velocity u_p . The incident shock wave is reflected off of the closed end of the shock tube. The Mach number of the reflected shock wave is slightly lower than that of the incident wave, as it is now moving in the opposite direction, relative to u_p . The reflected shock wave passes over the moving contact surface and brings it to a standstill before it reaches the end of the shock tube. The equations to model shock tube flow are presented in [Appendix B](#).

A thermo-acoustic igniter differs in one critical aspect from a traditional shock tube. In a resonance igniter the side that contains the high pressure driving gas is open and continuously driven by the incoming flow from the under-expanded jet. In a shock tube the volume of driving gas is closed, as shown in [Figure 2.6](#). This means that the reflected shock wave can leave through the entrance of the resonance cavity at the end of the inflow cycle. Thompson presented a theoretical flow profile, as experienced by the flow inside the acoustic cavity, that is closely based on shock tube theory [30]. The profile is shown in [Figure 2.7](#). Note the similarity to [Figure 2.6](#) during the inflow cycle.

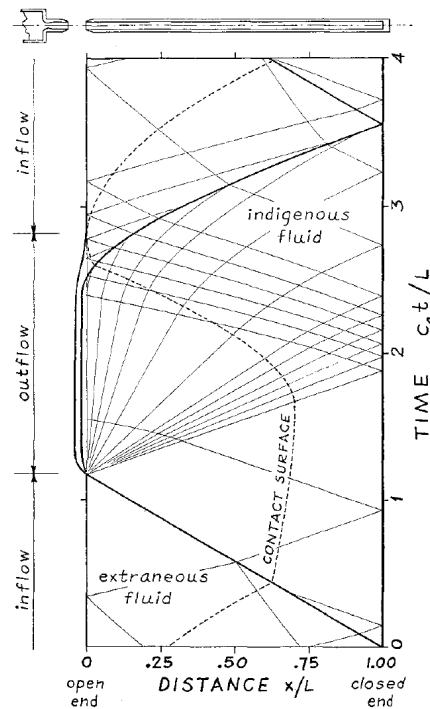


Figure 2.7: Figure taken from Thompson [30]. Illustration of time dependent velocity inside the resonance cavity. The incident and reflected shock wave is indicated as a thick black line, with expansion waves indicated as thin lines.

Figure 2.7 shows the inflow and outflow stages described in subsection 2.2.2. Following the reflected shock wave leaving the cavity, a series of expansion waves enter, travelling towards the end wall. Some representations of this pattern collapse these expansion waves into a single wave travelling at the same speed as the reflected shock wave [27]. These expansion waves cause a decrease in pressure and temperature of the gas entrained in the cavity. They pass over the contact surface, which has been more or less at rest since its interaction with the reflected shock wave. This causes the interface to move towards the entrance of the cavity, expelling gas from the resonator. Much like with the shock waves, these expansion waves are reflected at the cavity end wall, causing them to move back towards the entrance of the cavity [30]. The reflected expansion waves cause a final decrease in pressure and temperature of the entrained gas, as well as arresting the movement of the contact surface. This is the condition for the next inflow cycle to occur.

The entire flow cycle described in subsection 2.2.2 can be illustrated in a series of temperature and pressure plots, as well as velocity profiles inside the resonance cavity, based on the shock tube analogy and extended to include the outflow phase of JRM. This is shown in Figure 2.8.

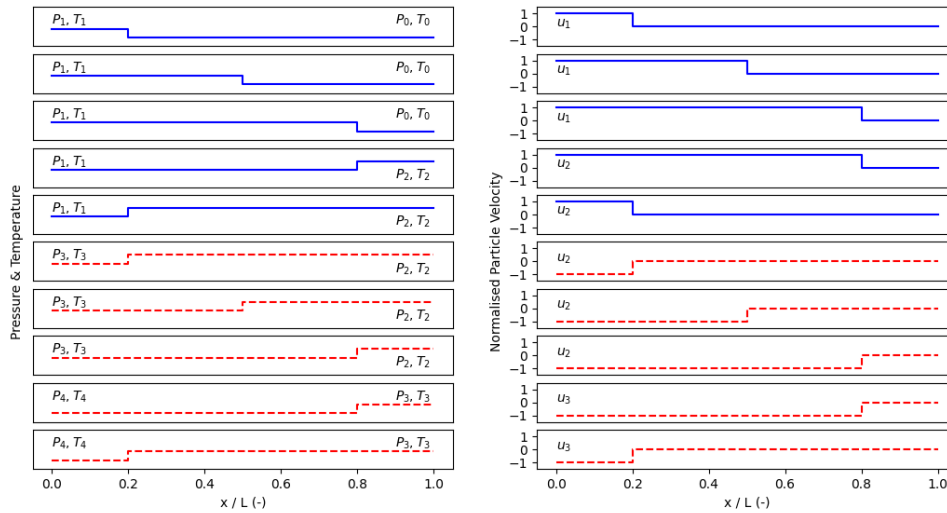


Figure 2.8: Illustration of temperature, pressure and particle velocity inside a shock tube. Note that both p and T in reality are closely linked and do not have the same value, as indicated in this figure. The sign of the velocity indicates if the velocity vector is pointed in positive or negative x -direction. Solid, blue, lines indicate the inflow phase, while dashed, red, lines indicate the outflow phase.

Here p_0 and T_0 denote the initial pressure and temperature of the entrained gas, with p_1 and T_1 being the pressure and temperature of the driving gas (essentially the pressure and temperature recovered after the under-expanded free jet). As the reflected shock wave passes over the entrained gas, the pressure and temperature rise to p_2 and T_2 . After the shock wave has left the cavity, the expansion reduces the pressure and temperature to p_3 and T_3 , with the final reduction in pressure occurring as the reflected expansion wave interacts with the gas, bringing it down to p_4 and T_4 . It is important to note that in this model $p_4 = p_0$, as it assumes that the pressure inside the cavity equalises to the ambient pressure after the outflow cycle. As entropy is generated over the incident and reflected shock wave, $T_4 > T_0$. As such the next cycle begins at a higher starting temperature, causing the continuous heating of the entrained fluid.

Several loss mechanisms and non-isentropic effects apply to the gas inside the resonance cavity that reduce the difference between T_4 and T_0 . These are further explored in [section 2.4](#). The shock tube analogy is useful for assessing the dominant mechanism behind heat generation in JRM, as well as making a idealised estimate of the flow profile inside the cavity, without using numerical solutions to the Euler or Navier-Stokes equations. Some researches have used the shock tube analogy to create models for thermo-acoustic resonators. Brocher & Maresca [27] and Thompson [30], among others have been successful with this approach. The assumed flow profile has also been used for one dimensional thermal models, such as the one proposed by Kawahashi and Suzuki [31].

2.4. Energy Balance and Loss Accounting

The flow inside Hartmann-Sprenger tubes is governed by several reversible and irreversible processes that determine the maximum temperature attainable inside the resonance cavity. An analysis of the main sources of heating and loss can give insight into the dominant influence parameters that need to be assessed for any igniter design. The processes for heating differ between the two main operating modes. This section is broadly applicable to a thermo-acoustic igniter operating in either JRM or JSM. However, most of the available literature focuses on analysing JRM, as the aforementioned shock tube analogy can be used to derive a closed model for the flow field inside the cavity [27]. The general energy balance of the gas inside the resonance cavity can be described using [Equation 2.2](#).

$$Q = Q_{sw} + Q_{friction} - Q_{mixing} - Q_{conv} \quad (2.2)$$

The system boundary to which Equation 2.2 is applied, is the interior of the resonance cavity. Q_{sw} is related to the entropy generated over a shock wave. $Q_{friction}$ is heat generated by friction, as the flow moves along the cavity wall. Q_{mixing} describes mass flow entrained in the boundary layer, which develops along the cavity wall. This occurs as the flow in the boundary layer is slower than the core flow, allowing some of the entrained gas to mix with the driving gas during the inflow and outflow phases. Lastly, Q_{conv} is the convective heat transfer between the hot gas inside the resonance cavity and the cavity walls. The energy balance in Equation 2.2 applies to JRM. When applied to JSM the term associated with the entropy over a normal shock wave (Q_{sw}) is zero.

The resulting process associated with JRM can be illustrated in a T-S-Diagram, shown in Figure 2.9. Figure 2.9 shows the temperature and pressure change inside a cylindrical resonance cavity during the inflow phase of JRM, according to the shock tube model presented in Appendix B.

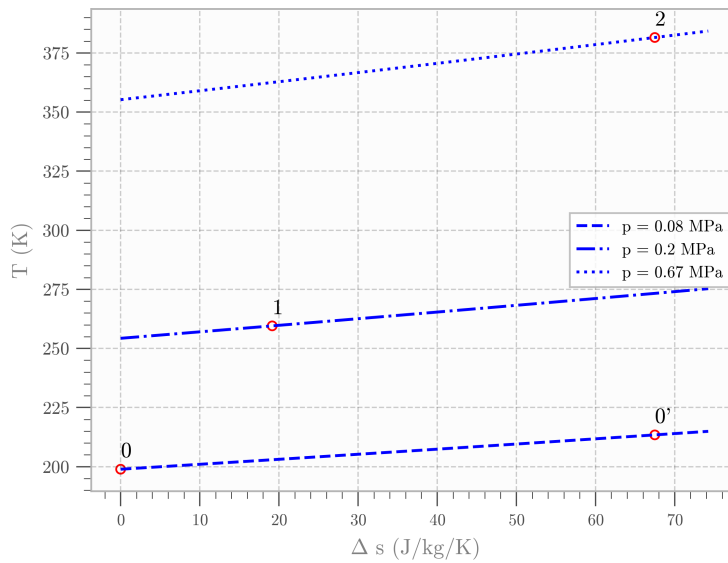


Figure 2.9: Temperature-entropy diagram of the entrained gas in JRM. The flow is modelled as a shock tube, with NPR = 6, using oxygen at an inlet pressure of 10 bar.

Between station 0 and 1 the flow experiences the first, incoming shock wave. The reflected shock wave brings the flow to state 2. If no heat loss mechanisms act on the flow, expansion would return it to state 0'. However, convective heat loss reduces the temperature at constant pressure. During the outflow, expansion returns the fluid to a point very close to state 1, depending on the exact amount lost due to heat transfer and mass flow through the boundary layer.

2.4.1. Heating over a Normal Shock

The main source of heat addition in JRM is the increase in static pressure over the incident and reflected shock wave. This term can be expressed as shown in Equation 2.3, assuming that C_p of the entrained gas does not vary as a function of temperature or pressure.

$$Q_{sw} = mC_p\Delta T \quad (2.3)$$

Here, m is the mass of the entrained gas, C_p its specific heat at constant pressure and ΔT refers to the temperature difference between T_0 and T_2 in Figure 2.9. In reality, this temperature difference also includes a contribution from isentropic compression of the gas inside the cavity. As the particle front moves towards the cavity tip, it compresses the entrained flow. The static temperature increase over a shock wave is a ratio of specific heats of the driven gas and the pressure ratio over the shock wave [17]. In the context of a Hartmann-Sprenger tube the pressure ratio is a direct function of NPR and therefore related to incident Mach number.

2.4.2. Friction

Heat addition through friction is an important contribution to flow heating in JRM and crucial for heating in JSM [24]. During each period when the particle interface in [Figure 2.7](#) moves, friction is generated between the moving fluid and the resonator walls. According to Brocher and Maresca [27] this generated loss through friction can be expressed as [Equation 2.4](#), assuming that the same amount of heat is generated during the inflow and outflow phases.

$$\partial Q_{fr} = C_f \rho u_p \frac{S}{D} (t_2 - t_1) \partial x \quad (2.4)$$

here C_f is the friction coefficient, dependent largely on Reynolds number and surface roughness and S/D refers to the ratio between the internal section surface area and the hydraulic diameter. The time difference between t_1 and t_2 refers to the time between when the contact surface begins to move and when it stops. u_p is the particle velocity. [Equation 2.4](#) can be integrated over the length of the resonance cavity. The particle velocity is a function of the incident Mach number. As a result, the heat generated through friction is directly dependent on incident Mach number, ratio of specific heats, cavity length and Reynolds number. This means that, in general, a resonance cavity with high L/d_{throat} produces more heat through friction.

2.4.3. Heat Loss to the Cavity Walls

The dominant mechanism for heat removal from the entrained gas is convective heat transfer to the cavity walls [27]. This phenomenon is highly dependent on the material of the resonance cavity [27]. This mechanism causes both heat transfer to the cavity wall, as hot gas moves past it, as well as a release of heat back into the gas during the outflow phase, with the now leaving entrained gas colder than the wall. The effect of conduction along the length of the resonator wall (in the direction of the mean flow) can usually be neglected, as the cavity has a very large length to diameter ratio [27].

Heat removal from the outer wall of the cavity to the environment adds an additional heat removal mechanism. As such it can be assumed that the heat flux due to convection is equivalent to the conduction through the cavity wall. Forced convective heat transfer occurs when only when the gas inside the cavity is moving. The magnitude of this heat flux depends on local gas and wall temperature, as well as flow properties. If it is assumed that the heat transfer coefficient is the same for both the inflow and the outflow phase, heat transfer due to convection can be written, as shown in [Equation 2.5](#) [27].

$$Q_{conv} = 2\pi Dh \int_0^L (T_r - T_w(x))(t_2 - t_1) dx \quad (2.5)$$

Where the x-axis is in line with the mean flow direction inside the resonance cavity. D is the cavity diameter, h is the convective heat transfer coefficient, T_r is the recovery temperature of the gas and T_w the wall temperature as a function of x. The time difference between t_1 and t_2 is the time between the contact surface beginning to move, and it stopping again. [Equation 2.5](#) can be integrated over the length of the resonance cavity. The heat transfer coefficient can be determined through empirical correlations. Typically these will depend on Reynolds number and Prandtl number of the flow, with some including friction effects as well. As such the magnitude of convective heat transfer is a function of fluid properties, upstream Mach number (in the form of flow velocity and Reynolds number), cavity length, cavity friction coefficient and material properties. A cavity material with lower thermal conductivity will have a higher equilibrium temperature, and cavities with higher length will result in a larger total amount of total heat exchanged. Similarly, a higher inflow Mach number increases this type of heat exchange, with a higher ratio of specific heats (for example in mono-atomic gases like helium) will exacerbate this effect [27] [25].

2.4.4. Entrainment Loss

During the process of inflow and outflow of gas from the resonance cavity there is a significant velocity difference between the boundary layer (at the cavity wall) and core flow. The flow inside the cavity is also expected to be highly turbulent. Mixing between the entrained gas and the driving gas is there-

fore considerable. The mixing between the entrained hot gas and the colder driving gas has been demonstrated experimentally in JRM [32]. Here the heat loss for can be quantified using Equation 2.6.

$$Q_{mixing} = m^* \cdot C_p (T_{gas,entrained} - T_{gas,driving}) \quad (2.6)$$

Where m^* represents the mass exchanged between the driving gas and the gas entrained inside the cavity and C_p is the specific heat at constant pressure. Brocher and Maresca claim that m^* is a function of Reynolds number, inflow Mach number and cavity length [27]. $T_{gas,entrained} - T_{gas,driving}$ is the difference between the temperature of the entrained gas and that of the colder driving gas. Depending on the magnitude of m^* , this effect can be the dominant mechanism of heat removal [27].

Both the resonator geometry and the operating point of a resonance igniter have a strong influence on the amount of heat generated and transferred. section 2.6 covers the specific effect of certain design parameters on the operating mode of the igniter and the effectiveness of heat generation. In general, a higher Mach number of the inflowing gas increases the temperature rise over the shock wave. Longer resonance tubes directly increase friction, convective heat transfer and mass exchange. Finally, the use of mono-atomic gases causes increased heating performance for the same cavity geometry and operating point [25]. The ratio of specific heats of a mono-atomic gas is around 1.667, in turn increasing the pressure and temperature ratio over a shock wave, as shown in Appendix B. These general observations seem to hold for both JRM and JSM.

2.5. Thermo-Acoustic Igniter Design

Several forms of thermo-acoustic igniters have been proposed for rocket engine ignition. These primarily differ in the mechanism by which ignition and mixing between fuel and oxidiser are achieved. Two primary designs exist that rely on ignition of a propellant mixture inside the resonance cavity [28]. The most commonly used igniter design is one that uses pre-mixed gaseous propellants entering the resonance cavity from a single nozzle. A diagram of such a design is shown in Figure 2.10.

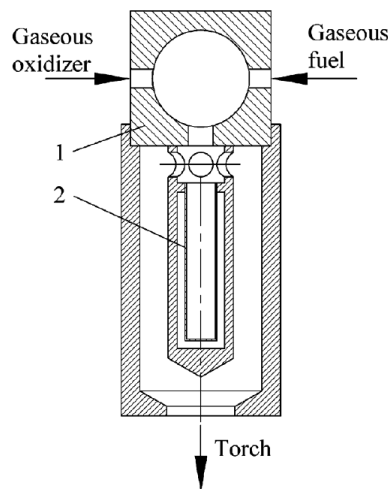


Figure 2.10: Pre-mixed igniter configuration, taken from Marchan [28]. (1) denotes the injector and (2) the resonance cavity.

An igniter like the one illustrated in Figure 2.10 has been tested by Phillips and Pavli [33] and BAUER, LUNGU, and HAIDN [12], among others. It requires both propellants to be gaseous. In such a design ignition occurs inside the resonance cavity [28]. Another design that causes ignition to occur inside the resonator is shown in Figure 2.11. It is similar to Figure 2.10, with the difference that one of the propellants is injected through a separate orifice. Here too, mixing occurs just outside the resonance cavity.

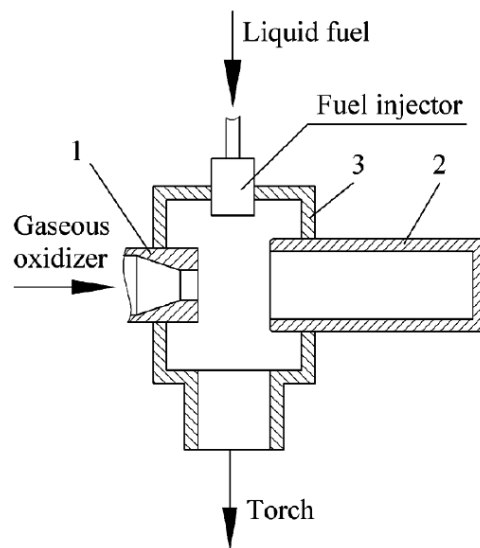


Figure 2.11: Non-pre-mixed igniter configuration, taken from Marchan [28]. (1) denotes the oxygen injector, (2) the resonance cavity and (3) the combustion chamber.

Designs such as the one shown in [Figure 2.11](#) have typically been used with liquid fuels [28] [34] in combination with gaseous oxygen. In these designs mixing is achieved from the velocity difference between the supersonic under-expanded jet and the slower liquid entering from the other orifice [28]. This design introduces some uncertainty in the mixture ratio inside the cavity [28], as the exact amount of entrained liquid is difficult to estimate.

For this thesis an igniter similar to [Figure 2.11](#) has been designed and tested. This design offers the advantage of not requiring pre-mixing of the oxidiser and fuel. This reduces the risk of flashback into the propellant lines and improves overall operational safety. Unlike existing non-pre-mixed resonance igniters, gaseous oxygen and gaseous methane are used as propellants.

2.6. Parameters Influencing Acoustic Resonance

Several design parameters common to all thermo-acoustic igniter designs have a large influence on performance. Often only a narrow range of values for these parameters and operating points result in sufficient heating to initiate combustion. Operational parameters, such as inlet pressure and temperature, as well as NPR in addition to the geometric parameters shown in [Figure 2.1](#) can impact the dominant operating mode of the igniter and its acoustic heating performance.

2.6.1. Driving Gas

The choice of gas to drive the acoustic resonance has a significant impact on the maximum temperatures attainable inside the resonance cavity. As already explored in [section 2.4](#), the ratio of specific heats, γ , is directly or indirectly relevant for all significant mechanisms of heat addition and removal. The effect of different gas composition on maximum gas temperature is shown in [Figure 2.12](#).

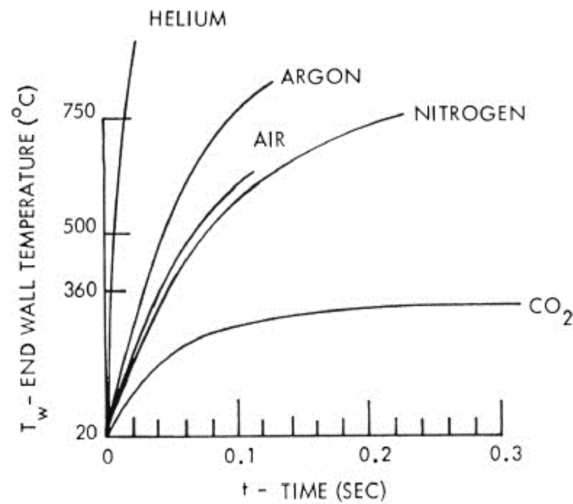


Figure 2.12: A comparison of highest attained gas temperatures with different driving gases. Oxygen is not shown here, but is expected to perform similarly to nitrogen, being a diatomic gas with similar molecular weight. Taken from E. Rakowsky [35]

Figure 2.12 shows that the maximum temperature appears to be strongly correlated with γ . Here the mono-atomic helium with $\gamma = 1.667$ attains significantly higher temperatures than CO_2 with $\gamma = 1.28$ [36]. Molecular weight also appears to play some role, as argon displays a significantly lower heating performance compared to helium (despite also being mono-atomic). Most resonance igniter designs make use of oxygen as the driving gas [12] [28] [34]. It is a very common oxidiser used in liquid propellant rocket engines [1] and thus widely available in different rocket engine designs. Some igniter designs use a mixture of hydrogen and oxygen [33]. For this thesis oxygen and nitrogen will be used as the driving gas for resonance heating tests.

2.6.2. Nozzle Gap Spacing and NPR

The most widely studied parameters are the nozzle gap spacing (non-dimensionalised as s/d_{throat}) and the nozzle pressure ratio (NPR). These two parameters are closely related and have a significant impact on igniter performance. These two parameters seem to be driving for both the expected operating mode of the igniter [21] and the maximum attainable resonator end-wall temperatures [27].

The nozzle pressure ratio directly determines the position of the pressure recovery regions inside an under-expanded free jet. Hence the optimal distance between the cavity inlet and the nozzle is also related to the NPR [21]. Sarohia and Back observe that the switch from a screech mode to the regurgitant mode occurs at fixed nozzle gap spacings for a given NPR [21]. This switch occurs when the nozzle gap spacing is approximately equal to the distance between the nozzle exit and the first mach disk of the free jet (often denoted as X_c). This transition is indicated in Figure 2.14 and is found to hold up until a NPR of approximately 6 [21]. Between a NPR of 6 to 8 this point moves towards the location of the second mach disk.

Some disagreement exists between authors observing JRM, what the optimum value of s/d_{throat} for any given NPR. Przirembel and Fletcher suggest to place the inlet at the third compression cell (instability region) of the free jet structure [37]. The observation by Sarohia and Back, that for certain NPR, JRM occurs between the first and second cell of the free jet, is validated by Bauer et al. [12] [22]. They also find the transition to a regurgitant mode closer to the second instability region but before the end of the second shock structure [12]. This coincides with the point of best heating performance. This has been replicated, albeit, at slightly lower NPR ranges by Sarpotdar et al. [23] and shown in Figure 2.13.

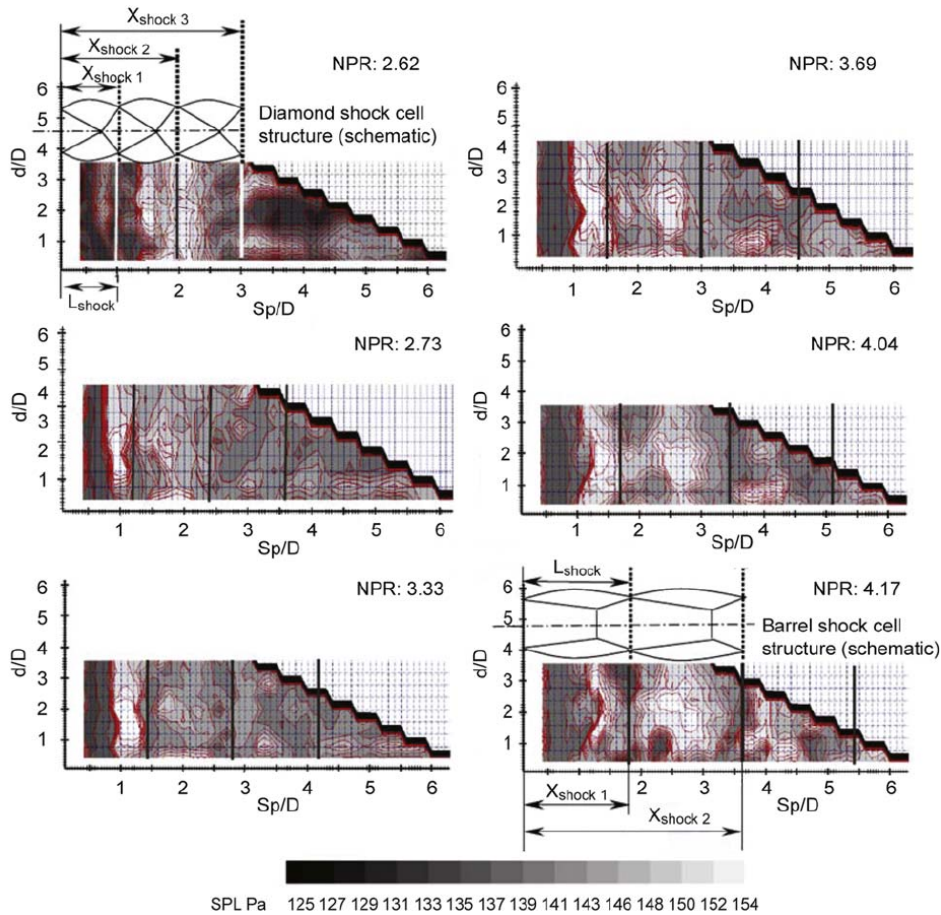


Figure 2.13: Sound pressure level measurements as a function of s/d_{throat} and NPR. The white areas denote spacing at which resonance was observed, with the black vertical lines indicating the expected length of shock structures X_s . Taken from Sarpotdar, Raman, and Cain [23]

Figure 2.13 shows the sound pressure level (SPL) measured near the resonator gap as a function of s/d_{throat} for different nozzle pressure ratios. The sound pressure level appears to be directly related to the heat generated in JRM. Note that particularly for the highest NPR tested (4.17) the highest sound pressure level is found in the second barrel shock structure. According to Figure 2.13 this only appears to be the case when the NPR is high enough to produce a barrel shock ($NPR > 4$). Lebedev & Bocharova show that the location of the Mach disk and the end of the first shock structure are influenced by downstream obstructions (such as a resonance cavity) [38]. As such the calculated location of a Mach disk of free under-expanded jet can differ slightly from that of an under-expanded jet in front of the resonance cavity. This makes it difficult to draw universal conclusions about the optimal placement of the cavity with respect to the under-expanded jet.

Figure 2.14 shows the combinations of NPR and s/d_{throat} that have been identified by several authors as causing high rates of resonance heating linked to JRM. The area shaded in green shows where Sarohia and Back report a stable jet regurgitant mode [21].

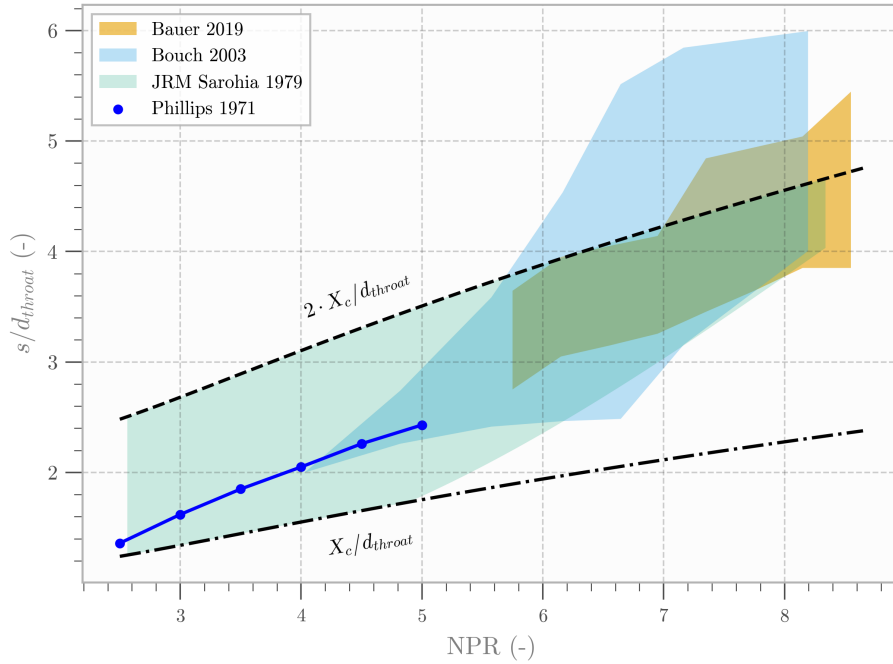


Figure 2.14: Comparison of nozzle gap spacing and NPR associated with high tip temperatures, taken from Bauer et al. [12], Bouch & Cutler [25] and Phillips & Pavli [33]. The green area represents the region, in which JRM has been identified as dominant, by Sarohia & Back [21]. The length of the first and second shock structure are determined using Equation 5.1.

It is important to note that Figure 2.14 is reconstructed from image data from the various authors. It is therefore not exact and to be taken as an illustrative comparison of the work performed by these authors. In all cases, nitrogen or oxygen are used as a driving gas. As both are diatomic gases with similar molecular weights, they are expected to behave similarly. It does indicate some agreement in the area in which high heating performance is expected in conjunction with the jet regurgitant mode. Another observation common to all authors is that higher heating rates coincide with a higher NPR, likely due to its effect on the strength of the incident shock wave.

Literature on optimum operating conditions exist for igniters operating in screech mode as well, specifically, in works by Marchan [28] and Sarohia and Back [21]. Both describe high heating rates for nozzle gap spacing below the length of the first shock structure ($s < X_c$). Marchan observes this behaviour between $\text{NPR} = 5.68$ and $\text{NPR} = 19.89$. As such, optimal heating performance is reported in the first instability region of the under-expanded jet. Experiments by Bouch & Cutler show that at $\text{NPR} > 20$ the highest rates of resonance heating occur in JSM (at $s/d_{throat} > 3$). The areas where these experiments produce a stable jet regurgitant mode are shown in Figure 2.14. As the nozzle pressure ratio is increased above 20, the cavities tend to transition to a screech mode. These observations strongly support the suggestion by Marchan that strong heating in JSM occurs in the first instability region of the under-expanded jet.

The NPR also has an impact on the magnitude of the incident Mach number for the incident shock waves, observed during JRM. As such, a higher pressure ratio generally results in higher heating rates in this mode [27].

2.6.3. Non-Dimensional Cavity Length

The cavity length has a strong impact on the dominant resonance frequency, specifically in the jet regurgitant mode [12]. The length of the resonance cavity is typically non-dimensional with respect to the throat diameter of the driving gas inlet, and commonly represented as L/d_{throat} . This allows for better comparison between designs of different scales. Sarohia and Back [21], as well as Lungu et al. [12] indicate that JRM is the dominant heating mode for cavities with a high L/d_{throat} . Long tubes allow for compression waves to coalesce into normal shock waves during the inflow phase and hence produce

irreversible heating over the incoming and reflected shock waves, as explained in subsection 2.2.2. Sarohia and Back [21] tested cavities with L/d_{throat} of 2.7 which were too short to have incident pressure waves coalesce into strong shock waves. In this kind of short cavity the Jet Screech Mode seems to be the best operating mode for heat generation.

Lungu et al. [12] found heating predominantly occurring in JRM with $L/d_{throat} = 11$. Excessive cavity lengths have been found to reduce maximum cavity tip temperature. Phillips and Pavli finding optimal heating performance in intermediate length tubes [33]. Here $L/d_{throat} = 9.37$, $L/d_{throat} = 19.06$ and $L/d_{throat} = 27.5$ show similar heating performance in cylindrical cavities. If the length is increased to $L/d_{throat} = 37.18$, the maximum attainable temperature decreases. This is shown in Figure 2.15.

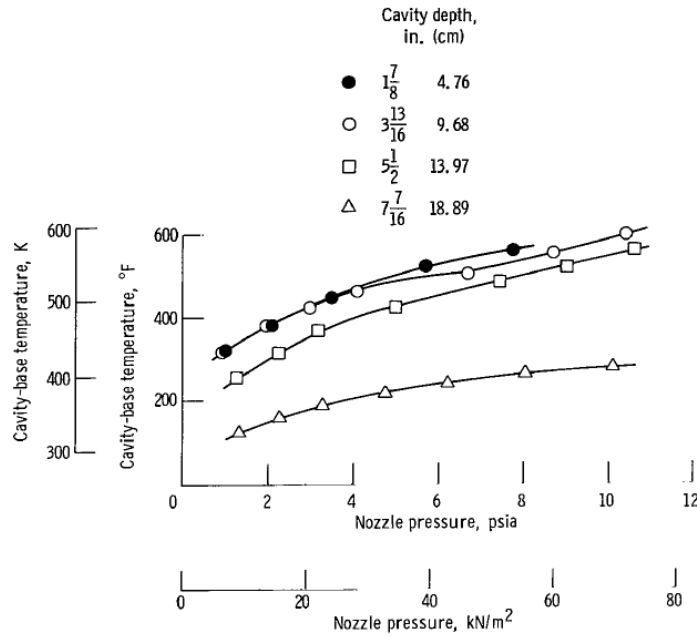


Figure 2.15: Comparison of heating performance for different cavity lengths, taken from Phillips and Pavli [33]. The cavity lengths tested here are equivalent to $L/d_{throat} = 9.37, 19.06, 27.5$ and 37.18 .

As discussed in section 2.4 the length of the acoustic cavity has an impact on the heat transmitted to the cavity walls, as well as the amount of friction heating and the amount of mixing losses in the boundary layer of the cavity flow. High heating performance in JSM is not limited to short tubes. Marchan uses cavities with $L/d_{throat} > 10$ and reports excellent heating performance in JSM, however, at high nozzle pressure ratios [28].

2.6.4. Resonator Inlet Diameter

The ratio cavity inlet diameter to throat diameter D_{inlet}/d_{throat} seems to play a role in the maximum heat generated in the igniter. Values between 1 and 2.5 have been used in experiments. Marchan proposes a correlation between D_{inlet}/d_{throat} and NPR [28]. For an NPR between 5.5 and 7.5 an optimum is found D_{inlet}/d_{throat} of 1.6, as outlined by Equation 2.7. This relation is only validated for a single tube design (tapered with cylindrical aft section) [28].

$$\frac{T_{max,cavity}}{T_{ambient}} = \left(1.246 - 1.1896 \left(\frac{D_{inlet}}{d_{throat}} \right) + 0.3616 \left(\frac{D_{inlet}}{d_{throat}} \right)^2 \right)^{-1} \quad (2.7)$$

2.6.5. Cavity Shape

Many different resonance cavity shapes have been characterised in thermo-acoustic igniters [39]. The two most common geometries used to achieve high tip temperature are *conical* and *tapered* resonance cavities. Combinations of conical and cylindrical cavities have been used, such as in designs tested

by Marchan [28] [34]. Both feature an initially converging cavity, with a cylindrical section of smaller diameter at the end.

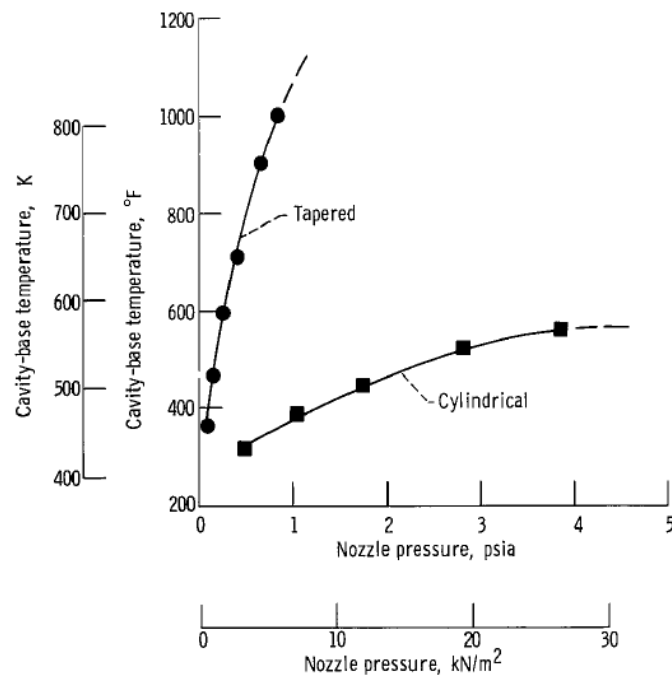


Figure 2.16: Heating performance in a cylindrical cavity compared to an equivalent cavity with a 3° half angle. Taken from Phillips and Pavli [33]

The use of a conical resonance cavity or semi-conical resonance cavities have been found to improve heating performance considerably [33] [40]. Figure 2.16 shows the difference in heating performance of a conical resonance cavity compared to one that is cylindrical. A study of shock tubes with converging sections by Sembian and Liverts [41] shows that the converging section causes the mach number of the incident shock wave (and thereby the maximum attainable end wall pressure) to increase significantly. This phenomenon explains the increase in end wall temperature observed in Figure 2.16, as the maximum fluid temperature is directly related to maximum pressure ratio [17].

2.7. Resonance Ignition

Several seconds of resonance heating are typically required to generate sufficiently high temperature at the tip of the resonance cavity to initiate combustion, irrespective of the dominant operating mode [12] [34]. Once a sufficient quantity of the propellant has been brought above its auto-ignition temperature a self-sustaining reaction can occur and the ignition will propagate to the remaining parts of the igniter. Depending on the igniter design the propellant heating is accomplished either through ongoing resonance heating, the wall temperature of the resonance cavity, or a combination of the two.

2.7.1. Propellant Mixing

Many resonance igniter designs use gaseous oxygen as an oxidiser [28]. Liquid oxygen is one of the most common oxidisers used on LPREs and a suitable gas for driving resonance heating [12]. This allows the igniter to use evaporated on-board propellants, as opposed to requiring a separate propellant supply. Resonance igniters have been demonstrated with a variety of gaseous and liquid fuels. Kerosene (or RP-1) has been demonstrated in a non-pre-mixed configuration by Marchan [28] [34]. Here gaseous oxygen (or air [28]) is used to drive the acoustic resonance, with the fuel injected perpendicular to the resonating gas, inside the combustion chamber. The liquid fuel is atomised by the injection and mixes with the under-expanded jet. Some of this fuel is entrained with the oxygen entering the resonance cavity, leading to ignition.

When paired with a gaseous fuel, such as hydrogen [33] or methane [12], the propellants are typically pre-mixed upstream of the under-expanded jet. This ensures a suitable mixture ratio at the tip of the resonance cavity, but introduces a significant risk of flashback into the propellant supply lines. This can lead to the flame front propagating from the combustion chamber into the oxygen supply, potentially leading to a catastrophic failure of the ignition system. This risk is somewhat mitigated by ensuring sufficient pressure drop over injection elements and through the use of specific timing of the fuel injection into the mixing chamber [12]. The use of gaseous propellants in a non-pre mixed configuration has not yet been studied in a resonance igniter. This thesis uses oxygen as the design driving gas for acoustic resonance, with gaseous methane injected perpendicular to the under-expanded jet after a period of resonance heating. This aims to demonstrate the viability of non-pre-mixed ignition with gaseous propellants. This not only contributes to improved testing safety but provides an igniter design that is viable for use with either a gaseous or liquid fuel.

2.7.2. Ignition Characteristics of Methane

Liquid methane and liquid oxygen have been used on several recently developed LPREs. This propellant combination provides a relatively high specific impulse, while offering a significantly higher density compared to liquid hydrogen. The storage temperatures of liquid methane and oxygen are also similar, allowing for simplifications in propellant tank design [1]. These propellants also require an external ignition source.

Methane has a relatively high auto-ignition temperature compared to some liquid fuels, such as kerosene [42]. This increases the heating requirements for the resonator. Both the ignition delay time, as well as the auto-ignition temperature depend on the mixture ratio of the propellants. This poses a challenge for non-pre-mixed designs, as the separate injection of propellants does not guarantee a specific mixture ratio at the tip of the resonance cavity. The adiabatic flame temperature of the combustion of oxygen and methane is shown in Figure 2.17, calculated using NASA CEA [43]. The rich and lean extinction limits of the reaction are shown, along with the stoichiometric mixture ratio [44].

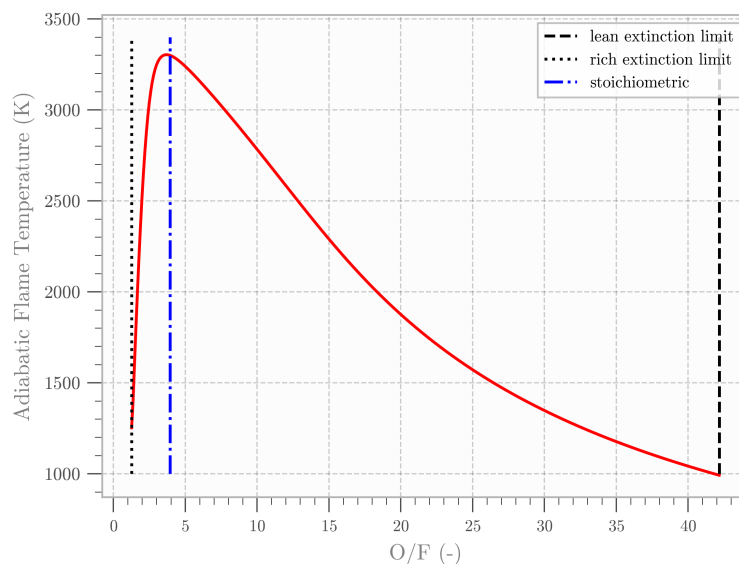


Figure 2.17: Adiabatic flame temperature of O_2/CH_4 as a function of oxidiser to fuel ratio, calculated under frozen equilibrium conditions at a pressure of 10 bar.

For many rocket engine ignition systems, operating at a low equivalence ratio is advantageous. As shown in Figure 2.17 the adiabatic flame temperature can be significantly reduced for lean propellant mixtures. This can eliminate the need for active cooling and extends the possible firing time of the ignition system [12].

Both the ignition delay time, as well as the auto-ignition temperature depend on the mixture ratio of the propellants [45] [42]. The shortest ignition delay of oxygen and methane mixtures is observed at equivalence ratios between $\phi = 1$ and $\phi = 1.3$ [45]. For thermo-acoustic igniters, a short ignition delay is generally desirable. The compression cycle during of the jet regurgitant mode only produces high cavity gas temperatures for a very short time, after which the gas mixture expands again and the temperature reduces. The wall of the resonance cavity retains a significant amount of heat during resonance that is returned to the flow during the expansion process. This means that a low auto-ignition temperature in combination with a short ignition delay can increase igniter reliability. The mixture ratio chosen for the igniter design represents a trade-off between allowable burn time and ignition reliability. The required burn time and energy release of the igniter is dictated by the requirements of the main propulsion system [2].

2.8. Numerical Models of Resonance Heating

Several numerical models have been developed to study the effect of resonator geometry and operating point on heat generation. The simplest such models focus on the flow inside the resonance cavity. Shock tube equations or one-dimensional Euler equations are used to determine the flow profile during JRM, with empirical relations used to account for heat transfer to the cavity wall. Predicting the interaction between the cavity and the under-expanded jet requires the use of multi-dimensional models, significantly increasing the complexity of the simulation and associated computational cost.

2.8.1. Zero-Dimensional Models

As shown in [section 2.3](#), the flow inside a resonance cavity can be approximated using models developed for shock tubes. Brocher and Maresca [27] use an analysis of integral quantities of heat generation and loss to determine the temperature of the cavity wall.

The mechanisms of heat generation and loss have been discussed in detail in [section 2.4](#). The advantage of such a model is that it considers the total production and exchange of heat independent of resonance frequency. It is therefore broadly applicable to all driving gases and geometrical parameters. It is also very simple to implement and is valuable for understanding the impact certain operational parameters, such as total pressure or driving gas have on heating performance.

This model has shown reasonable accuracy in predicting maximum wall temperatures for tests with air and helium. The accuracy reduces significantly at high ratios of cavity temperature to upstream total temperature. For $T_{max}/T_t > 2$, radiation to the environment contributes significantly to the total amount of heat lost [27]. As this is not accounted for in the model, the solution diverges more at these temperature ratios.

2.8.2. One-Dimensional Models

The flow inside the resonance cavity can be modelled using one-dimensional unsteady Euler equations. This allows for the inclusion of friction effects and heat transfer along the length of the cavity [31]. The mass, momentum and heat equations are solved numerically.

Kawahashi and Suzuki show how the one-dimensional approach improves the accuracy of the predicted flow field over the shock tube based flow models [31]. An important limitation of the one-dimensional approach to flow modelling is that the mechanism initiating resonance cannot be resolved. The shock-cavity-interaction is inherently a multi-dimensional process [21]. This approach is sensible if a resonance mode and fundamental frequency can be assumed a priori. Closure for the heat equation can be provided using empirical models for the friction coefficient and heat transfer coefficient. Kawahashi and Suzuki use conservation of entropy and a differential form of the entropy equation to solve for the temperature of a fluid element [31]. The wall is modelled using unsteady heat conduction along the length of the cavity. Here it is assumed that the wall is very thin and possesses a uniform temperature across its thickness. The resulting model is computationally inexpensive compared to a multi-dimensional approach, and allows for the simulation of time dependent heat generation.

2.8.3. Multi-Dimensional Euler Models

The flow field inside resonance has been studied extensively using Computational Fluid Dynamics (CFD). These studies tend to focus on an analysis of the driving mechanisms behind the resonance and on the temperature of the gas entrained inside the cavity. Most of these studies take advantage of the symmetry inherent to most igniter designs and solve a 2D axis-symmetric system. This significantly reduces the required computational resources over solving a three-dimensional problem with similar spatial resolution. As opposed to the other simplified models outlined above, this allows for resolving of the driving mechanism behind the acoustic resonance [38].

Some studies have used the compressible Euler equations to model the driving mechanisms behind acoustic resonance. Here flow is assumed to be adiabatic and inviscid [17]. This reduces the computational cost of simulating the two-dimensional flow field compared to methods that include turbulence models. It has been used by Lebedev and Bocharova [38] to study the driving mechanism behind acoustic resonance. Here a variety of nozzle gap distances and inlet geometries of the acoustic cavity are compared. These results are used to establish a relation between the Strouhal number of the oscillations and the nozzle gap spacing [38]. Similarly, Chang and Lee [46] also use a form of compressible Euler equations to model a Hartmann-Sprenger tube. In this numerical study, the resonance is initiated by a periodic variation in upstream mach number, instead of a sonic, converging nozzle. This periodic variation in the inflow boundary condition reproduces the pressure wave patterns expected in the Jet Regurgitant Mode. The study further claims that when a simulation assumes the presence of a Jet Regurgitant Mode the effects of turbulence can be neglected [46]. This statement appears to be in reference to the flow field inside the igniter, as heat transfer was not considered in this study.

2.8.4. Multi-Dimensional RANS Models

The interaction between an under expanded jet and an acoustic cavity can be modelled using unsteady Reynolds-Averaged Navier-Stokes (URANS) in conjunction with a turbulence model. The RANS equations themselves do not resolve turbulence, but the effect of turbulence on the mean flow can be modelled [47]. Using URANS equations for the flow inside the resonance cavity allows for modelling the effect of turbulence on heat transfer and wall friction.

Bauer et al. conducted a wall resolved simulation with a realizable $k-\epsilon$ turbulence model and Menter-Lechner wall treatment [48]. y^+ values below 1 are achieved along the length of the resonator. The authors note that there are situations in which the flow inside the boundary layer flows in reverse direction compared to the core flow of the resonator. This complex flow profile with high local gradients poses some challenge for numerical stability [48]. A similar numerical approach is used by Afzali and Karimi [49].

Bauer et al. find that turbulence generally plays an important role in the prediction of the operating mode of the Hartmann-Sprenger tube [48]. The authors speculate that this may be due to the effects of turbulence on the pressure distribution within the free jet. This directly contradicts the statements made by Chang and Lee [46].

A direct comparison of a three-dimensional and a two-dimensional axis-symmetric URANS simulation has been performed by Bauer and Haidn [50]. The two-dimensional simulation shows high amplitude, periodic pressure oscillations, while these same oscillations decay after two flow cycles in the three-dimensional simulation. Experimental results from the same operating point show a stable jet regurgitant mode. The pressure trace of the two simulations is shown in [Figure 2.18](#).

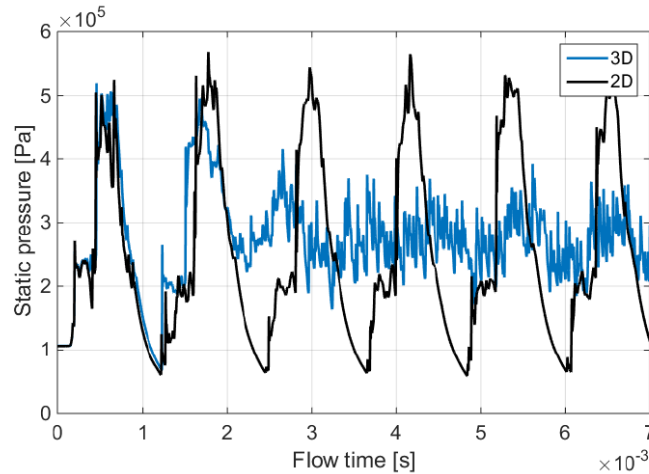


Figure 2.18: Comparison of the pressure evolution of 2D and 3D URANS simulations, taken from Bauer and Haidn [50]

The authors attribute this decay in JRM to the highly non-uniform pressure field in front of the entrance of the resonance cavity. In the three-dimensional simulation this pressure showed strong non-uniformities in circumferential direction [50]. Iwamoto identifies a uniform pressure gradient in front of the resonator inlet as a requirement for JRM to be sustained [26]. The non-uniformity results in uneven pressure recovery behind the under-expanded jet and a decay in oscillation [50]. In this particular case it is found that the 2D axis-symmetric simulation more closely matches experimental results [50]. The validity of these results is difficult to assess with only a single three-dimensional CFD simulation available.

For this thesis project the prediction of the operating mode based on operational parameters is particularly relevant. As such 2D axis-symmetric CFD is required to resolve the phenomena responsible for initiating and sustaining resonance. The modelling of heat transfer though the cavity wall also requires the use of a turbulence model.

The switch between operating modes has been studied numerically by Bauer et al. [12] and by Lebedev and Bocharova [38]. In both of these studies a limited number of simulations are compared to experimental data. The onset of JRM is shown to be predicted for some operating conditions and resonator geometries. A more detailed comparison of these models to experimental data is needed to conclusively demonstrate that the onset of JRM can be predicted over a large range of geometrical parameters and different driving gases. For a numerical model to be useful as part of the design process of a resonance igniter, it must have a low computational cost and be able to predict which parameters lead to the highest rates of heat generation. The numerical model developed and validated as part of this study, aims to predict both the onset of the JRM, as well as the geometrical and operational parameters leading to the highest rates of resonance heating. This is to be accomplished while having a lower computational cost than most of the existing multi-dimensional models presented here.

2.9. Numerical Discretisation

For numerical flow models of thermo-acoustic resonance requires accurately resolving the stationary and moving shock waves. High gradients in flow velocity, pressure and density, as well as reverse flow in the resonator boundary layer pose challenges for numerical stability [12]. This section briefly outlines some of the numerical methods employed to solve these highly compressible flows. This is limited to the context of finite volume methods, as that is the most common approach used for similar problems [48] [49] [38].

2.9.1. Spatial Discretisation and Convective Schemes

High Mach number flows generally require special treatment of the advective terms of the Navier-Stokes equations. This allows for the accurate computation of fluxes across a discontinuity, such as a shock wave. Several approximate Riemann solvers can be used to determine the flux over cell faces. The choice of convective scheme is typically based on the desired order of accuracy, as well as the amount

of numerical dissipation required to stabilise the simulation.

A possible choice for an approximate Riemann solver is a first order upwind method. These offer high degrees of numerical stability and reduced computational effort. Lebedev and Bocharova [38] use a first order Gudonov scheme with results that compare well to experiments conducted on under-expanded jets. The use of first order upwind schemes introduces a high degree of numerical dissipation. The flow over a sharp discontinuity is therefore strongly attenuated. Several upwind schemes have been developed, with different degrees of numerical dissipation. The Roe approximate Riemann solver is a popular solver based on a Gudonov method, implement in many CFD packages. The Advection Upstream Splitting Methods (AUSM) have been shown to perform well near sharp discontinuities [51]. However, all of these first order upwind schemes are extremely dissipative. In order to limit this behaviour, higher order reconstruction is often employed [49] [48]. Here higher order spatial accuracy can be obtained by introducing non-linearity to a Gudonov-type scheme. Monotonic Upstream-centered Scheme for Conservation Laws (MUSCL) reconstruction can achieve second order accuracy but requires slope limiters to prevent spurious oscillations near discontinuities.

In this thesis a first order classical Roe scheme is used to approximate convective fluxes. Although highly dissipative it is shown to have good predictive capability and excellent convergence characteristics over all geometrical and operating parameters. This allows for the same simulation to be used for a wide variety of operating conditions, while providing results that are sufficiently accurate to predict the operating mode of the igniter, as well as the geometrical parameters that cause the highest rates of resonance heating.

2.9.2. Time Discretisation

For time integration, the Courant-Friedrichs-Lewy (CFL) condition poses a limit on the largest time step possible for a given time integration scheme to remain stable. For high flow velocities and fine grid sizes the CFL condition forces a very small time step on explicit time integration schemes [47]. This necessitates very high iteration numbers and high computational cost. The time step can be increased significantly (thereby reducing the total number of steps required) using a dual time stepping technique with implicit time integration. Here a quasi steady state problem is solved between each time steps. This leads to a higher computational cost per time step but allows for significantly coarser time steps [48]. This method is also implemented in this study to reduce the computational cost of the large number of simulations performed.

3

Research Objectives

Thermo-acoustic igniters present a promising concept for rocket engines that require a high number of ignition cycles. Despite some advantages over spark torch igniters, no resonance igniters have been used as flight hardware as part of a launch vehicle or in-space propulsion system [12]. In [chapter 2](#) several gaps in the understanding of thermo-acoustic heating have been identified. Research gaps related to both resonance igniter design and the modelling of thermo-acoustic heating are summarised in this chapter. These are later reformulated as research objectives and research questions for this thesis.

3.1. Research Gap

Several successful prototypes have been demonstrated by Phillips & Pavli [33], Bauer et al. [12] and Marchan [28] [34], among others. The proposed designs for thermo-acoustic igniters operate with a variety of driving gases and propellant combinations. The small number of tested designs makes drawing universal conclusions about the operating modes of the igniters and design principles difficult. The disagreement in existing literature about which conditions produce a stable jet regurgitant mode and which result in the highest rates of resonance heating has been outlined in [section 2.6](#). A more unified understanding of this switch in operating modes is crucial for creating design guidelines and predicting igniter behaviour under a variety of operating conditions. Specifically, the influence of the area upstream of the inlet to the resonance cavity, and the surrounding combustion chamber requires further study.

In recent years several rocket engines have been developed that use liquid oxygen and methane [1]. Gaseous oxygen (GOx) and gaseous methane are therefore particularly interesting propellants for resonance igniters. Bauer et al. have demonstrated ignition with these propellants in a pre-mixed configuration [12], commonly used when both propellants are gaseous, as outlined in [section 2.5](#). This thesis aims to test these same propellants in a non-pre-mixed configuration, demonstrating design options that are inherently safer to test. Pre-mixing gaseous propellants carries an inherent risk of flash-back. This can cause the flame front to travel into one of the propellant supply lines, and can lead to catastrophic failure of the system. Introducing the fuel and oxidiser into the combustion chamber separately significantly reduces the probability of flashback, but introduces additional challenges discussed as part of this study.

Any new igniter design requires extensive testing to find a stable operating mode that produces sufficient resonance heating, and yet more testing to determine an optimal operating regime. The stability of the operating point of a resonance igniter also depends on the conditions of the upstream gas. In any practical application of such devices, the supply pressure and temperature of the gas may vary over the course of a mission. If the igniter is used as part of a pressure fed propulsion system, it may experience some drop in supply pressure over the course of the mission. Stabilising the heat generation of the igniter over the expected mission envelope is therefore a priority for any practical design [22]. Testing an igniter over all possible permutations of operating conditions is costly and time consuming, and

is ideally reserved for igniter qualification tests. A numerical model that is able to accurately predict heating performance under a wide range operating conditions is therefore important during the design phase of the igniter.

Some studies have produced numerical models capable of simulating thermo-acoustic effects in Hartmann-Sprenger tubes [49] [48] [50] [38]. With the exception of Bauer et al. [48] and Lebedev & Bocharova [38] very few models are able to predict the switch between the high frequency jet screech mode and lower frequency jet regurgitant mode. In both cases these models are validated over a range s/d_{throat} . Lebedev & Bocharova [38] include additional validation over changing depth of a cylindrical resonance cavity. No validation has so far been conducted with varying driving gases or using different cavity inlet geometries in the same experimental setup. None of the existing models are shown to predict the set of geometrical and operating parameters that result in the highest rates of heat generation.

The focus of the numerical model, developed as part of this thesis, is to simulate the onset and sustainment of thermo-acoustic heating. It is important for this model to be able to predict which set of operational parameters and nozzle gap spacing cause the highest rates of resonance heating and thereby showing at which point ignition is likely to occur. Resonance heating experiments with different igniter geometries, operating conditions and driving gas are used for model validation.

3.2. Research Objectives

The adoption of thermo-acoustic igniters for liquid propellant rocket engines requires a better understanding of the geometrical and operational parameters that initiate resonance heating. Ideally these conclusions are generalisable to any resonance igniter and thereby useful during igniter design. Numerical models can also be used as part of this process. The complexity of these simulations necessitates a trade-off between the accuracy of the model and its ability to simulate a wide range of geometrical and operational parameters. A computationally efficient model that is capable of predicting the onset of effective resonance heating can be used for igniter optimisation, or analysing the sensitivity of the system to changing inflow and environmental conditions. Extensive testing is required to validate such a model and to qualify any resulting design.

This thesis aims to contribute to the understanding of both the operation and simulation of thermo-acoustic igniters. The research objective of this study is:

To investigate the performance envelope of a non-pre-mixed oxygen/methane resonance igniter experimentally, and develop a numerical model capable of predicting the operating mode of the igniter based on nozzle gap spacing and operational parameters.

3.3. Research Questions

In order to reach this objective, several research questions are identified based on gaps in existing literature. Two primary research questions are identified. The first question focuses on the predictive capacity of the numerical model. Three sub-questions are identified based on the development of the numerical model.

Could a simplified numerical model predict the heating performance of a thermo-acoustic igniter as a function of nozzle gap spacing and operating point?

1. How accurately can the switch between the jet screech mode and jet regurgitant mode be predicted numerically and reproduced experimentally?
2. How accurately can these simulations predict which nozzle gap spacing and operating points cause high rates of resonance heating?
3. What measuring equipment can be used to accurately determine the operating mode of small-scale thermo-acoustic igniters, while not interfering with the acoustic resonance?

The first sub-question relates to the connection between thermo-acoustic heating and the operating modes outlined in [section 2.2](#). Accurately predicting this switch and how it is influenced by the nozzle gap spacing and operating point (sub-question two) influences the value of such a model for the igniter design process. The third sub-question relates to the validation process of the model. The small scale

of the resonator means that it is important to consider how the resonance frequency be measured without altering the onset of an operating mode.

The second primary research question centres around the viability of using gaseous propellants in a non-pre-mixed configurations. Two additional sub-questions are identified concerning the experiments with a prototype igniter.

How does the use of non-pre-mixed, gaseous propellants impact the ignition reliability of a thermo-acoustic igniter?

1. How stable is the resonance heating with respect to changing upstream pressure. Which upstream pressure provides the best conditions for ignition?
2. What are the fundamental differences in the resonance heating envelope when using different driving gases?

The stability of the resonance with respect to changing upstream pressure is an important operational parameter for the use of these igniters in launch vehicles or as part of in-space propulsion systems. Comparing the effect of different driving gases on the resonance heating envelope is important to assess how resonance heating is affected by changing fluid properties.

4

Experimental Approach and Simulation

This chapter outlines the experimental and numerical approach taken to answer the research questions posed in [chapter 3](#). An overview of the igniter prototype is given, together with an overview of the conducted experiments. The particular challenges associated with numerical modelling of thermo-acoustic heating are introduced. The validation strategy for the model is outlined.

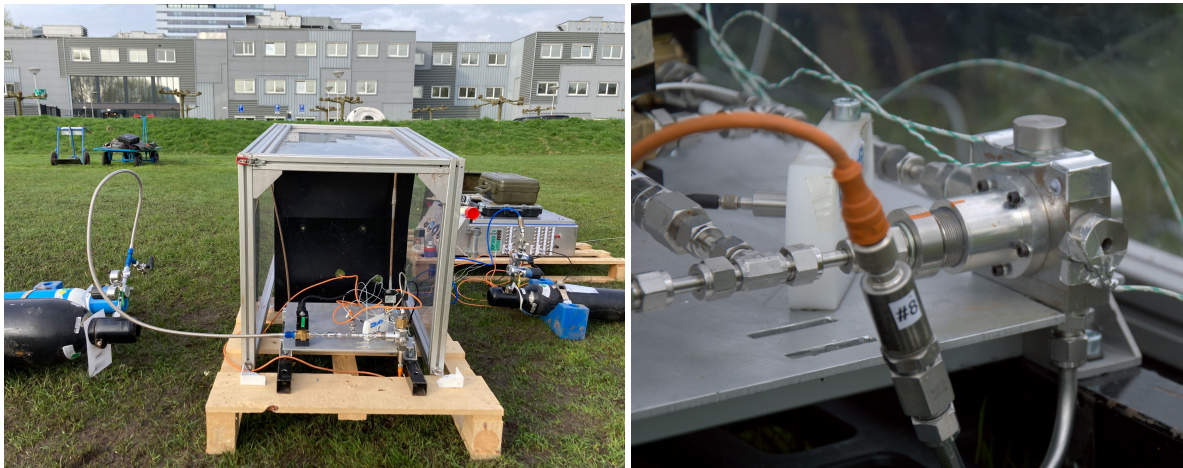
4.1. Experimental Approach

Several experimental campaigns were conducted with the support of Delft Aerospace Rocket Engineering (DARE), a student rocketry society associated with Delft University of Technology. DARE is active in the development of liquid, hybrid and solid rocket motors, recovery systems, rocket structures and electronics.

As part of this thesis a test setup was designed that allows for resonance heating experiments with gaseous oxygen and gaseous nitrogen. A cylinder of gaseous methane was added to the setup to supply fuel for combustion experiments. A resonance igniter prototype was designed to feature a replaceable resonance cavity, inlet and exhaust nozzles, as well as variable s/d_{throat} . The modularity of the design allows for rapid testing of different resonator and cavity inlet geometries. Replacing the exhaust nozzle with one of a different throat diameter results in a different nozzle pressure ratio. The mixture ratio and the injection pattern of the methane supplied to the chamber can also be adjusted by replacing the fuel injector. All of these modifications to the igniter can be performed rapidly between tests and allow for efficient testing of a design space.

The detailed design of the igniter prototype and propellant feed system are shown in [section 5.3](#). The requirements set for the igniter design are outlined in [Appendix A](#). These include safety requirements the igniter and feed system, as well as design requirements. Requirements are also set for the data acquisition system and instrumentation based on the research objectives. Details on the manufacturing of the igniter and technical drawings of components and assembly are shown in [Appendix E](#). Testing of an ignition system operating on pressurised oxygen and methane carries some inherent risk. A full risk assessment including mitigation strategies is presented in [Appendix F](#), together with structural failure analysis of the igniter design. The test procedures guiding the experimental campaigns are included in [Appendix G](#) for future reference.

An overview of the igniter design and the fluid system are presented in [section 5.3](#). Using this igniter prototype, a total of 95 resonance heating tests were conducted, along with six combustion tests. An overview of the test setup in resonance heating configuration is shown in [Figure 4.1a](#), with an image of the igniter in [Figure 4.1b](#).



(a) Resonance igniter test setup configured for a heating test with gaseous oxygen.

(b) Igniter prototype during an ignition test.

Figure 4.1: Overview of the test setup developed as part of this thesis.

4.2. Numerical Approach

The fluid dynamic simulation of the acoustic resonance phenomena requires accurately resolving stationary and moving shock waves, as well as very high gradients in flow velocity, pressure and density. The choice of spatial discretisation, time marching method are relevant for the accuracy of the simulation, as well as numerical stability. The Open Source CFD software SU2 [52] is used for the numerical model developed as part of this thesis. [section 5.4](#) outlines the computational domain and full simulation setup used for the numerical studies. An overview of the 2D axis-symmetric simulation domain is shown in [Figure 4.2](#), together with a visualisation of the flow field during part of the inflow cycle of the jet regurgitant mode.

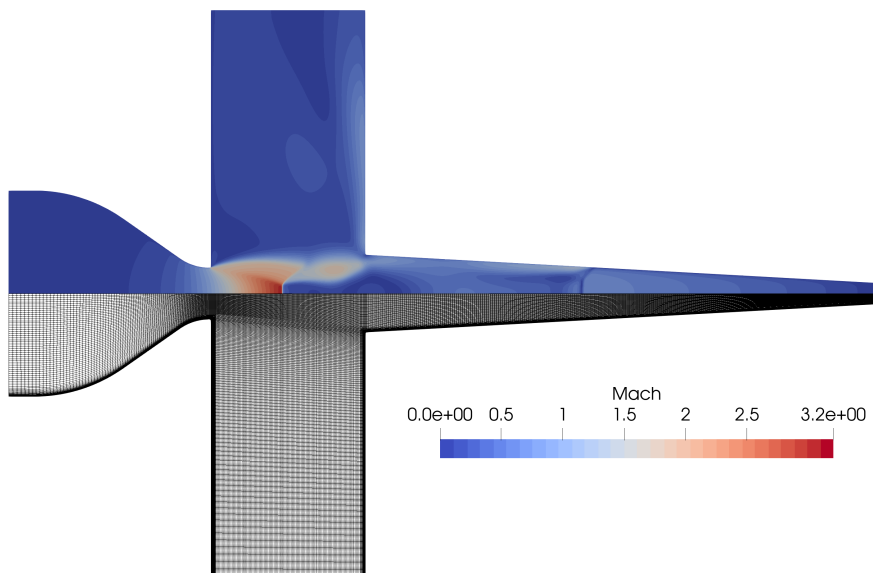


Figure 4.2: Simulated Mach number during the inflow cycle of JRM (above), with visualisation of the computational grid at 50% of the nominal number of nodes (below).

A mesh refinement study is carried out to verify the simulation and quantify the error of the first-order spacial and second-order time discretisations. The simulation is also extensively validated using the gathered experimental data. The predicted resonance frequency is validated over several nozzle gap distances, using two different driving gases and using two different cavity inlet shapes. Additional model validation is performed using an analytical model for shock tube flow. The model validation is shown in [section 5.6](#), with additional validation cases presented in [Appendix B](#). Additional numerical results of the flow inside the resonator are shown in [Appendix D](#).

5

Thesis Paper

This study investigates the use of a non-pre-mixed GOx/CH_4 resonance igniter for liquid propellant rocket engines. Resonance heating at varying nozzle gap spacing for both oxygen and nitrogen is investigated both experimentally and numerically. High frequency microphone data is used to experimentally determine the operating mode of the igniter. Temperature measured on the outside of the resonator tip is used to evaluate heating performance at specific set points. The Open Source CFD software SU2 is used to create a numerical model, capable of accurately predicting the switch in igniter operating point, as well as the operational parameters leading to the highest rates of thermo-acoustic heating. Ignition attempts show that the separate injection of methane into the combustion chamber causes severe disruption of resonance heating, preventing the mixture from igniting.

5.1. Introduction

In the context of rocket propulsion, *green* propellants refer to combinations of fuel and oxidiser that are less toxic and less environmentally hazardous than many of the currently used storable propellants [1], such as MMH and MON. In 2011 hydrazine was added to a European Union candidate list of substances of very high concern through REACH (registration, evaluation, authorisation of chemicals)[3]. The high carcinogenic potential of hydrazine and its derivatives being the primary motivation. This leads to any test or integration facility requiring specialised personal protective equipment, trained operators and environmental permits to work with these propellants [4]. The difficulties associated with propellant handling have led to an increased interest in developing less toxic alternatives [1].

The use of non-hypergolic, cryogenic propellants are being investigated as potential alternatives for longer duration space missions [8]. These, however, require the use of an external ignition system. At the same time, more orbital transfer vehicles and upper stages of rockets are being developed, that rely on multiple re-ignitions of their main propulsion system. As a result there is a need for highly reliable, light-weight ignition systems, capable of a high number of ignition cycles.

Thermo-acoustic igniters (sometimes referred to as *resonance* igniters) present a attractive solution. They feature the power and reliability of a spark torch igniter, with reduced system complexity by omitting an external ignition source. Instead, they use the interaction between a supersonic gas flow and an acoustic cavity to initiate combustion. The use of a thermo-acoustic igniter is advantageous for a system that requires multiple re-ignitions during a single flight. These might include the main engines of a launch vehicle (specifically if propulsive landing is required), upper stage propulsion systems, or orbital transfer vehicles. Gaseous oxygen is often used to drive acoustic resonance and can be combined with a variety of gaseous and liquid fuels inside the igniter, such as kerosene [28] [34], hydrogen [33], or methane [12].

The use of such devices as rocket engine igniters has been studied since 1967 [15]. However, to date, none have been used as flight hardware [12]. The challenge in designing a reliable resonance igniter lies in maintaining an operating regime in which enough heat can be generated [12]. Despite multiple

experimental and numerical studies of thermo-acoustic resonance, few universal conclusions can be drawn about which resonator geometry and operating point result in optimal heating performance. This extends to the two main operating modes of the acoustic resonance and under what conditions they are initiated. Some disagreement exists about which of the two modes produces the highest rates of resonance ignition and which are more suitable for reliable ignition.

This study shows that a simplified numerical model can be used to accurately predict the switch in operating mode of the resonance igniter and the onset of resonance heating. The numerical model is extensively validated with an experimental setup using tests with oxygen, nitrogen and two different resonator inlet geometries. A prototype of a resonance igniter using gaseous oxygen and gaseous methane is used to test non-pre-mixed ignition. The phenomena associated with thermo-acoustic resonance are briefly introduced in [section 5.2](#). The non-pre-mixed resonance igniter, designed as part of this study, is described in [section 5.3](#). [section 5.4](#) describes the numerical model, including a mesh refinement study and a discussion of the importance of using non-ideal equation of state for these simulations. The experimental method and data acquisition is presented in [section 5.5](#). Results from the resonance heating experiments are shown in [section 5.6](#), including the validation of the numerical model. The results of the ignition tests are outlined in [section 5.7](#).

5.2. Thermo-acoustic Resonance

A thermo-acoustic igniter uses the interaction between an under-expanded supersonic gas flow and an acoustic cavity to generate sufficient heat to initiate combustion. A mixture of reversible and irreversible processes raise the temperature of the gas entrained inside the cavity [21]. Two different acoustic modes can reliably produce high gas temperatures inside the tip of the cavity. The high frequency jet screech mode (JSM) or the lower frequency jet regurgitant mode (JRM) can be initiated under different operational parameters or igniter geometry [21]. Sustaining one of these operating modes over many resonance cycles is critical for achieving high gas temperatures and consistent ignition.

The operating mode and the effectiveness of thermo-acoustic heating primarily depend on the interaction of shock structures with the acoustic cavity. This makes the relative position of the under-expanded jet to the entrance to the cavity particularly important [21].

The shock structure of an under-expanded jet is dictated by the ratio of total pressure in the inlet nozzle to ambient pressure surrounding the under-expanded jet, p_t/p_∞ . This is commonly referred to as the Nozzle Pressure Ratio (NPR ¹). A jet that is moderately under-expanded features a diamond pattern of oblique shock waves. This generally occurs at $2 < \text{NPR} < 4$ [19]. Resonance heating has been demonstrated in weakly under-expanded gas flows, but appears significantly more effective at higher NPR [33]. If the pressure ratio increases to $4 < \text{NPR} < 7$ the jet forms a barrel structure with a Mach disk, illustrated in [Figure 5.1](#). The flow through an under expanded jet experiences alternating compression and expansion along the centreline as it passes through the shock- and expansion waves.

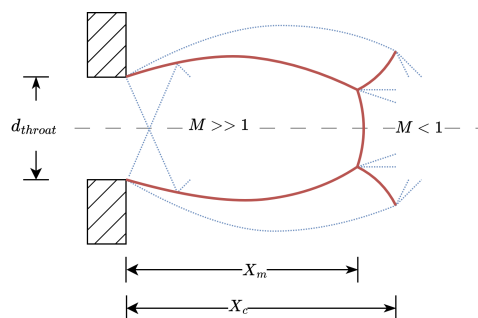


Figure 5.1: Illustration of the structure of the shock structure of a single cell in an under-expanded jet at $4 < \text{NPR} < 7$. Based on the description by Duronio, Villante, and Vita [19]. X_m denotes the distance between the nozzle exit and the Mach disk and X_c the distance to the end of the first shock cell.

¹This parameter is almost exclusively found in western literature on the subject. By contrast literature from countries, formerly part of the Soviet-Union, use $n = p_e/p_\infty$, the ratio of static pressure in the throat of the nozzle to ambient pressure [38].

Equation 5.1 relates the location of the Mach disk X_m and the end of the first shock cell X_c to the NPR, exit Mach number M_e and the ratio of specific heats of the driving gas γ [28].

$$\begin{aligned}\frac{X_m}{d_{throat}} &= (0.8 + 0.085 \cdot (M_e - 2.1)^2) \cdot M_e \cdot \left(\text{NPR} \cdot \left(1 + \frac{\gamma - 1}{2} M_e^2 \right)^{\frac{-\gamma}{\gamma - 1}} - 0.5 \right)^{0.5} \\ \frac{X_c}{X_m} &= 1.3 + 0.5 \cdot \left(\text{NPR} \cdot \left(1 + \frac{\gamma - 1}{2} M_e^2 \right)^{\frac{-\gamma}{\gamma - 1}} \right)^{-3}\end{aligned}\quad (5.1)$$

The two most influential parameters for the interaction between the cavity and the under-expanded jet are, therefore, the NPR and the normalised nozzle gap spacing s/d_{throat} . The effectiveness of resonance heating also depends on the upstream total pressure, the driving gas and the geometry of the resonator.

The choice of driving gas directly impacts both the resonance frequency of the cavity and the rate of resonance heating [35]. The molecular weight and ratio of specific heats are particularly important. Mono-atomic gases, such as helium and argon exhibit rapid resonance heating, with di-atomic gases, such as oxygen being slightly less effective [35].

The shape of the resonance cavity itself influences the pressure oscillations inside the cavity, as well as heat generation. The use of a (semi-) conical resonance cavities significantly increasing maximum temperature during resonance heating [33] [12] [40] [28]. Three non-dimensional parameters are used to define the shape of this cavity. The cavity length L/d_{throat} , the cavity inlet diameter D/d_{throat} and the convergence angle of the cavity α .

The effect of s/d_{throat} , upstream total pressure and the shape of the cavity inlet on resonance heating are explored as part of this study. Resonance heating experiments are conducted with both oxygen and nitrogen.

5.2.1. Inlet and Exhaust Nozzles

The under-expanded jet driving acoustic resonance requires the flow through the inflow nozzle to be choked. Equation 5.2 can be used to estimate the mass flow of the driving gas during resonance heating [16].

$$\dot{m} = \frac{C_d A p_t}{\sqrt{T_t}} \sqrt{\frac{\gamma}{R}} M \left(1 + \frac{\gamma - 1}{2} M^2 \right)^{-\frac{\gamma + 1}{2(\gamma - 1)}} \quad (5.2)$$

Here C_d is the discharge coefficient, p_t is the total pressure, T_t the total temperature, A is the cross sectional area of the throat, R is the specific gas constant and γ the ratio of specific heats. The mass flow determined using Equation 5.2 is highest when $M = 1$.

Both Bauer et al. [12] and Marchan [28] have shown that adding a choked nozzle in the exhaust flow can stabilise resonance with respect to changing total pressure of the inflow. Assuming that the driving gas behaves like an ideal gas and does not experience viscous losses throughout the resonance chamber, the NPR only depends on throat and exhaust area, as shown in Equation 5.3. Using Equation 5.2 and assuming that the mass flow entering through the nozzle is the same as that leaving through the exhaust nozzle, the NPR can be expressed in terms of the ratio between the nozzle exit, A_{exit} and the throat area, A_{throat} . This holds as long as p_t is sufficiently high to ensure that both inlet and exhaust nozzle remain choked.

$$\text{NPR} = \frac{A_{exit}}{A_{throat}} \quad \text{if } p_t \geq p_\infty \cdot \text{PR}_{critical} \cdot \text{NPR} \quad (5.3)$$

Here p_∞ denotes the ambient pressure downstream of the exhaust nozzle, p_t is the total pressure of the inflow and $\text{PR}_{critical}$ the critical pressure ratio of the driving gas. A constant NPR with respect to upstream total pressure means that the optimum s/d_{throat} also remains constant as the upstream pressure changes [12].

5.2.2. Fuel Injection and Ignition

The propellants used in a resonance igniter are usually chosen to match those used in the main propulsion system, to minimise complexity. In most resonance igniters, gaseous oxygen is used as the oxidiser [28]. This can be paired with either a liquid or a gaseous fuel. When using a liquid fuel, such as kerosene [28], or RP-1 [34], gaseous oxygen is typically used as the driving gas for resonance heating, with the fuel injected separately into the combustion chamber. Some of the injected fuel mixes with the under expanded oxygen flow and is entrained into the resonance cavity. The ongoing resonance heating, as well as the heated walls of the cavity tip provide the necessary activation energy to ignite the mixture. The separate injection of the liquid fuel into the combustion chamber introduces some uncertainty in the mixture ratio at the tip of the cavity, as it is difficult to predict how much of the fuel is entrained together with the oxygen. The mixture ratio influences both ignition delay and auto-ignition temperature [42].

Thermo-acoustic igniters using gaseous fuels rely on pre-mixing the propellants and using this mixture to drive resonance heating [33]. This ensures a specific mixture ratio inside the resonance cavity, and has been demonstrated using gaseous hydrogen [33], and more recently using gaseous methane [12]. Pre-mixing propellants introduces a significant risk of flashback into the propellant supply lines.

This study aims to demonstrate resonance ignition with gaseous oxygen and gaseous methane in a non-pre-mixed configuration. Gaseous oxygen is used for resonance heating. After the cavity tip has reached a sufficient temperature, methane is injected perpendicular to the resonating oxygen. Mixing with the under-expanded jet allows some of the methane to be entrained into the resonance cavity, creating the conditions necessary for ignition.

5.3. Thermo-Acoustic Igniter Design

An experimental setup was designed for resonance heating and ignition tests with gaseous oxygen and methane. Nitrogen was substituted as the driving gas during commissioning experiments. The supply pressure of the driving gas and the fuel can be adjusted between 8 bar and 25 bar. The igniter design allows for varying s/d_{throat} between experiments and features a replaceable resonance cavity, as well as modular inlet and exhaust nozzles to be able to vary the NPR.

5.3.1. Igniter Design

An overview of the igniter assembly is shown in [Figure 5.2](#). The oxygen injector (2) has a throat diameter of 2 mm (H7 tolerance). s/d_{throat} can be adjusted from 1.5 to 4 using an M24x1.0 thread interfacing between the oxygen injector and the injector support (1). The combustion chamber (3) serves as a mounting point for the oxygen inlet support. The main axis of the chamber is perpendicular to the resonating flow of oxygen. Methane is injected at the top of the combustion chamber using a replaceable injection element (5). The resonator (4) is mounted to the chamber using four M3 bolts (grade 8.8). An aluminium gasket provides a seal at the interface between resonator and combustion chamber. Similar gaskets are used at the interfaces to the methane injector, exhaust nozzle and oxygen injector support. A piston seal made from FKM provides a seal between the chamber and the oxygen inlet. Both the methane injector (5) and exhaust nozzle (6) feature external threads that engage with the combustion chamber. Concentric alignment of the oxygen injector and the inlet resonance cavity is critical for repeatable operation with different resonators. As such, the mounting holes of the oxygen injector and the resonator were milled on the same setup and later inspected. Technical drawings of the igniter assembly and all components are shown in [Appendix E](#).

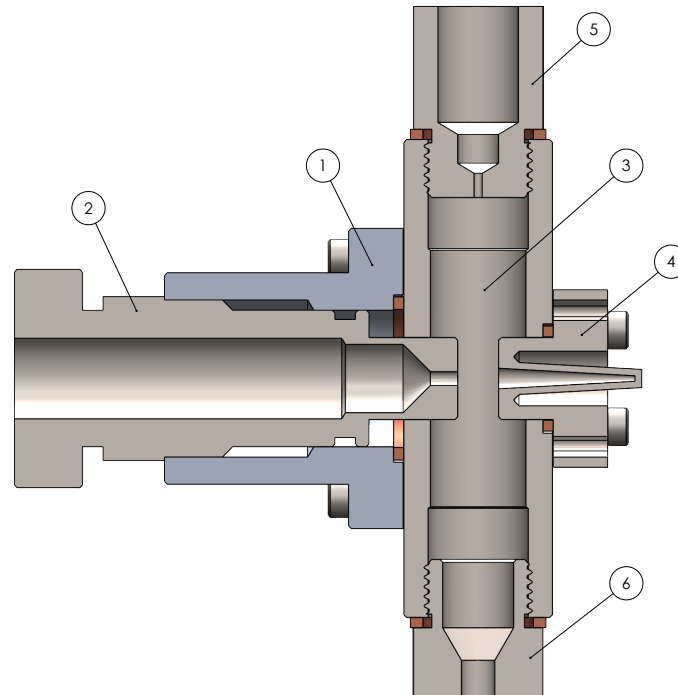


Figure 5.2: Section View of the igniter assembly, (1) oxygen injector support, (2) oxygen injector, (3) combustion chamber, (4) resonator, (5) methane injector, (6) exhaust nozzle.

The oxygen injector, combustion chamber, methane injector and exhaust nozzle are manufactured from 1.4305 stainless steel. The diameters of all choked orifices, the oxygen and methane inlet and the exhaust nozzle are determined using Equation 5.2. A discharge coefficient of 0.9 is assumed for all orifices, based on numerical results from 40° conical converging nozzles in gaseous, choked flow at an NPR of 6 [53]. Table 5.1 summarises the high level design and operational parameters of the igniter.

Table 5.1: Igniter Design and Operational Parameters

Parameter	Value	Unit
Fuel	Gaseous Methane	(-)
Oxidiser	Gaseous Oxygen	(-)
Fuel pressure	8 - 25	bar
Oxidiser pressure	8 - 25	bar
Oxidiser mass flow at 25 bar	17.73	g/s
Fuel mass flow at 25 bar	4.43	g/s
Mixture ratio	4	(-)
d_{inj,O_2}	2	mm
d_{inj,CH_4}	1.2	mm
Nozzle diameter	5.2	mm
s/d_{throat}	1 - 4	(-)

5.3.2. Resonator

The conical resonator is 3D printed from 17-4 PH stainless steel using Selective Laser Melting (SLM) on an EOS M400-4. The inlet to throat diameter ratio D/d_{throat} of 1.5 is based on an optimum found by Marchan [28]. The tip diameter of 0.8 mm is chosen based on an estimate of the minimum diameter that could be reliably SLM printed to a reasonable degree of accuracy and repeatability ¹. The length

¹Based on conversations with an EOS printer operator in December 2023

of the resonance cavity is set 20 mm giving an L/d_{throat} of 10. This is similar to a resonator design by Lungu et al. [12] and deemed sufficiently long for the cavity to be able to initiate JRM [21]. This results in a 3.15° taper of the resonator, closely matching that of a resonator tested by Phillips and Pavli [33]. The interface with the chamber is post-machined to ensure the required alignment tolerance. A front view of the inlet of the resonator is shown in [Figure 5.3a](#), taken using a digital microscope.

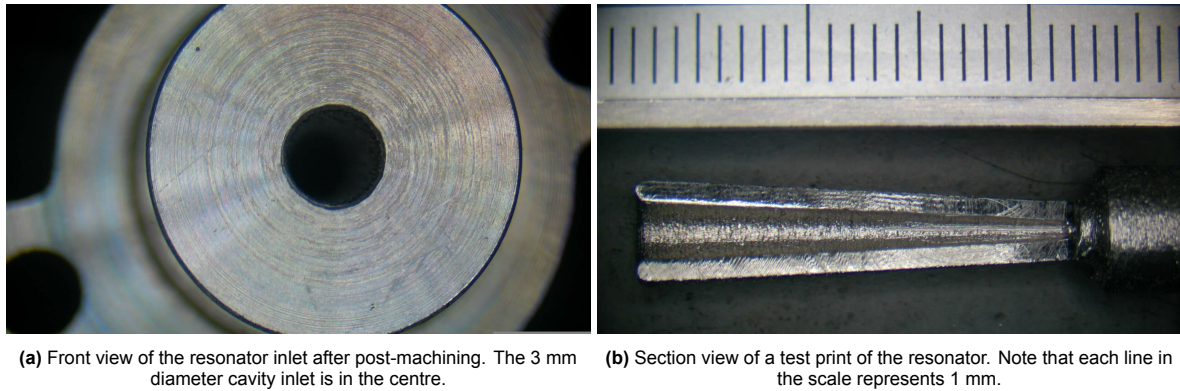


Figure 5.3: Microscope images of SLM printed resonance cavity.

A set of test prints was created with 1.2 mm and 0.8 mm tip diameters to ensure that the cavity dimensions were properly resolved by the SLM process. One of these test prints is shown in [Figure 5.3b](#). [Table 5.2](#) shows the design resonator dimensions compared to those measured off of the test print. The overall length of the cavity and the tip diameter match the design point very closely. The inlet of the print appears quite rounded which leads to a larger measurement error. However, the design value of the inlet diameter is still within the uncertainty of the measurement. The test print does not have a closed cavity tip (in contrast to the actual resonators), instead extending the 0.8 mm hole through the base of the part. This allowed for inspecting the circularity of cavity with a gauge pin, leading to an estimated diameter between 0.7 mm and 0.8 mm.

Table 5.2: Design and Measured Resonator Dimensions

Dimension	Design Value	Measured Value
Inlet diameter (mm)	3	2.83 ± 0.25
Tip diameter (mm)	0.8	0.8 ± 0.1
Resonator length (mm)	20	20 ± 0.18
D/d_{throat} (-)	1.5	1.41 ± 0.125
L/d_{throat} (-)	10	10 ± 0.09

It was not possible to inspect the surface roughness of the inside of the cavity. This is an important parameter for predicting the heat flux to the cavity wall [54] and presents a possible disturbance for the shock wave travelling into the cavity. To minimise surface roughness, all resonators were printed upright with the cavity tip closest to the build plate.

5.3.3. Modified Resonator Inlet Geometry

The shape of the cavity inlet affects the pressure field upstream of the resonance cavity. An additional resonator was modified to test the effect of the cavity inlet geometry on the onset of JRM. A 45° chamfer with a length of 4 mm is applied to the blunt cavity inlet. The dimensions of the resonance cavity remained unchanged. A comparison of the geometries of the two resonators is shown in [Figure 5.4](#).



Figure 5.4: Comparison between the conical (left) and cylindrical resonator (right).

5.3.4. Resonance Frequency

The expected resonance frequency of the acoustic cavity is a useful parameter for quantifying fluid time scales for simulations [48] or for selecting appropriate measuring equipment. The quarter wave frequency of a truncated cone can be estimated using Equation 5.4 [55].

$$\frac{2\pi f_{0,cone}}{a(T)} L = \pi - \arctan\left(\frac{2\pi f_{0,cone}}{a(T)} L \frac{D_1}{D_2 - D_1}\right) \quad (5.4)$$

Where L is the length of the resonator and $a(T)$ the speed of sound, as a function of gas temperature. D_1 is the diameter at the resonator tip and D_2 is the entrance diameter of the cavity. As the gas temperature inside the resonator varies considerably as a function of position and moment in the resonance cycle, it is expected to have an impact on the resonance frequency. Figure 5.5 shows the estimated natural frequency of the resonator as a function of gas temperature for both oxygen and nitrogen. Gas properties of oxygen and nitrogen are taken from CoolProp [36]. For the design resonator dimensions shown in Table 5.2 and assuming 20°C gas temperature, this results in $f_0 = 5065$ Hz for oxygen and $f_0 = 5417$ Hz for nitrogen.

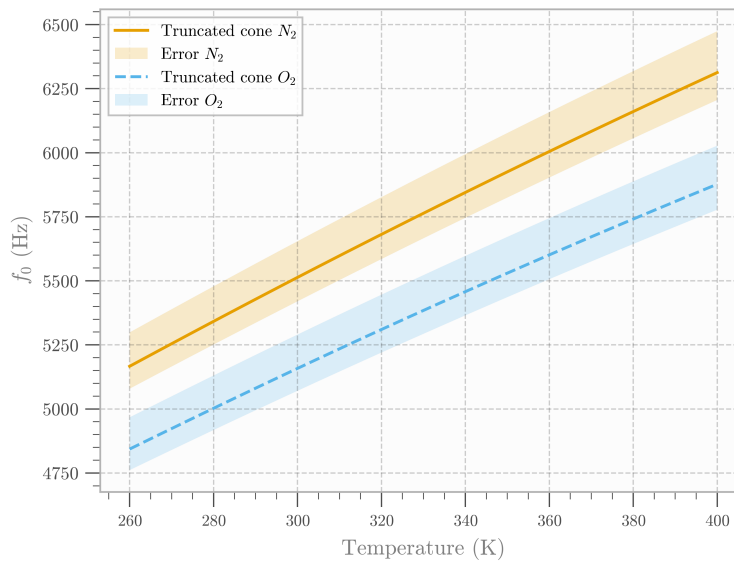


Figure 5.5: Temperature dependent quarter wave frequencies of a truncated cone for the given resonator dimensions using oxygen and nitrogen.

Based on the measurement error of the resonator dimensions, shown in [Table 5.2](#), an error was added to the expected quarter wave frequency. A maximum upper and lower bound of the error are determined by stacking the errors in [Table 5.2](#) and identifying the permutation that causes the largest deviation in a given direction. The lower bound of the error was determined to be -1.693%, with the upper bound being 2.558%. These bounds are effectively constant over the temperature range shown in [Figure 5.5](#) and between nitrogen and oxygen.

5.3.5. Chamber Natural Frequencies and Secondary Resonance

The supersonic under-expanded flow into the combustion chamber can excite acoustic modes outside of the resonance cavity. The volume between the under-expanded jet and the methane injector, shown in [Figure 5.2](#), can act as a Helmholtz resonator with a frequency that changes as a function of s/d_{throat} . Changing s/d_{throat} in turn changes the area of the *neck* of the Helmholtz resonator, while the cavity volume remains constant.

In some cases it is possible that this secondary resonance is dominant in measurements, instead of to the operating mode of the cavity, as shown in [subsection 5.6.2](#). The natural frequency of a Helmholtz resonator can be determined using [Equation 5.5](#) [56].

$$f_0 = \frac{a}{2\pi} \sqrt{\frac{A}{V_0 L_{eq}}} \quad (5.5)$$

Here, a is the speed of sound of the gas inside the chamber. A is the cross sectional area of the neck formed by the nozzle gap distance and L_{eq} the equivalent length of the neck of the Helmholtz resonator. V_0 is the static volume inside the Helmholtz cavity. Using nitrogen and $s/d_{throat} = 3.5$, [Equation 5.5](#) predicts a natural frequency of 7132.5 Hz, a mode that is observed during some experiments shown in [section 5.6](#).

5.3.6. Propellant Feed System

The Pressure and Instrumentation Diagram for the fluid system is shown in [Figure 5.6](#), showing operational pressures, gases, as well as sensors. Three solenoid valves are used to control the flow of oxygen, methane and nitrogen. Check valves are placed on both the fuel and oxidiser lines upstream of the igniter to prevent reverse flow. Gas cylinder supply pressure is regulated using manually set diaphragm regulators. These feature manual depressurisation valves in case the solenoid valves are no longer operable, due to a loss of connection to the control system or power loss. The nitrogen purge is only supplied through the fuel line as this prevents the purge gas from causing unintentional resonance heating.

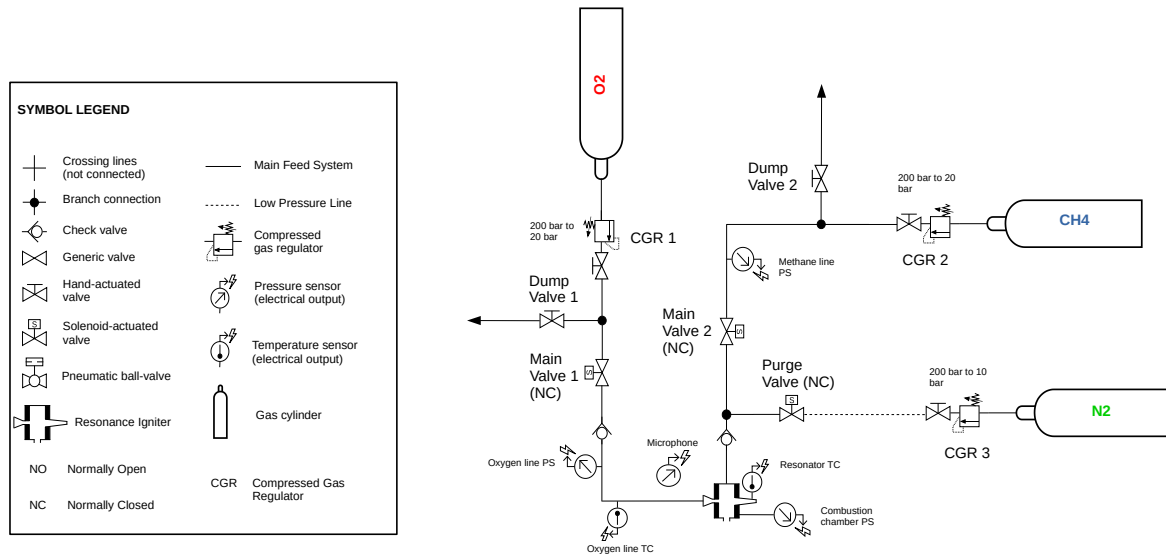


Figure 5.6: P&ID of the fluid system for combustion tests. Note that for heating tests the line to the methane cylinder is removed.

5.3.7. Sensors and Data Acquisition

An overview of the sensors used on the igniter test setup and their approximate placement is also given in Figure 5.6. Model designations of the various sensors and data acquisition modules are shown in Table 5.3. Two K-type thermocouples (TC) are spot welded to the tip of the resonator to sample the temperature of the outer wall at 50 Hz. The thermocouples are attached at $x/L = 0.8 \pm 0.1$ and $x/L = 1 \pm 0.1$ respectively. Pressure transducers (PT) are placed upstream of the oxygen and methane injectors and in the combustion chamber and sampled at 2 kHz. The chamber pressure transducer is separated from combustion gases using a stand-off pipe. In order to capture the expected resonance frequency of the acoustic cavity in both JRM and JSM, a microphone is placed outside of the combustion chamber near the tip of the resonator. Data is sampled at 100 kHz. This provides a non-invasive measurement of acoustic resonance. The small scale of the resonance cavity makes any direct pressure measurement at the tip of the resonance cavity very difficult.

Table 5.3: Elements of the Data Acquisition System

Application	Model	Specification	Error
Oxygen inlet PT	ifm PT5423 ²	0-60 bar	± 0.3 bar
Methane inlet PT	ifm PT5423	0-60 bar	± 0.3 bar
Chamber PT	ifm PT5423	0-60 bar	± 0.3 bar
ICP Microphone	PCB 106B52 ³	0-6.89 kPa, 13e-2 Pa resolution	$\pm 1\%$ FS
Resonator TC	RS PRO K-Type 0.3mm ⁴	-50°C – 600°C	$\pm 0.75\%$ FS

The microphone is used to determine frequency information during resonance heating. As such the amplitude error listed in Table 5.3 does not directly affect these results. The rise time is also not directly relevant, as data from a period of at least one second is used to generate the spectral data. The manufacturer lists the resonant frequency of the sensor itself as ≥ 40 kHz, which is an order of magnitude larger than the natural frequency of the resonance cavity.

²ifm PT5423 (last accessed 15.08.2024): <https://www.ifm.com/de/en/product/PT5423?tab=documents>

³PCB 106B52 (last accessed 15.08.2024): <https://www.pcb.com/products?m=106b52>

⁴RS PRO K-Type 0.3mm (last accessed 15.08.2024): <https://nl.rs-online.com/web/p/thermocouples/6212170>

5.4. Simulation Setup

The numerical model presented in this study uses the Open Source CFD software SU2 [52] to simulate thermo-acoustic heating. It demonstrates that a simplified 2D axis-symmetric model can predict the switch between operating modes and can be used as part of the igniter design process. A URANS simulation with $k-\omega$ SST turbulence model and non-ideal gas model are employed. Extensive validation of the simulation is performed using experimental data in [section 5.6](#) at varying nozzle gap spacing with both oxygen and nitrogen as driving gases. Additional validation using the alternative resonator inlet geometry (shown in [subsection 5.3.3](#)), as well as validation to an analytical shock-tube model are presented in [Appendix B](#).

5.4.1. Simulation Domain and Boundary Conditions

An illustration of the computational domain is shown in [Figure 5.7a](#). It includes the converging section of the oxygen inlet, the gap between nozzle and resonator, the resonance cavity and an outlet. A structured mesh is used throughout the domain, including boundary layer refinement. The domain is comprised of 96000 mesh elements, with 45000 elements forming the resonance cavity. An average $y^+ < 1$ is achieved along the resonator wall. Approximately 4 - 5 mesh elements are placed within $y^+ = 5$, to ensure appropriate near-wall resolution. Additional information on mesh quality is shown in [Appendix D](#). [Figure 5.7b](#) shows a part of the mesh at the inlet of the resonance cavity. Note that a rounded corner was artificially applied to the resonator inlet as well as the nozzle outlet. A corner radius of $r = 0.03 \cdot d_{throat}$ was found to significantly improve numerical stability, by avoiding high aspect ratio orthogonal cells in the boundary layer. The smoother transition between resonator inlet and outlet wall improved convergence during the outflow phase of the Jet Regurgitant Mode.

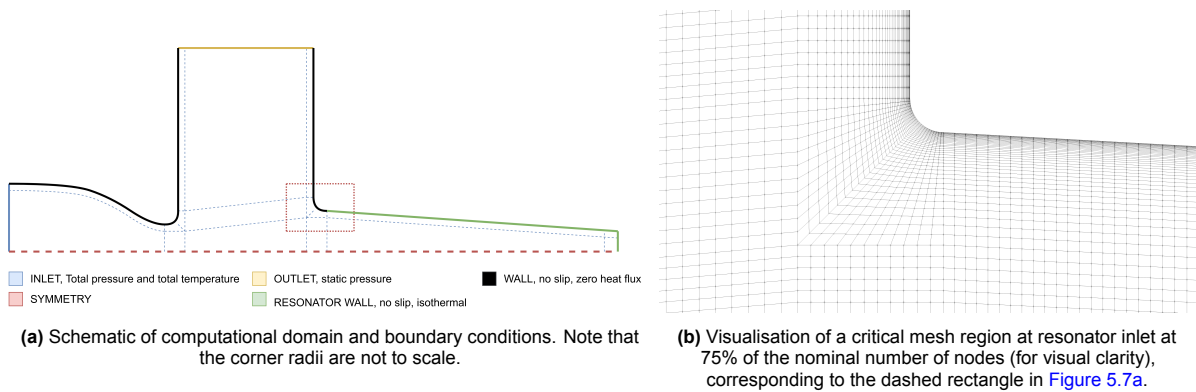


Figure 5.7: Critical mesh regions and boundary conditions.

The simulation domain is symmetric around the x-axis. The inlet boundary conditions are set as total pressure and temperature of the driving gas (either nitrogen or oxygen). This allows for matching the simulated inlet conditions to experimental measurements. Static pressure is prescribed at the outlet. The length of the outlet is set to five times the throat diameter to ensure sufficient distance from the under-expanded jet. The boundary of the resonance cavity is assumed to behave as an isothermal, no-slip wall. All other walls in the domain are also no-slip, but adiabatic.

The use of an isothermal wall significantly improved the stability of the simulation. The assumption introduces two sources of error when compared to the experiments. Fixing the wall at ambient temperature will result in a higher predicted heat flux at the tip of the resonance cavity, as the wall itself cannot heat up locally. A higher outward heat flux also means that the gas temperature inside the resonator will be lower in the simulation. This will impact the predicted resonance frequency slightly as the local fluid temperature influences the speed of sound. This error scales with the square root of the temperature and is expected to be minor, as the area in which the gas reaches these temperatures is very small compared to the total cavity length [27].

5.4.2. Time Scales

The two primary physical phenomena of interest in thermo-acoustic heating are the flow inside the resonator and the heat transfer through the resonator wall. The flow time scale and the conductive time scale are given by [Equation 5.6](#).

$$\tau_{flow} = \frac{1}{f_0} \quad , \quad \tau_{cond} = \frac{L^2}{\alpha} \quad (5.6)$$

Here, f_0 is the natural frequency of the resonance cavity. L is a length scale, in this case the wall thickness of the resonator and α is the thermal diffusivity of the material. Experimental results show a cavity natural frequency around 4800 Hz for oxygen (as shown in [Figure 5.16](#)). The corresponding flow time scale is $\tau_{flow} = 2.08 \cdot 10^{-4}$ seconds. The resonator wall is 1 mm thick and made from 17-4 PH stainless steel, with a thermal diffusivity of $5 \cdot 10^{-6}$ m²/s, resulting in a conductive time scale of $\tau_{cond} = 0.2$ seconds.

The simulation used for showing the onset of JRM cover $2 \cdot 10^{-3}$ seconds of actual flow time. As such the assumption of a constant wall temperature is justified by the simulation time being two orders of magnitude shorter than the conductive time scale of the resonator wall.

Other authors have assumed an infinitely thin resonator wall with a fixed heat transfer coefficient [48] [49] [50]. This is useful for determining a more accurate estimate of the wall temperature along the resonator. However, it produces wall temperature fluctuations at the same time scale as the gas flow inside the resonator. During the outflow phase of JRM the gas inside the cavity can become colder than the cavity wall [27], leading to a transfer of heat from the wall back to the gas. A thin wall with an instantaneous response results in a slower re-admission of heat to the outflow compared to a wall with a high degree of thermal inertia. This in turn impacts the temperature inside the resonance cavity at the start of the next inflow cycle.

5.4.3. Solver Setup

The difficulty in simulating thermo-acoustic heating lies in simulating a flow that alternates between subsonic and supersonic, as shock waves enter and are reflected in the resonance cavity. As a result gradients in velocity, pressure and temperature are very high throughout the flow field. The flow inside the cavity periodically experiences reverse flow inside the boundary layer. This occurs as the reflected shock wave collides with the mean flow inside the resonator, still moving in the direction of the cavity tip. The numerical instability associated with this flow is overcome using the numerical dissipation, inherent to first order spatial discretisation.

SU2 solves the unsteady RANS equations through a finite volume discretisation. The presence of shock waves necessitates special treatment of the convective terms in the RANS equations. A density based solver with a classical Roe scheme [57] is employed for determining convective fluxes. A first order upwind scheme offers excellent numerical stability over all possible operating regimes at the expense of introducing a significant degree of numerical diffusion. Second order MUSCL reconstruction was experimented with but lead to instabilities that prevent a third of the iterations from converging. The use of a slope limiter based on methods by Venkatakrishnan and Wang [58] did not provide sufficient improvement.

Several AUSM type schemes, as well as the second order JST scheme were tested, but did not improve convergence. As such first order Roe was used for all further analyses. Lebedev and Bocharova validate a first order Godunov scheme against experimental results of supersonic jets on a flat plate and find their simulation to closely match Schlieren imaging [38]. A similar number of grid points are used in this study to discretise the area near the under-expanded jet. As such, the choice of a first order upwind scheme for this analysis appears justifiable. However, a higher order scheme would be preferred. Accurate resolution of the incident and reflected shock wave has an impact on the maximum pressure and temperature attained at the cavity tip. A further validation case is performed in [Appendix B](#), using an analytical model of flow inside shock tubes. This shows favourable behaviour of the first order upwind scheme, concerning the flow inside the resonator.

Gradient reconstruction from the cell centre is accomplished using the Green-Gauss node based method.

The effect of turbulence is modelled using the 2003 iteration of the $k-\omega$ SST turbulence model [59]. This model performs well under adverse pressure gradients [60], a condition encountered both near the resonance cavity inlet and along the cavity wall. It is also less sensitive to the prescribed inflow turbulence intensity, unlike the $k-\omega$ model [60].

For time integration, the Courant-Friedrichs-Lewy (CFL) condition poses a limit on the largest time step possible for a given time integration scheme to remain stable. For high flow velocities and fine grid sizes the CLF condition forces a very small time step on explicit time integration schemes [47]. This necessitates very high iteration numbers and high computational cost. The time step can be increased significantly (thereby reducing the total number of steps required) using a second-order-accurate dual time stepping method with implicit time integration. Here a quasi steady state problem is solved between each time steps. This leads to a higher computational cost per time step but allows for significantly larger time steps [48]. Using this technique a time step of $4 \cdot 10^{-8}$ s proved sufficient for numerical stability and adequate shock resolution.

5.4.4. Gas Model

The Peng-Robinson-Stryjek-Vera equation of state (EOS) implemented in SU2 [61] is used for the coupling between density and pressure, as well as determining the specific heat capacity of the driving gas. Other authors instead use an ideal EOS [48] [50] [49]. Figure 5.8 shows the density and C_p predicted by the ideal EOS and by a Peng-Robinson EOS over a temperature range expected inside the resonance cavity.

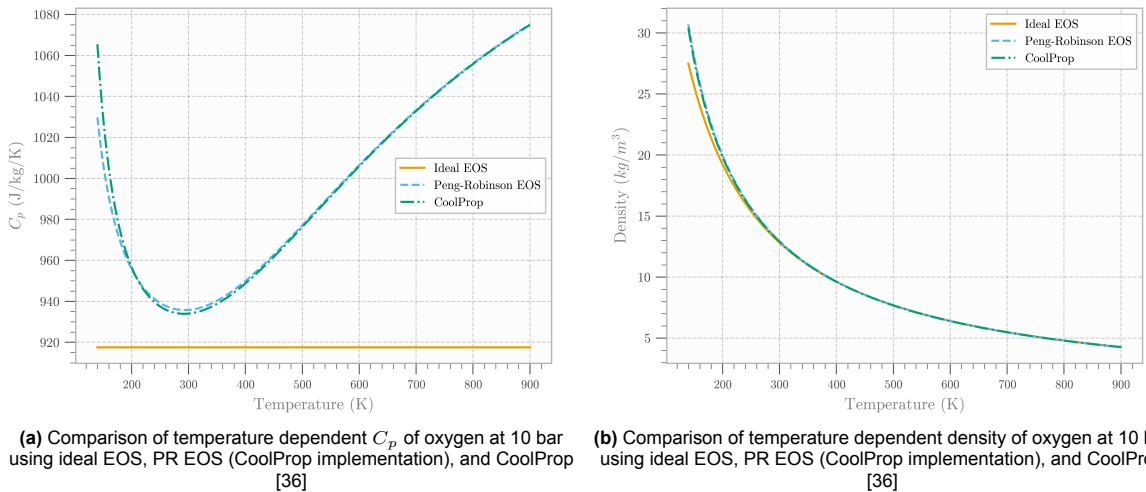


Figure 5.8: Non-ideal gas effects for conditions in the resonator cavity.

Figure 5.8a shows a deviation in the C_p of oxygen of up to 17.3% compared to an ideal gas at the highest gas temperature simulated inside the resonator tip. This is relevant both for heat transfer to the cavity wall, as well as the temperature rise experienced over the incident and reflected shock waves [17]. The flow also experiences temperatures below 170 K during the outflow phase and below 100 K inside the under-expanded free jet. Iwamoto identifies the pressure field upstream of the resonator during the outflow phase as important for initiating the next inflow cycle [26]. The pressure field determines both the uniformity and energy of the subsequent inflow. An accurate coupling of pressure and density at low gas temperatures is therefore important. The driving gas of a resonance igniter would likely consist of evaporated cryogenic propellants (liquid oxygen or liquid hydrogen) if used as part of a rocket propulsion system [33]. In this case the evaporated gas can enter the nozzle throat at a very low temperature, reducing further inside the under-expanded jet. Therefore when simulating the resonance heating under operating conditions, the pressure-density coupling upstream of the resonance cavity becomes even more critical than in the simulations presented as part of this study (conducted with the oxygen and nitrogen at room temperature). Table 5.4 shows the fluid parameters used in the resonance heating

simulations.

Table 5.4: Peng-Robinson EOS Critical Parameters and Acentric Factors from [62]

Fluid	p_c (MPa)	T_c (K)	ω (-)
Nitrogen	3.398	126.2	0.037
Oxygen	5.043	154.58	0.025

The temperature dependent viscosity of the gas is modelled using Sutherland's law. A constant turbulent and laminar Prandtl number are assumed. Together with the temperature dependent viscosity, this leads to a temperature dependent value for thermal conductivity.

5.4.5. Mesh Refinement Study

The numerical discretisation of the domain leaves a dependence of the solution on the grid resolution. This is especially relevant as shock waves are infinitely thin discontinuities in pressure, temperature and velocity [17]. The local mesh resolution, as well as the order of the numerical schemes used to approximate convective fluxes will influence how well this discontinuity over a shock wave is approximated.

In order to verify that the mesh used for these simulations is suitably fine, a Grid Convergence Index (GCI) together with a Richardson extrapolation are employed [63]. The GCI describes the error in a local flow variable at a given mesh refinement compared to an extrapolation, representing an infinitely fine mesh.

The grid is refined using a global mesh refinement parameter, which also inversely scales the mesh stretch factor. The number of elements in the gap between nozzle and resonator are also scaled with increasing s/d_{throat} . The flow inside the resonator behaves similar to one dimensional advection as the mean flow direction is predominantly along the x-axis. The mesh refinement study is therefore conducted with a constant Courant number, according to Equation 5.7. This means that for an increased spatial resolution, the time step is reduced proportionally.

$$C = \frac{u\Delta t}{\Delta x} \quad (5.7)$$

Where u is the magnitude of the velocity, Δt the time step and Δx the mesh spacing. A study of the grid convergence index (GCI) and Richardson extrapolation are performed for a normalised grid spacing of 0.64, 1, 1.56, corresponding to 40%, 100% and 240% of the number of nodes. As this is an unsteady simulation, the parameters used for this analysis are time averaged properties taken at discrete points along the centreline of the resonance cavity and the cavity wall. At each mesh refinement the simulation is run for three full JRM flow cycles. Figure 5.9 shows the mesh refinement study performed for fluid density and heat flux at three points along the length of the resonance cavity. The error bars represent the GCI at that refinement factor with an additional 25% margin applied to the error [63]. The points at a normalised grid spacing of 0 are the extrapolated solutions to a theoretical, infinitely fine mesh.

Figure 5.9a shows a very consistent GCI error of between 6.4% and 6.5% at the three locations along the resonator centreline. All points also show a clear convergence towards the extrapolated value. The estimated p-factor in Figure 5.9a varies between 1.3 and 2.1. This value represents the order of convergence of the method and is expected to be ≤ 1 for a first order convective scheme. The high p-factor is a result of maintaining a constant CFL number and the use of a second order method in time. As such the p-factor does not directly represent the order of convergence of the spatial discretisation, but a combination of the spatial and time discretisations.

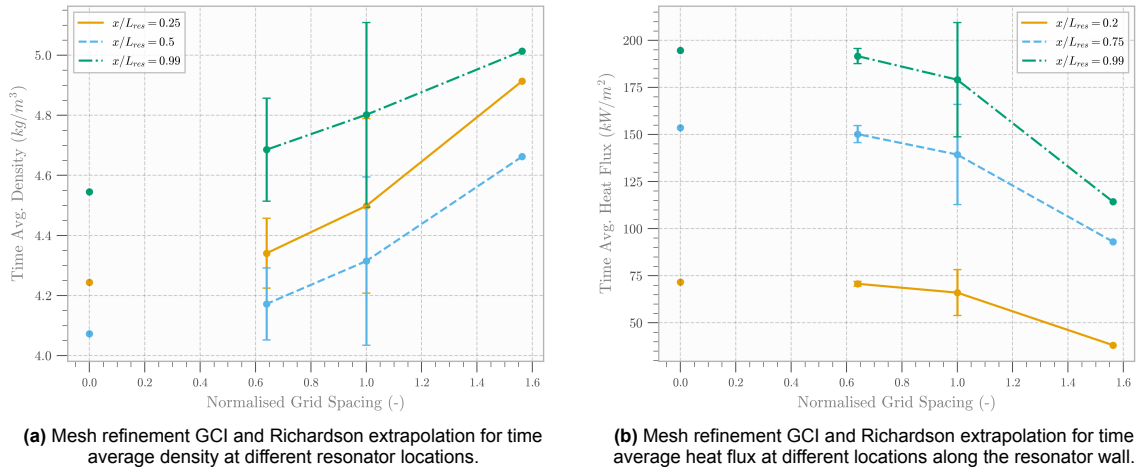


Figure 5.9: Mesh verification

Figure 5.9b shows a mesh refinement study performed at three points along the resonator wall for local heat flux. Here the GCI error bar is still rather large at the nominal mesh spacing. Despite $y^+ < 1$ along the resonator at this mesh spacing, the estimate of wall heat flux still varies by almost 15 kW/m² between it and the finest mesh. This represents a GCI error of 16.9%. For the purposes of this study, the error shown in Figure 5.9b is deemed acceptable, as the relative heat flux generated at different s/d_{throat} is the desired outcome, rather than absolute estimates of heat flux. For a numerical study interested in the absolute heat flux or wall temperature, a finer mesh, closer to 200% of the nominal number of nodes is recommended.

5.4.6. Simulation Cases

In order to show that this simulation is capable of predicting the switch between JSM and JRM, parametric sweeps are used with either oxygen and nitrogen as the driving gas. In the case of nitrogen, $1.5 \leq s/d_{throat} \leq 4$ and $2.5 \leq s/d_{throat} \leq 4$ in the case of oxygen. The inflow total conditions and outflow static pressure are set according to those measured during the corresponding experiment.

For the parametric sweeps, simulations are run for $5 \cdot 10^4$ time steps (corresponding to 2 ms of actual flow time). A startup transient of two flow cycles (corresponding to $1 \cdot 10^4$ time steps) is excluded from the analysis. The specific gap spacings of $s/d_{throat} = 2.0, 2.05$ and 3.0 with nitrogen and $s/d_{throat} = 3.0$ for oxygen were simulated for $2 \cdot 10^5$ time steps for a more accurate comparison between simulated and experimental pressure spectra. The results of these simulations and validation with experimental data are presented in section 5.6.

5.5. Experimental Method

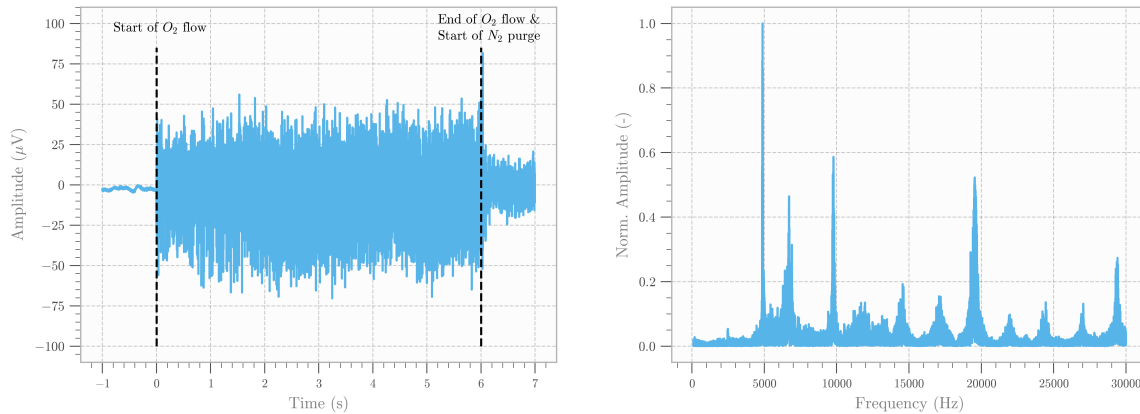
The test setup described in section 5.3 was used for a total of 95 resonance heating tests with either nitrogen or oxygen. A further six ignition tests were conducted with the setup. Over the course of the heating tests the nozzle gap spacing, driving gas, upstream pressure and resonator inlet geometry were varied to explore a wide performance envelope for thermo-acoustic heating.

5.5.1. Resonance Heating Experiments

The objective of the resonance heating experiments was to explore the effect of nozzle gap spacing and upstream total pressure on the operating mode of the resonator, as well as their impact on the rate of resonance heating. These experiments also serve as model validation for the numerical simulations outlined in section 5.4. The test setup allows for varying the nozzle gap spacing from 1.5 to 4, the full range of which was tested using nitrogen. A more limited parametric sweep was conducted with oxygen, between $s/d_{throat} = 2.5$ and $s/d_{throat} = 3.5$, due to a limited availability of gas. Each set point was tested between three and eight times to confirm the consistency of the microphone spectra and

tip temperature. Before the start of each new test the resonator is allowed to cool down to ambient temperature to maintain similar starting conditions for each test. Some variation in initial temperature remains as a result of changing ambient temperature during the test day ($< 5^{\circ}\text{C}$).

Six seconds of resonance heating, followed by two seconds of a nitrogen purge were used for all heating tests. This allowed for a significant temperature rise at certain settings, but not for tip temperature to reach steady state. This was typically only reached after 18 seconds (as tested with nitrogen at select s/d_{throat}). For the spectral analysis the time interval between T+1 and T+5 seconds was sampled. This resulted in a total of $4 \cdot 10^5$ samples used for the fast fourier transform of the pressure signal. [Figure 5.10a](#) shows the raw microphone data



(a) Microphone pressure trace of heating test with O_2 at $s/d_{throat} = 3$, NPR = 6.4.

(b) FFT of pressure trace in [Figure 5.10a](#).

Figure 5.10: Processing of microphone data for heating test results.

The temperature measured at the resonator tip is corrected for the response time of the thermocouple, as shown in [Appendix C](#) [64]. The correction is particularly relevant for the rapid initial temperature rise, as the thermocouple is estimated to have a response time of $\tau = 0.1$ seconds. Tip temperature measured during a set of 15 second resonance heating tests is shown in [Figure 5.11a](#). An insulating cover was placed over the resonator tip to limit convective heat loss to the environment and increase maximum tip temperature during ignition tests. This removes additional heat loss from forced convection. [Figure 5.11a](#) shows an increase of maximum tip temperature of around 40 K when using the aluminium cover, as well as significant smoothing of the temperature profile.

5.5.2. Combustion Experiments

A total of six ignition attempts were made. The igniter is designed to operate at an equivalence ratio of $\phi = 1$. By varying the CGR set point of the methane and oxygen cylinder independently the equivalence ratio can be adjusted. Equivalence ratios between $0.9 < \phi < 1.3$ were tested. Upstream pressure was varied between 14, 19 and 23 bar on the oxygen and methane supply. [Figure 5.11b](#) shows typical system pressures during an ignition test. The pressure is displayed as a line indicating a moving average, with the surrounding shaded area representing two standard deviations above and below the average. Note that the pressure in the methane line is measured upstream of main valve 2 (as seen in [Figure 5.6](#)). The pressure in the oxygen line is measured downstream of main valve 1. Once the methane is injected, the chamber pressure increases as a result of an increasing mass flow through an already choked exhaust nozzle. Oxygen inflow begins at T+0 seconds and lasts until T+16 seconds. Methane is injected into the combustion chamber from T+14 seconds until T+16 seconds. This is followed by a two second nitrogen purge, not shown in [Figure 5.11b](#).

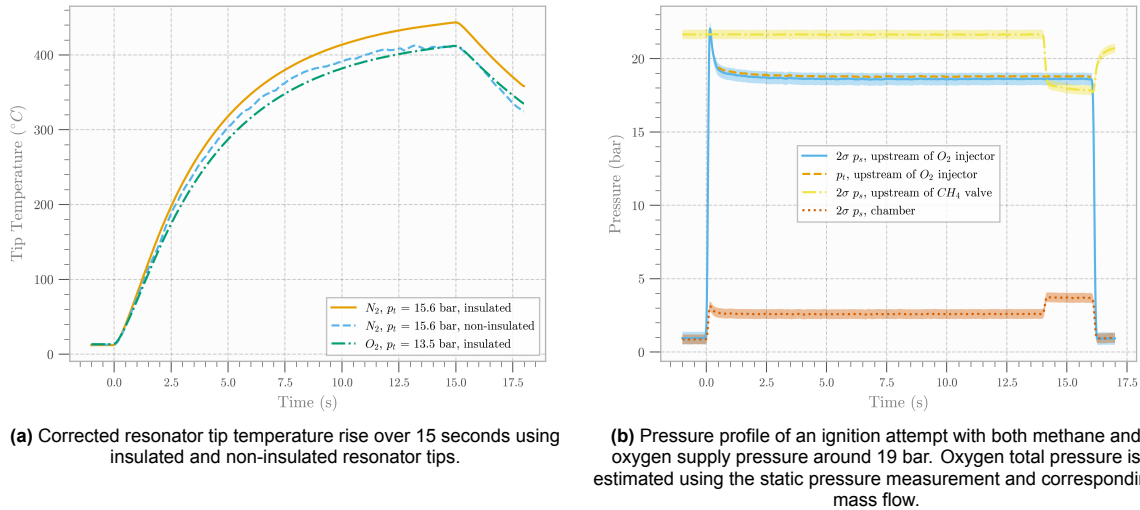


Figure 5.11: Processing of pressure and temperature data for ignition attempts.

Figure 5.11b also shows an estimate for the total pressure of the oxygen supply. The pressure sensor mounted on the oxygen line measures static pressure that must be corrected to total pressure to determine the NPR. The mass flow of oxygen can be estimated using Equation 5.2. The Mach number at the pressure port was determined using this mass flow and the diameter of the oxygen line at the pressure port. Assuming isentropic flow, the total pressure could then be estimated from the local Mach number. The error in the mass flow estimate is due on the noise of the pressure measurements (before filtering), as well as the machining tolerance of the nozzle throat diameter. This error becomes relevant when analysing the equivalence ratio found inside the combustion chamber during methane injection.

5.6. Resonance Heating Results

Experimental results are presented for thermo-acoustic heating at variety of s/d_{throat} and upstream pressure for both oxygen and nitrogen. Corresponding simulations at the same s/d_{throat} are used to validate the numerical model. The simulations are shown to predict the onset of JRM, as well as the point of highest resonance heating accurately for nitrogen. The simulation results are used to analyse the different flow patterns at specific s/d_{throat} , as well as their impact on heat flux to the cavity wall. Additional experimental spectra are presented for a conical resonator inlet geometry to show its effect on the onset of JRM.

5.6.1. Description of Operating Modes

The parametric sweep over s/d_{throat} allows for a detailed analysis of JRM and JSM as observed in both simulation and experimental data. Images from a complete flow cycle of JRM are shown in Figure 5.12, simulated at $s/d_{throat} = 3.25$ and NPR = 6.8 using nitrogen. The flow patterns shown closely match descriptions by Sarohia and Back [21] and Sobieraj and Szumowski [24], obtained using Schlieren imaging.

The Jet Regurgitant Mode can be broken down into four stages that occur cyclically. The time for a single cycle closely aligns with the quarter wave frequency of the resonance cavity [21] [25]. During the *inflow phase*, image (1), pressure inside the resonance cavity is low, allowing for the under-expanded jet to push gas into the cavity, in the form of a series of pressure waves. If the L/d_{throat} is sufficiently large, these pressure waves can coalesce into a single shock wave [21]. This shock wave is reflected at the tip of the cavity and travels back towards the nozzle. Both the incident and reflected shock wave are primarily responsible for the increase in temperature and pressure at the tip of the cavity. Friction between the entrained gas and the cavity wall further increases the total temperature of the fluid. After leaving the cavity the shock wave induces a series of expansion waves that travel towards the tip of the cavity. The *transitional phases*, images (2) and (3), mark a low pressure region in the

wake of this expansion wave and results in fluid leaving the cavity. The flow leaving the cavity pushes the Mach disk of the under-expanded jet rearward. Eventually, the interface between the outflow from the cavity and the under-expanded jet comes to a standstill. The *outflow phase* is complete when this reflected expansion wave has left the cavity, shown in image (4). As the low pressure behind the reflected expansion wave reaches the cavity inlet it suddenly weakens the interface between the under-expanded jet and the outflow from the cavity. The Mach disk is again able to move towards the cavity inlet allowing the next inflow cycle to begin.

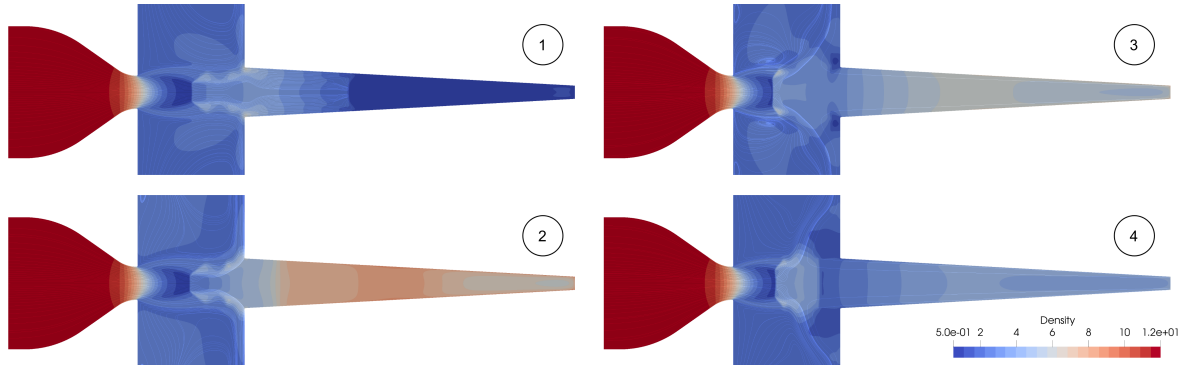


Figure 5.12: Simulated flow cycle in JRM, showing density and velocity stream lines, taken at $s/d_{throat} = 3.25$ and $NPR = 6.8$. (1) shows the beginning of the inflow phase with a shock wave moving into the resonance cavity. (2) and (3) show the transitional phases, as first the reflected shock wave leaves, followed by the mach disk reaching its closest point to the nozzle. (4) shows the end of the outflow phase, just before the start of the next flow cycle.

The Jet Screech Mode typically occurs when the cavity is placed at s/d_{throat} smaller than the length of the first shock structure of the under-expanded jet [21]. Schlieren images show a strong bow shock forming in front of the entrance to the cavity, completely encompassing it. The bow shock in front of the tube entrance acts like a membrane weakly compressing and expanding the gas inside the resonance cavity [21] [24]. Visualisations of a complete flow cycle of JSM are shown in Figure 5.13, simulated at $s/d_{throat} = 2$ and $NPR = 6.8$ using nitrogen. With every back-and-forth-motion of this bow shock, weak pressure waves travel down the length of the cavity, shown in both image (1) and (2). Unlike in JRM, multiple compression waves enter before the first is reflected off of the end-wall of the cavity. Little to no fluid in the tube leaves during these oscillations as the pressure difference experienced by the gas inside the cavity is significantly lower than during JRM. Friction from each compression wave incrementally increases the temperature of the entrained gas and the cavity wall.

Figure 5.13 shows this minimal movement of the Mach disk during the various compressions and expansions. Images (1) and (2) represent the entire movement range of the mach disk. Multiple pressure waves entering the cavity simultaneously are also clearly visible.

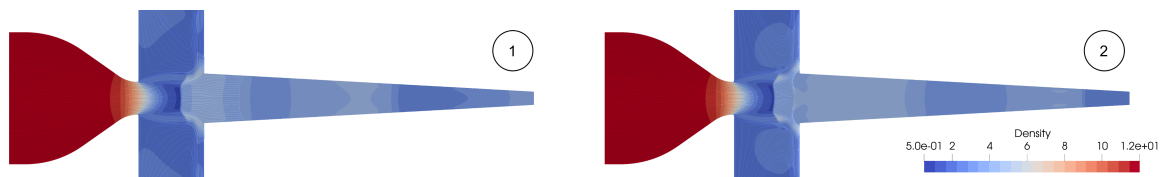


Figure 5.13: Simulated flow cycle in JSM, showing density and velocity stream lines, taken at $s/d_{throat} = 2$ and $NPR = 6.8$. (1) Shows a pressure wave entering, (2) shows this pressure wave reflected, while another is entering the cavity. The interval between (1) and (2) represents the full movement of the Mach disk.

5.6.2. Switch Between Operating Modes

The pressure trace recorded by the microphone provides clear spectra of the acoustic resonance inside the cavity. These are taken at every nozzle gap spacing and provide a very good indication of the operating mode of the cavity. Figure 5.14a and Figure 5.14b show spectra over varying s/d_{throat} for nitrogen and oxygen, respectively. It is worth noting that the NPR is slightly different between both sets

of tests. The manually adjusted gas regulators used for the experiments introduces some variation in upstream pressure between the two different gases. In this case the parametric sweep with nitrogen was conducted at NPR = 6.8, while for oxygen NPR = 6.4. All spectra are normalised to the maximum amplitude at that particular nozzle gap spacing.

Figure 5.14a shows a clear onset of a Jet Regurgitant Mode at $s/d_{throat} = 2$. At $s/d_{throat} = 2$ the natural frequency of the resonance cavity (expected between 5000 and 6000 Hz, based on the cavity shape) begins to appear, in addition to its overtones. The fundamental frequency of the cavity has the highest amplitude in this spectrum. This is accompanied by a noticeable increase in resonator tip temperature, as discussed in subsection 5.6.4. Up to and including $s/d_{throat} = 4$ the resonator operates in JRM. In the spectrum at $s/d_{throat} = 3$, the fundamental frequency and the first two overtones are most clearly visible. This point happens to align with the point of maximum tip temperature as discussed in subsection 5.6.4. At $s/d_{throat} = 1.5$ no clear resonance peaks are visible under 20 kHz and no significant heating is observed. At this particular gap spacing several peaks are visible near 40 kHz, indicating a Jet Screech Mode (not shown in Figure 5.14a).

A sudden shift in f_0 , from 5500 Hz to 7000 Hz, is observable at $s/d_{throat} = 3.5$ in Figure 5.14a. f_0 returns to the previous value at $s/d_{throat} = 4$. This appears to be the result of a secondary resonance mode excited at that particular gap spacing. The volume between the main flow axis through the nozzle and the methane inlet creates a cavity similar to a Helmholtz resonator, as discussed in subsection 5.3.5. To confirm this, the resonator was attached to an alternate mount with four exhaust holes arranged around the flow axis of the resonating gas. With this mount f_0 remains around 5500 Hz at $s/d_{throat} = 3.5$. This indicates that the resonance frequency of the cavity does not change at this nozzle gap spacing. While mounted inside the combustion chamber, $s/d_{throat} = 3.5$ appears to excite a secondary mode outside of the resonance cavity that has a higher amplitude than f_0 of the cavity when detected by the microphone. The same shift in f_0 is observable in Figure 5.14b but at $s/d_{throat} = 3.25$. The lower of speed of sound of oxygen could cause the onset of the same secondary resonance at a slightly lower gap spacing than for nitrogen.

Figure 5.14b shows that between $s/d_{throat} = 2.5$ and $s/d_{throat} = 3.5$ the cavity is operating in JRM when using oxygen.

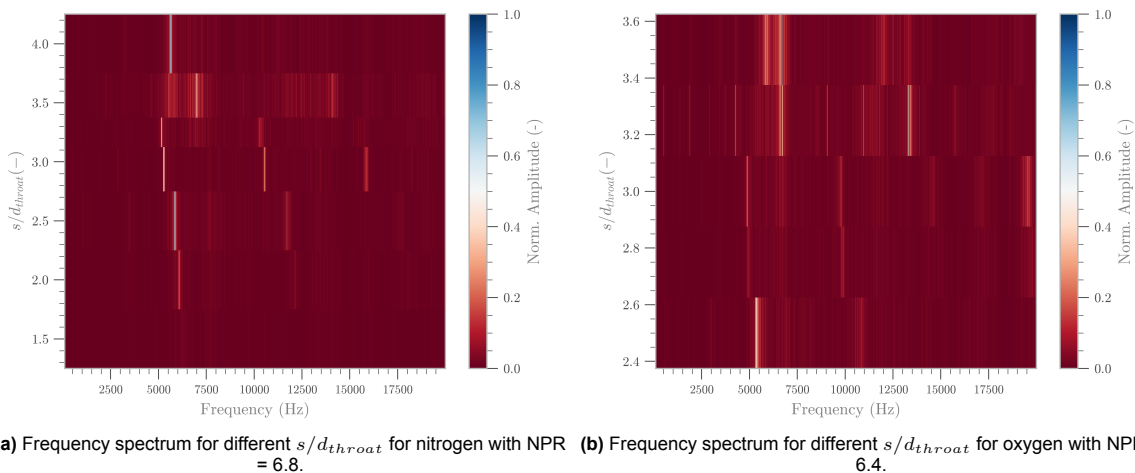


Figure 5.14: Spectra of parametric sweeps with oxygen and nitrogen.

The results shown in Figure 5.14 differ notably from results obtained by Lungu et al. [12]. Lungu et al. observe a clear onset of JRM only at $s/d_{throat} = 3.5$ when using oxygen, at an NPR of 6.31. Closer agreement is found with results from Sarohia and Back, who predict an onset of JRM near $s/d_{throat} = 2.5$ for NPR = 6.8 when using nitrogen [21]. Several important differences exist between the resonance cavities used for these experiments and those tested by the other authors. While their cavity shape and size are quite comparable, Lungu et al. use a sharp edged inlet to the resonance cavity, as opposed to

blunt inlet used in these experiments. The effect of the inlet shape is further explored in [subsection 5.6.6](#). Sarohia and Back use a conical resonance cavity with a significantly lower L/d_{throat} to characterise this specific combination of s/d_{throat} and NPR.

Sarohia and Back predict the onset of JRM when the inlet of the resonance cavity is placed beyond the end of the first shock structure of the under-expanded jet [21]. This holds for $NPR < 6$, after which the onset point JRM moves to a larger nozzle gap spacing, until at $NPR = 8$ it occurs at the end of the second shock structure. Using [Equation 5.1](#) the first shock structure ends at $X_c/d_{throat} = 2.074$ for $NPR = 6.8$. The results in [Figure 5.14a](#) show that, in these experiments, JRM still occurs at the first shock structure even at the higher pressure ratio.

5.6.3. Experimental Validation of Numerical Model

The validation of the CFD simulations outlined in [section 5.4](#) is performed quantitatively through a comparison of f_0 at select nozzle gap spacings, shown in [Figure 5.15](#) and [Figure 5.16](#). Of particular interest is the point of onset of JRM, as well as the points of maximum tip temperature, as seen in [subsection 5.6.4](#).

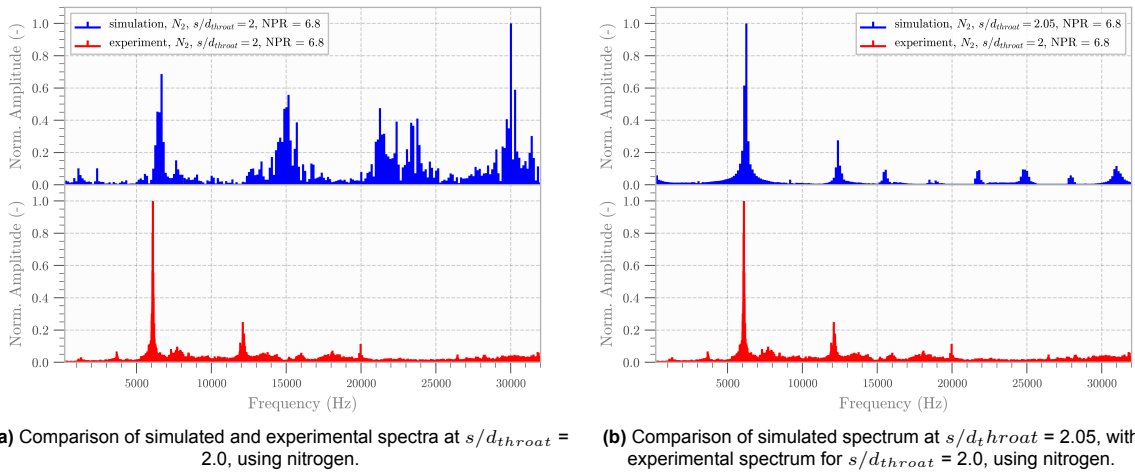
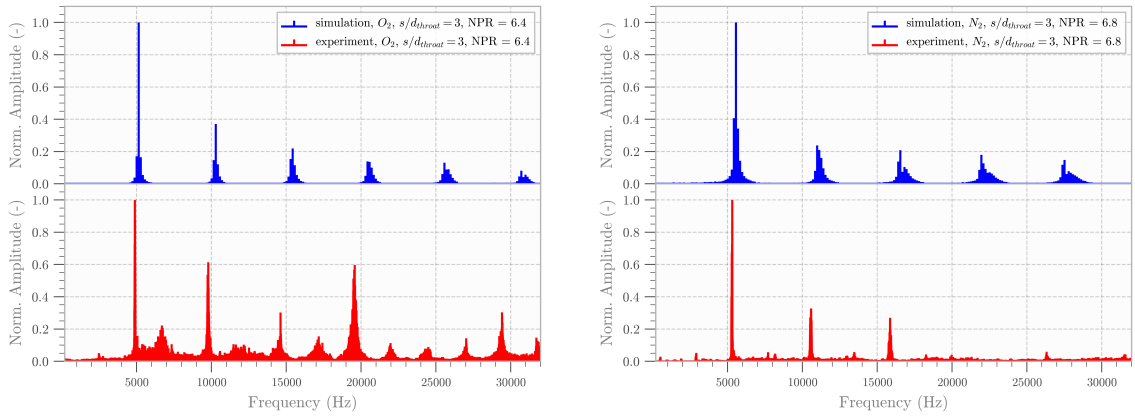


Figure 5.15: Model validation at $s/d_{throat} = 2.0$.

The similarity between the simulated and experimental spectrum at $s/d_{throat} = 2.0$ is rather poor. At this nozzle gap spacing CFD predicts no clear resonance at the natural frequency of the cavity. Meanwhile the onset of JRM is clearly visible in the experimental data. A simulation run at $s/d_{throat} = 2.05$, however, shows excellent agreement with the experimental data for $s/d_{throat} = 2.0$ with an error in the fundamental frequency of 2.59 %.

The simulation predicts a clear onset of JRM at $s/d = 2.05$, while experiments show it occurring at, or just under $s/d_{throat} = 2.0$. [Figure 5.15b](#) shows f_0 and its first overtone predicted very closely by the simulation. The second overtone, visible in the experimental data is not clearly present in the simulation.

Comparing [Figure 5.15](#) and [Figure 5.16](#) the simulation accurately captures the gradual shift in fundamental frequency between $s/d_{throat} = 2$ and $s/d_{throat} = 3$ from 6252 Hz to 5558 Hz. The physical reason for this shift is currently unknown and requires further study. A small shift in frequency is expected as the cavity temperature increases. This directly effects the gas temperature in the cavity and thereby also the local speed of sound. This can be quantified by taking multiple spectra during a single heating test. It was found experimentally that an increase in wall temperature of 350 K causes an increase in f_0 of approximately 87 Hz. This means that the aforementioned shift in f_0 between $s/d_{throat} = 2$ and $s/d_{throat} = 3$ is likely caused by a different phenomenon.



(a) Comparison of simulated and experimental spectra at $s/d_{throat} = 3.0$, using oxygen. (b) Comparison of simulated and experimental spectra at $s/d_{throat} = 3.0$, using nitrogen.

Figure 5.16: Model validation at $s/d_{throat} = 3.0$, using different gases.

The simulated and experimental spectrum show very close agreement at $s/d_{throat} = 3$ using nitrogen. The experimentally obtained spectra clearly show the natural frequency of the resonance cavity and its first two overtones. In [Figure 5.16b](#) the fourth overtone is barely visible around 26200 Hz. The simulation meanwhile shows several more integer multiples of the first harmonic (with decreasing amplitude) beyond what is shown in experimental data. The experimental measurements are obtained using a microphone placed several centimetres away from the resonance cavity. It is possible that some of the higher order modes might be attenuated by sound travelling through the resonator wall.

For the same nozzle gap spacing tested with oxygen, the simulated spectrum differs more significantly from experimental results. The first harmonic of the cavity is over-predicted by 5.23%. The location of the first three overtones of this natural frequency are clearly visible in both graphs. The amplitudes of the first and third overtone are significantly larger in the experimental data compared to the simulation. Experimental data shows an additional peak around 6800 Hz, which is not present in the simulation. The overtones of this additional peak are also visible over the remaining frequency domain. It is possible that this peak is related to the secondary resonance observed at $s/d_{throat} = 3.5$ when using nitrogen, discussed in [subsection 5.6.2](#). A summary of the error in f_0 for all cases is shown in [Table 5.5](#)

Table 5.5: Error in Fundamental Frequency between Simulation and Experiment

s/d_{throat}	Experiment (-)	s/d_{throat}	Simulation (-)	Gas	f_0 error (%)
2.0 ± 0.028		2.0		N_2	9.43 ^{+1.69} -2.56
2.0 ± 0.028		2.03		N_2	6.57 ^{+1.69} -2.56
2.0 ± 0.028		2.05		N_2	2.59 ^{+1.69} -2.56
3.0 ± 0.028		3.0		N_2	4.62 ^{+1.69} -2.56
3.0 ± 0.028		3.0		O_2	5.23 ^{+1.69} -2.56

The nozzle gap spacing is manually adjusted between experiments using a screw thread with a pitch of 1 mm on the outside of the oxygen inlet. A rotational misalignment of up to 20° is possible while setting s/d_{throat} . This results in a gap space error of 0.056 mm and a corresponding error in s/d_{throat} of 0.028. [Table 5.5](#) additionally shows the error for one more simulation case at $s/d_{throat} = 2.03$ to show the convergence of the frequency error around the onset of JRM. A range is added to the f_0 error to account for the uncertainty in cavity dimensions as a result of manufacturing error. The values are based on the procedure described in [subsection 5.3.2](#).

5.6.4. Tip Temperature and Heat Flux

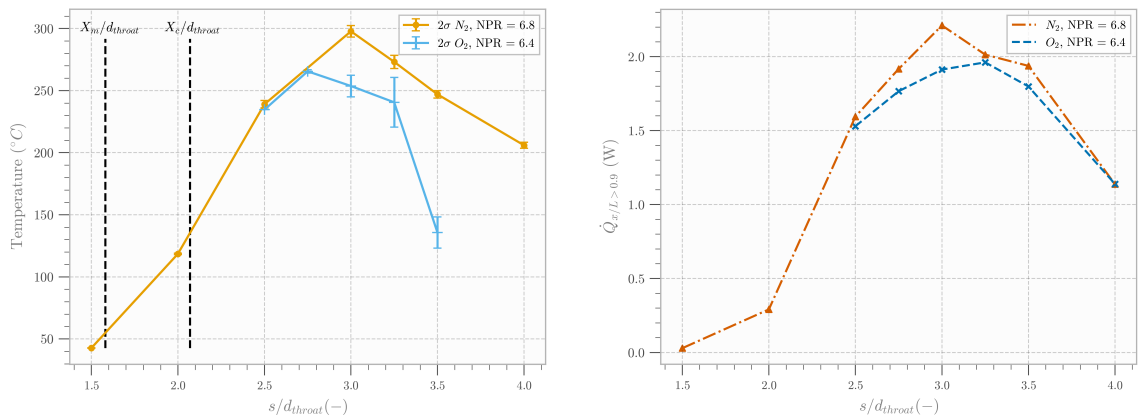
The maximum tip temperature as a function of nozzle gap spacing is shown in Figure 5.17a. The onset of JRM, previously identified at $s/d_{throat} = 2$ is also accompanied with a significant increase in tip temperature. A clear maximum temperature for nitrogen is found at $s/d_{throat} = 3$. For oxygen this maximum appears instead at $s/d_{throat} = 2.75$, and is significantly less pronounced compared to nitrogen. Higher nozzle gap spacings result in a rapid decrease in tip temperature, even if the igniter still operates in JRM (as shown in Figure 5.14b).

A qualitative comparison between the experimental parametric sweeps and the simulation can also be performed using Figure 5.17a. The simulation assumes a constant wall temperature, so the time averaged heating power through the resonance tip is used for comparison with experimentally determined tip temperature. Equation 5.8 is used to determine the time averaged heating power of the resonator tip for all nodes along the resonator wall where $x/L > 0.9$. According to Brocher and Maresca this represents the section of the resonator that is expected to have the highest wall temperature [27].

$$\dot{Q}_{x/L>0.9} = \int_{0.9}^{1.0} 2\pi D \bar{q} d(x/L) \quad (5.8)$$

Here \bar{q} represents the time averaged heat flux at a single node along the resonator wall and D the local diameter of the resonator inner wall. The time averaged heating power is calculated by numerically integrating Equation 5.8 over the relevant wall indices. Figure 5.17b shows the simulated heating power for both oxygen and nitrogen simulated at the same total temperature, total pressure and NPR as the parametric sweeps in Figure 5.17a. The shape of the simulated curve matches experimental heat flux very closely in the case of nitrogen. The location of maximum temperature and heat flux are identical. The onset of significant resonance heating at $s/d_{throat} = 2$ is also evident in both figures. Similarly, the steady decrease in heating after $s/d_{throat} = 3$ is captured by the simulation.

In the case of oxygen the comparison shows less agreement between the experiments and simulation. While the simulation accurately predicts a lower heat flux across every nozzle gap spacing compared to nitrogen, the point of maximum power is located at $s/d_{throat} = 3.25$, as opposed to $s/d_{throat} = 2.75$ in experiments. Furthermore, the time averaged heating power does not show the steep drop experienced at $s/d_{throat} = 3.5$ in Figure 5.17a, instead showing a very similar profile to the cases with nitrogen. The reasons for this discrepancy are difficult to ascertain and require further study.



(a) Experimental maximum tip temperatures for 6 seconds of resonance heating. Between three and nine tests were conducted per s/d_{throat} set point. X_m/d_{throat} and X_c/d_{throat} are determined using Equation 5.1 and shown for nitrogen at NPR = 6.8.

(b) Simulated time averaged heating power through the resonator tip wall under the same conditions as Figure 5.17a.

Figure 5.17: Qualitative model validation using wall temperature and heat flux.

A more direct comparison between the simulation and experimental results is shown in Figure 5.18. Here, the heating power and maximum tip temperature are both normalised to the maximum value

attained at $s/d_{throat} = 3$ with nitrogen. Between $s/d_{throat} = 2.5$ and $s/d_{throat} = 3.5$ the relative heating performance of the cavity is predicted very well by the simulation when using nitrogen. At lower nozzle gap distances the simulation predicts proportionally lower tip heating, specifically, when the resonator is operating in JSM. The relative heating performance of oxygen, compared to nitrogen, is also predicted accurately. The maximum heating power when using oxygen is 11.3% lower compared to the maximum value attained with nitrogen. The maximum temperature differs by 10.8%. Note that the experiments using oxygen were performed at $p_t = 8.87$ bar, with the experiments with nitrogen performed at $p_t = 10.2$ bar. In addition to the difference in gas properties, a lower total pressure reduces the expected heating performance in JRM, as discussed in [subsection 5.6.5](#).

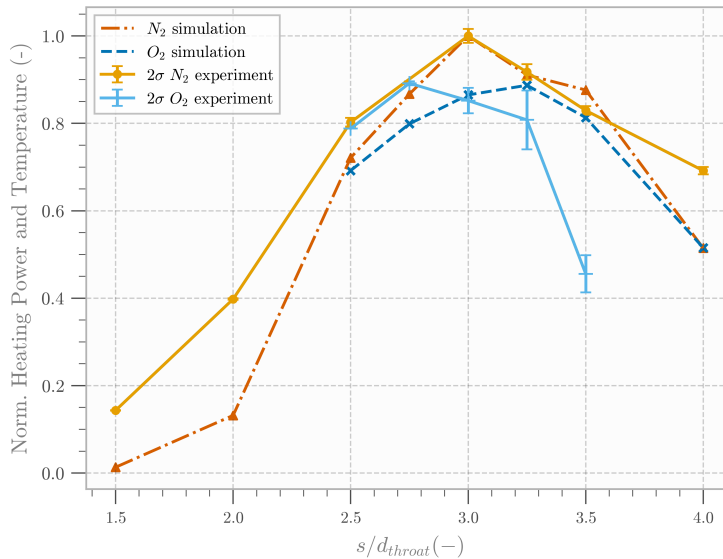


Figure 5.18: Normalised simulated heating power and experimentally determined maximum tip temperature.

In [Figure 5.18](#) $s/d_{throat} = 3$ stands out as a clear optimum for nitrogen at an NPR of 6.8 in both the simulation and experiments. [Figure 5.17b](#) predicts a 9.8% increase in heating power compared to $s/d_{throat} = 3.25$, with a corresponding 9% increase in measured tip temperature. Using the simulated flow field in the resonance cavity these two operating points can be investigated. Simulation results of these two points show that $s/d_{throat} = 3.25$ experiences both a higher end-wall pressure and higher end-wall gas temperature than $s/d_{throat} = 3$. [Figure 5.19a](#) shows the pressure at the cavity tip during a single flow cycle. [Figure 5.19b](#) shows the heat flux over the same flow cycle at a single point along the resonator wall, near the cavity tip. Here too the maximum heat flux is slightly lower in the case of $s/d_{throat} = 3$. Based on this the expectation would be that $s/d_{throat} = 3.25$ would cause the highest rates of resonance heating.

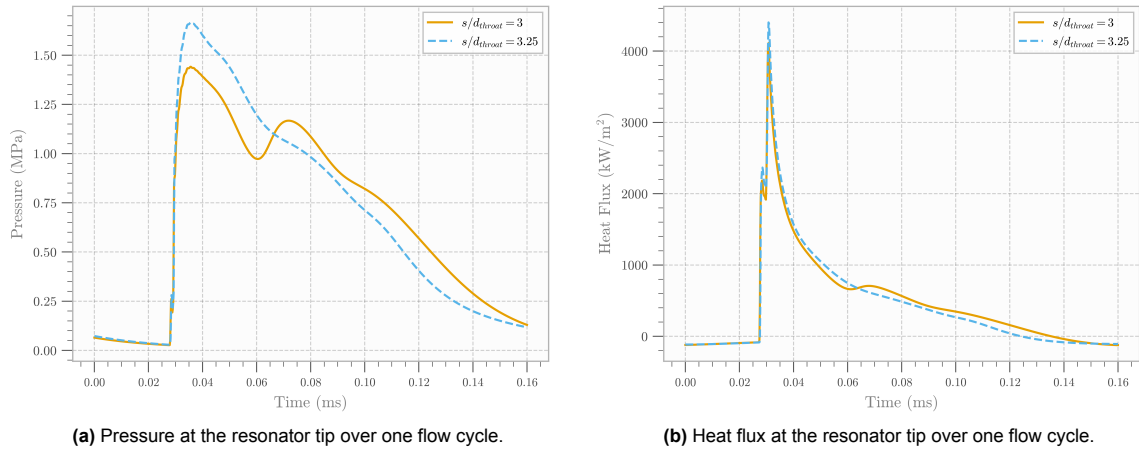


Figure 5.19: $s/d_{throat} = 3.0$ and $s/d_{throat} = 3.25$, both at NPR = 6.8, nitrogen.

Instead, $s/d_{throat} = 3$ has a higher heat flux when integrated over the duration of a flow cycle. At this nozzle gap spacing a second pressure rise at 0.07 ms is visible, that is not present in the case of $s/d_{throat} = 3.25$. This seems to represent an additional pressure wave entering the cavity behind the incident shock wave. It is also visible as slight increase in heat flux at 0.07 ms in [Figure 5.19b](#).

This secondary pressure wave prolongs the dwell time of the hot gas inside the resonator tip. While the maximum pressure is higher for $s/d_{throat} = 3.25$, the longer dwell time results in higher heating power at $s/d_{throat} = 3$. This seems to be a unique phenomenon associated with this particular gap spacing and pressure ratio. Other set points feature similar secondary pressure waves entering the cavity. These, however, do not contribute significantly to wall heat flux, either because the waves are very weak or because of a longer delay between the shock wave and entering pressure wave.

5.6.5. Effect of Upstream Pressure

The tip temperature can be increased by increasing the upstream oxygen pressure. The choked nozzle flow ensures that the NPR is maintained between 7.2 and 7.3. [Figure 5.20](#) shows the increase in maximum tip temperature with increasing oxygen total pressure. For an ideal gas, the static temperature ratio over a shock wave depends only on pressure ratio over the shock wave and the ratio of specific heats [17]. While the nozzle pressure ratio does not change with increasing total pressure, the static pressure inside the resonator increases. A higher static pressure increases the specific heat capacity and thermal conductivity of oxygen [36], thereby increasing the maximum wall temperature. The ratio of specific heats also increases at higher pressure, increasing the static temperature ratio over a shock wave.

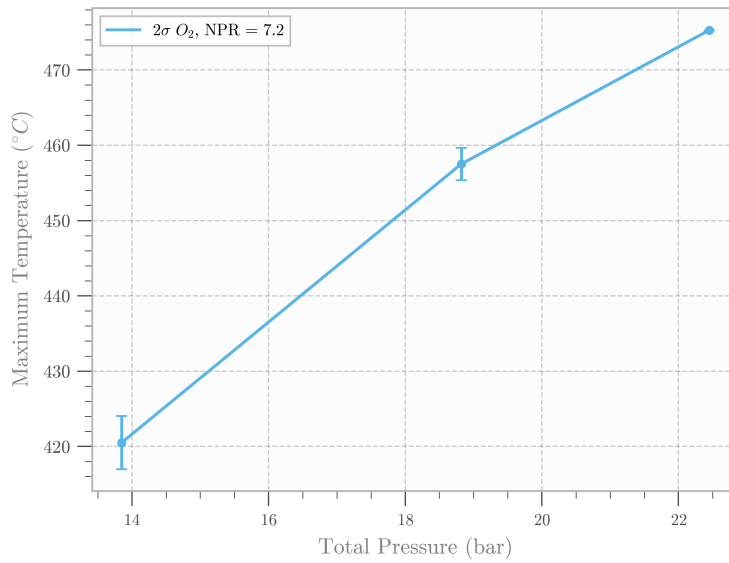


Figure 5.20: Maximum tip temperature when as a function of oxygen total pressure. Two tests were conducted for the first two pressure settings and only a single one for the highest pressure.

Figure 5.21 shows the measured tip temperature as a function of s/d_{throat} , similar to Figure 5.17a. Here nitrogen is used at an upstream total pressure of 16.6 bar, as opposed to the 10.2 bar upstream pressure used in the previously shown results. This shows that the optimum point of heat generation does not shift significantly with an increase in upstream pressure, if the NPR remains approximately constant. The maximum temperature remains at $s/d_{throat} = 3$. The difference between $s/d_{throat} = 3$ and $s/d_{throat} = 3.25$ is less pronounced in Figure 5.21 compared to Figure 5.17a. This could be a result of a slight shift in NPR from 6.8 to 7.0 as the pressure increases.

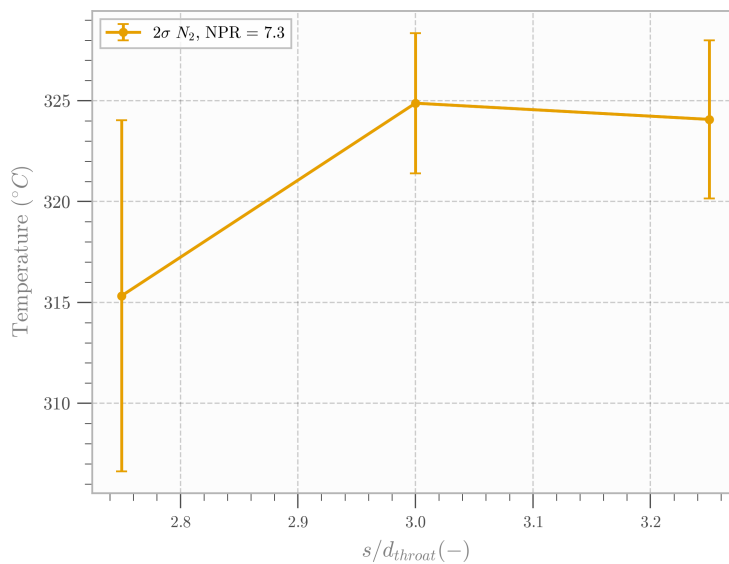


Figure 5.21: Tip temperature as a function of s/d_{throat} using nitrogen at 16.6 bar upstream pressure after 6 seconds of resonance heating.

5.6.6. Effect of Inlet Geometry

The specific geometry of the resonator inlet is known to have a strong effect on the conditions under which a switch in operating modes occurs [24]. The results presented in [subsection 5.6.2](#) show some discrepancy in the nozzle gap spacing at which JRM is first observed, when compared to results by Bauer et al. [12]. The difference between these results could be explained by the difference in resonator inlet geometry. Bauer et al. [12] use a narrow cavity inlet with a thickness of approximately 1.2 mm, compared to the 4.5 mm thick, blunt cavity inlet used in this study. In order to investigate this difference, an alternate resonator was modified to feature a large 45° chamfer at the cavity inlet, as shown in [Figure 5.4](#). A parametric sweep was conducted between $s/d_{throat} = 1.5$ and $s/d_{throat} = 4$ using the same nozzle pressure ratio as for the tests with a cylindrical inlet.

The spectra with respect to nozzle gap spacing are shown in [Figure 5.22](#), tested using nitrogen at NPR = 6.8. These show a delay in the onset of JRM compared to [Figure 5.14a](#), using the cylindrical resonator inlet. In [Figure 5.22](#), at $s/d_{throat} = 2$, the natural frequency of the cavity is barely visible. It only becomes the mode with the highest amplitude at $s/d_{throat} = 2.5$. This indicates that the conical resonator inlet delays the transition from JSM to JRM by approximately $\Delta s/d_{throat} = 0.5$.

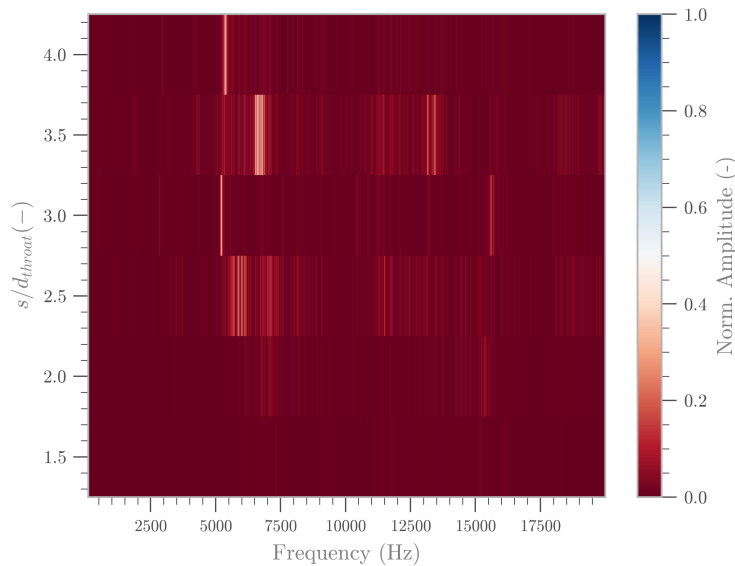


Figure 5.22: Frequency spectrum for different s/d_{throat} for nitrogen, using the modified conical resonator inlet. NPR = 6.8

These results support the hypothesis that the narrow resonator inlet shifts the onset of JRM to larger s/d_{throat} and explains the results in [subsection 5.6.2](#). Another important difference in the igniter design used by Bauer et al. is that the resonator is mounted axially inside the main combustion chamber [12]. The outflow from the cavity can expand radially around the resonator inlet and flow towards the downstream exhaust nozzle. In the design presented here, the combustion chamber is perpendicular to the flow of resonating gas. The majority of the outflow therefore moves downwards from the cavity inlet or around the under-expanded jet. The predominant direction of the outflow from the resonance cavity has an impact on the pressure field upstream of the cavity, in turn directly influencing the conditions for the next inflow cycle. This can impact the stability of a jet regurgitant mode [26].

Universal claims about the onset of certain operating modes as a function of nozzle gap spacing or pressure ratio must therefore be analysed critically, as several other geometric parameters appear to influence thermo-acoustic resonance. As shown in [subsection 5.6.3](#) a 2D axis-symmetric simulation is capable of accurately predicting the switch between operating modes, in the case of this particular geometry. A further validation study using the modified, conical inlet geometry is shown in [Appendix B](#). Here too the numerical model is able to predict the onset of JRM.

5.7. Non-Pre-Mixed Ignition Tests

The combustion experiments presented here aimed to demonstrate ignition using non-pre-mixed oxygen and methane. Six attempts at ignition were made, while independently varying upstream pressure of oxygen and methane after each test. This allowed testing a range of mixture ratios and resonator tip temperatures. None of the ignition attempts were successful despite favourable equivalence ratios and high resonator tip temperatures. The reasons for these ignition failures and fundamental limitations of non-pre-mixed designs are explored.

5.7.1. Temperature Profile and Decay of Resonance

During all ignition tests, oxygen was used as the resonating gas, with methane injected perpendicular to the under-expanded oxygen jet. The flow of oxygen heated the resonator tip for 14 seconds. Methane was injected at T+14 seconds, while the oxygen was still flowing. At T+16 seconds both main valves were closed followed by a nitrogen purge.

An insulator in the form of an aluminium cap over the outside of the resonator was used to increase tip temperature. This significantly reduced heat loss at the tip through forced convection. Figure 5.23a shows resonator tip temperature for three of the ignition tests. All tests were conducted at $s/d_{throat} = 3.0$ but at increasing oxygen total pressure. The location of the thermal probe is measured to be between $x/L = 0.9$ and $x/L = 1.0$, representing the point of expected maximum temperature [27]. Brocher and Maresca show that the highest temperature in a thermo-acoustic resonator is localised only to the resonator tip, quickly dropping towards the resonator inlet [27]. In Figure 5.23a the thermocouple shows a rapid temperature rise once the oxygen is injected. This temperature nearly reaches a steady state at T+14 seconds. Note that the temperature profile shown is corrected for the response time of the spot welded thermocouple, according to Oliveira, Avrit, and Gradeck [64].

As the temperature on the inside of the resonance cavity is critical for ignition, A method of thermal resistances was used to estimate the inner wall temperature of the resonator tip. An estimate of heat loss due to free convection from [65] and heat conduction in radial coordinates (outlined in Appendix C). This results in a maximum inner wall temperature estimate of $477.1\text{ }^{\circ}\text{C}$ for an oxygen total pressure of 22.45 bar.

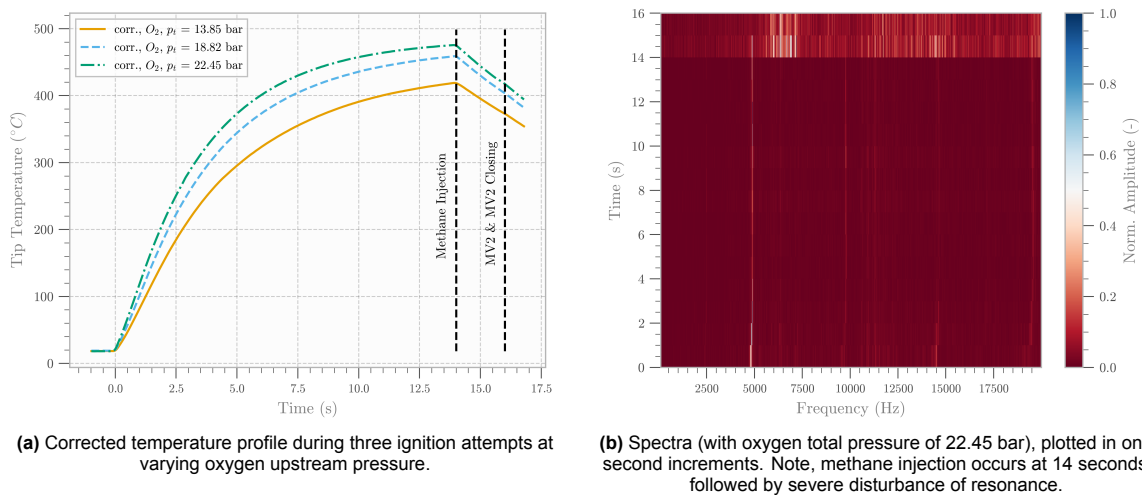


Figure 5.23: System behaviour during ignition attempt

Figure 5.23b shows a spectrum taken every second during an ignition test. During resonance heating a clear jet regurgitant mode is visible. Once methane is injected at T+14 seconds, the characteristic peak around 4900 Hz reduces in relative amplitude and disappears completely at T+15 seconds. The injection of methane appears to severely destabilise the acoustic resonance, consequently ending the ongoing resonance heating. Iwamoto defines two necessary conditions for sustaining a jet regurgitant mode [26]:

1. A low pressure region in front of the inlet to the resonance cavity is essential for a higher pressure differential between the under-expanded jet and the cavity entrance. This provides good initial conditions for the next inflow phase. The more complete the evacuation of the cavity, the larger the low pressure region around the inlet of the cavity at the end of the outflow phase.
2. A uniform pressure gradient, in the mean flow direction, is required in front of the resonator inlet. This means that there needs to be uniform pressure recovery behind the under-expanded jet, with a region of high pressure that covers the entirety of the resonator inlet. Non-uniformities in a radial or tangential direction (relative to the mean flow) can severely distort the inflow into the cavity.

Both the low pressure region at the cavity inlet, as well as the uniform pressure gradient are disrupted by the high speed flow of methane colliding with the resonating oxygen. As a result, [Figure 5.23a](#) shows a steady decrease in tip temperature once the methane is injected. The slope in [Figure 5.23a](#) at T+14 seconds is very similar to the slope at T+16 seconds (when both main valves are closed and the purge valve is opened). This, together with [Figure 5.23b](#) indicate, that the injection of methane perpendicular to the resonating oxygen completely ceases acoustic resonance and prevents any further resonance heating. This means that mixture of oxygen and methane now entering the resonance cavity can no longer use the heat generated during the inflow cycle of JRM to heat it beyond its auto-ignition temperature. Instead, the only remaining source of heat is the rapidly cooling resonator wall. The low thermal inertia resonator tip results in rapid heat loss to the environment once resonance heating subsides.

Note that [Figure 5.23b](#) also shows a shift in the fundamental frequency of the cavity from 4800 Hz to 4890 Hz. The shift is visible between T+0 seconds and T+14 seconds, with the strongest variation near the start of the test. As the wall temperature of the resonance cavity increases, the maximum gas temperature inside the cavity also increases. During the compression cycle, the gas loses less heat to the already heated resonator wall. During the expansion cycle the hot wall returns heat back to the gas. This increases the local speed of sound of the gas, thereby increasing the fundamental frequency of the cavity.

5.7.2. Mixture Ratio

The equivalence ratio is an important parameter for both the ignition delay and auto-ignition temperature of the mixture [45] [42]. Asaba et al. observe ignition delays between 0.1 ms and 1.5 ms for mixtures of oxygen and methane, over a temperature range between 800 K and 2000 K and at pressures between 3 bar and 7 bar. The shortest ignition delay consistently occurs between $\phi = 1$ and $\phi = 1.3$ over the temperature range [45]. A short ignition delay is critical for thermo-acoustic igniters, due to the very short duration of each compression cycle in JRM. The incoming and reflected shock waves cause pressure and temperature peaks lasting less than 0.1 ms, as shown in [Figure 5.19a](#). During the following expansion, the mixture cools rapidly inside the resonator tip.

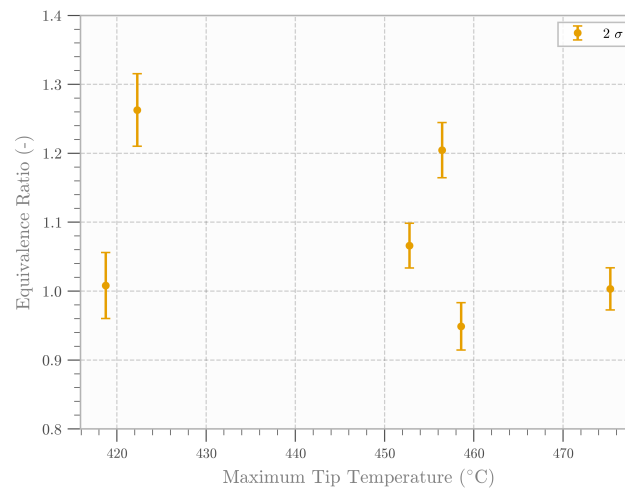


Figure 5.24: Equivalence ratios and maximum measured tip temperature for each ignition attempt. Fuel and oxidiser mass flow are determined based on measured upstream pressure and orifice size. Error is based on fluctuations in measured pressure sensor data.

Figure 5.24 shows that the six ignition test attempts fell within an equivalence ratio of $0.9 < \phi < 1.3$. This indicates that the global equivalence ratio inside the combustion chamber was favourable for a short ignition delay and low auto-ignition temperature. However, Figure 5.24 does not show the equivalence ratio at the tip of the resonance cavity. It can be assumed that the oxygen and methane are not perfectly mixed when entering the resonance cavity, meaning that the mixture ratio inside the tip of the resonance cavity is probably far off of a stoichiometric mixture ratio.

5.8. Conclusion

A test setup for a thermo-acoustic igniter with exchangeable resonators and variable s/d_{throat} was constructed. A prototype igniter was design that uses non-pre-mixed gaseous oxygen and methane as propellants. A microphone was used to determine the operating mode of the igniter, with thermocouples spot welded to the tip of the resonance cavity used to determine wall temperature. Resonance heating experiments were conducted with both oxygen and nitrogen, at different s/d_{throat} and upstream pressures. The parametric sweep with nitrogen was used to identify the switch from a jet screech mode to a regurgitant mode. In these experiments JRM still occurs at the first shock structure at a nozzle pressure ratio of 6.8. When compared to results by other authors, this indicates that the the onset of JRM is likely not universal to a combination of s/d_{throat} and NPR, but instead also depends on the cavity inlet geometry and surrounding combustion chamber. Both have a direct impact on the pressure field upstream of the cavity inlet and therefore on the stability of the regurgitant mode. Increasing the upstream pressure consistently leads to higher resonator tip temperature and a faster temperature rise in the pressure range of 14 bar to 23 bar.

In conjunction with the resonance heating experiments, a numerical model of the acoustic resonance was made using the Open Source CFD software, SU2. A 2D axis-symmetric, non-ideal, compressible, URANS simulation is capable of accurately predicting the switch to the jet regurgitant mode. This has been demonstrated for different cavity inlet geometries. Extensive validation of the model was performed using a variety of s/d_{throat} and with both oxygen and nitrogen. The error in predicted fundamental frequency is consistently below 10%, and as low as 2.6%. This combined with the low computational cost makes the simulation approach used in this study useful for the preliminary design of resonance igniters.

The simulations were carried out on a fully structured grid. A mesh refinement study bases on a grid convergence index and Richardson extrapolation were conducted. This shows a low sensitivity of the flow density on the mesh resolution. The wall heat flux, however, shows a much stronger dependence on mesh refinement, despite achieving $y^+ < 1$ along the length of the resonator on the nominal mesh.

The Peng-Robinson equation of state, implemented in SU2, is well-suited for the predicting gas properties in the flow regime encountered inside the under-expanded jet, as well as the resonance cavity. The use of state dependent C_p and C_v are important for the accurate prediction of wall heat flux during the JRM cycle.

The set point of highest simulated heating power is the result of longer flow dwell time due to a secondary pressure wave as opposed to the strongest incident shock wave. This phenomenon was only observed at $s/d_{throat} = 3$ and NPR = 6.8 and requires further investigation. This operating point provides a 9.8% increase in simulated heating power and corresponds to a measured 9% increase in tip temperature measured experimentally.

Six ignition attempts were made with oxygen as the gas driving the resonance and methane as fuel. Equivalence ratios were varied between 0.9 and 1.3. None of the ignition attempts were successful. The failure to ignite fundamentally represents an issue with non-pre-mixed resonance igniter designs using gaseous fuels. The collision between two high speed gas flows of similar mass flow is found to disrupt the JRM and resonance heating. The use of pre-mixed designs is therefore recommended for gaseous fuels. It is possible that the use of a lower fuel mass flow, therefore operating at very lean conditions could cause less disturbance of the resonance. This, however, also reduces the amount of fuel that is entrained into the resonance cavity and could result in very low equivalence ratios near the cavity tip, in turn increasing ignition delay and auto ignition temperature.

6

Conclusions

The research objective of this thesis was *to investigate the performance envelope of a non-pre-mixed oxygen/methane resonance igniter experimentally, and develop a numerical model capable of predicting the operating mode of the igniter based on nozzle gap spacing and operational parameters*. Based on this, several research questions were identified related both to the validation of a simplified numerical model of resonance heating and the experiments with non-pre-mixed ignition. The research question and sub-questions on the numerical model and its validation are repeated below.

Could a simplified numerical model predict the heating performance of a thermo-acoustic igniter as a function of nozzle gap spacing and operating point?

1. How accurately can the switch between the jet screech mode and jet regurgitant mode be predicted numerically and reproduced experimentally?
2. How accurately can these simulations predict which nozzle gap spacing and operating points cause high rates of resonance heating?
3. What measuring equipment can be used to accurately determine the operating mode of small-scale thermo-acoustic igniters, while not interfering with the acoustic resonance?

Several conclusions can be drawn about the operating modes based on experimental results. The onset of JRM does not immediately result in high rates of resonance heating. Only when s/d_{throat} is increased beyond this onset to 2.5, does the tip temperature increase significantly. This study observes no significant heat generation in JSM either experimentally or in simulation. Other authors that have reported high rates of resonance heating in JSM generally do so at a higher NPR [28] [25] compared to the pressure ratio of between 6.4 and 7.2 used in this study.

This thesis shows that the onset of a jet regurgitant mode in a resonance igniter can be predicted using a simplified numerical model. A 2D axis-symmetric URANS simulation is shown to predict the switch of operating mode as a function of nozzle gap spacing and resonance cavity inlet geometry. The comparatively low computational cost of this model makes it valuable for igniter design and parametric studies.

The error in fundamental frequency predicted by the simulations is below 10%, and as low as 2.6%. Validation of these simulations was carried out with experimental data obtained at different s/d_{throat} , different driving gases (oxygen and nitrogen), as well as two different resonator inlet geometries. Simulations with nitrogen as the driving gas predict the nozzle gap spacing that results in the highest rate of resonance heating. The same prediction was found to be less accurate in the case of oxygen.

The use of a sensitive microphone placed outside of the resonance igniter, near the resonator tip, proved very effective for determining the operating mode of the igniter. With a sampling rate of 100 kHz it was able to resolve not only the fundamental frequency of the cavity, but also several of its overtones. It is likely that especially these overtones were more strongly attenuated by travelling through

the resonance cavity wall. However, the use of a microphone allows for accurate, non-invasive measurement of the acoustic resonance. The small scale of the cavity makes a direct measurement of the pressure of the resonating gas very difficult. The presence of a pressure port inside the cavity might also disrupt the resonating flow.

The resonance heating tests with nitrogen and oxygen were used to demonstrate that both oxygen and nitrogen experienced the highest rates of resonance heating around $s/d_{throat} = 3$ at an NPR between 6.8 and 7.2. This was used as a starting point for six combustion experiments using oxygen and methane. Equivalence ratio of $0.9 < \phi < 1.3$ were tested. The research questions related to the ignition tests are repeated below.

How does the use of non-pre-mixed, gaseous propellants impact the ignition reliability of a thermo-acoustic igniter?

1. How stable is the resonance heating with respect to changing upstream pressure. Which upstream pressure provides the best conditions for ignition?
2. What are the fundamental differences in the resonance heating envelope when using different driving gases?

One of the most consequential results of this study are the ignition attempts conducted with a non-pre-mixed igniter using gaseous propellants. The separate injection of methane was found to destabilise the acoustic resonance and stop resonance heating entirely. This results in almost no methane being entrained into the resonance cavity, as well as low tip temperatures once the fuel is injected. As a result, none of the ignition tests were successful. This represents a fundamental issue with non-pre-mixed igniters with gaseous propellants. Despite global mixture ratios that were close to a stoichiometric ratio, no trace of ignition was observed in either temperature or pressure measurements

Increasing the upstream pressure from 14 bar to 23 bar of oxygen total pressure led to a consistent increase in the measured resonator tip temperature. Due to the use of a choked exhaust nozzle during resonance heating, the NPR remained almost constant over this increase in pressure. Increasing the upstream pressure also has little effect on the s/d_{throat} that results in maximum tip temperature, if the NPR is kept constant.

Both nitrogen and oxygen were tested over a range of nozzle gap spacings and at varying upstream pressures. The use of manually set diaphragm regulators resulted in the set pressure and, therefore, the NPR varying slightly between tests. This makes it very difficult to show an accurate comparison of the maximum attainable tip temperature. As previously demonstrated, the upstream pressure directly affects the rate of resonance heating. The parametric sweeps conducted with oxygen showed a significant decrease in resonance heating at $s/d_{throat} > 3.25$ at NPR = 6.4. Nitrogen by comparison produced reasonably high tip temperatures up to $s/d_{throat} = 4$, with higher tip temperatures across all nozzle gap spacings. In these results it is difficult to account for the effect of reduced upstream pressure. Tests with nitrogen show a 7.3% higher natural frequency of the acoustic cavity. This means that over the same period of resonance heating, a cavity with nitrogen undergoes more JRM cycles and, therefore, more cycles of irreversible heating. It is likely that this contributes to the observed difference between the two gases. Further experimentation is required for conclusive results on the different behaviour of the two driving gases.

Testing with nitrogen shows that it can be used to find operating points of interest that can then be verified with oxygen. This allows for large number of the experiments to be performed with an inert gas, with fewer tests performed with a highly reactive gas. This could be used to simplify initial testing of a new igniter design or qualification of a test setup.

7

Recommendations

Several recommendations can be made for future research into thermo-acoustic igniters, based on the experimental and numerical work conducted in this thesis. These include proposed improvements to the experimental setup, new research directions based on the results obtained in this study and further developments of the numerical model.

7.1. Thermo-Acoustic Heating Experiments

The pressure control of the gas supply of oxygen, nitrogen and methane was accomplished using manually operated diaphragm regulators. During heating and combustion tests these showed a significantly lower measured pressure than the set pressure of the regulator. This is a result of regulator droop at high volume flow rates and is an inherent problem when using diaphragm regulators for high flow applications. This problem is exacerbated when testing at higher pressures, as the mass flow of driving gas increases. As a result, the the maximum oxygen pressure measured during heating tests was 23 bar at a regulator set pressure of approximately 40 bar. Dome loaded regulators or active pressure control devices can be employed that feature higher volumetric flow rates than the diaphragm regulators. Specifically, active pressure control can also improve test turnaround time as changes in the upstream pressure can be set remotely. Most importantly, these regulators could be used to repeatedly set the same upstream pressure and provide a better comparison between different driving gases than the manually set regulators used in this study. When using these regulators, higher oxygen pressures could be set for driving acoustic resonance, either increasing the maximum tip temperature or decreasing the heating time required to attain a certain temperature.

Experiments with mono-atomic gases would be very interesting to use as an additional validation case for the numerical model. Using helium as the driving gas is expected to increase heating of the cavity tip substantially [35]. The effect of the gas composition on the onset of operating modes could also be investigated, if these results are compared to heating tests with oxygen or nitrogen.

The use of additive manufacturing for the tip of the resonator allows for creating small-scale geometries that are otherwise very challenging to manufacture in metals. Without post-processing the surface of SLM printed parts is very rough compared to a machined surface. This is also the case for the acoustic cavity used in this study. High surface roughness also directly impacts heat transfer through the cavity wall, as well as heat generation in the entrained gas [54]. The effect of the surface roughness on resonance heating and on the shock waves travelling in and out of the resonance cavity is a potential topic for further study. It is important to determine at which relative roughness height the resonance behaviour is impacted and to derive some requirements for the manufacture of these cavities.

7.2. Pre-Mixed Operation

The prototype igniter and fluid system are designed specifically for combustion experiments. An outcome of the experiments with non-pre-mixed gaseous propellants is that ignition under these circumstances is very difficult to accomplish. As such, experiments with pre-mixed propellants in this igniter

are encouraged. The existing operational and design safety measures implemented for the test setup make it suitable for testing with pre-mixed oxygen and methane. This would require the addition of flashback arrestors on both the methane and oxygen supply lines in order to prevent the flame front propagating back into one of the propellants lines. The check valves, currently installed on the system, are insufficient to prevent flashback when using pre-mixed, gaseous propellants. With successful ignition tests, several new avenues of research could be explored. The mixture ratio limits of resonance ignition could be analysed. Additionally, the lower limit of resonator tip temperature, which still results in ignition, is an important operational parameter for any igniter design.

For combustion experiments the thermal failure of the resonator is likely when operated for more than a few seconds and at mixture ratios near stoichiometric. A possible mitigation strategy is to implement software based thermal limits in the automated valve sequence. These could use the temperature measured at the resonator tip to set a condition for automatic closing of the main valves, if the tip temperature exceeds a critical value. This is a very useful safety measure to prevent excessive temperature at the resonator tip and reducing the risk of damage to the test setup.

7.3. Instrumentation

The simulations of resonance heating at different nozzle gap distances are used to show why $s/d_{throat} = 3$ at NPR = 6.8 shows significantly higher rates of resonance heating with nitrogen. Confirming these hypotheses experimentally would be very valuable for a better understanding of the heating mechanisms in JRM. This could be accomplished by placing a pressure transducer at the tip of the resonance cavity. This is extremely challenging at the resonator scale used in this thesis, but might be possible for larger cavities. The use of additive manufacturing might also allow for smaller pressure ports near the cavity tip.

7.4. Numerical Model

The simulation method used in this thesis could be improved though the use of higher order schemes to approximate convective flux. The current implementation relies on first order upwind methods, which are highly dissipative and not ideal for the resolution of the incident and reflected shock waves. The use of a second order MUSCL reconstruction in SU2 was attempted but was found to be highly unstable. The use of such a scheme, or another higher order method, would allow for a more accurate estimation of temperature and pressure, especially at the cavity tip.

A conjugate unsteady heat transfer and flow simulation could provide a direct comparison between simulated and experimental tip temperature. The large difference in flow and conductive time scales makes any multi-physics simulation very computationally expensive. A method to overcome the problem posed by the large difference time scales is suggested in [section D.3](#). Using this, the measured temperature at the resonator tip and the simulated wall temperature could be compared directly.

The predictive capability of the simulation means that it can be used to investigate a variety of in-flight conditions that are more challenging to test experimentally. Any practical igniter design is likely to use evaporated cryogenic propellants, stored onboard a rocket or satellite. This requires qualifying the igniter design for very low propellant inlet temperatures. Simulation at these representative upstream conditions can take full advantage of the cubic equation of state used in this simulation and can be used to determine operational limits for the thermo-acoustic heating.

Lastly, SU2 features an implementation of an adjoint solver that can be combined with the existing simulation setup presented in this thesis. This could provide the basis for cavity shape optimisation with the objective of maximum wall heat flux or maximum fluid temperature.

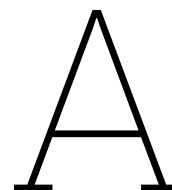
References

- [1] George Paul Sutton. *Rocket propulsion elements*. Ed. by Oscar Biblarz. Ninth edition. Includes bibliographical references and index. Hoboken, New Jersey: John Wiley & Sons Inc, 2017. 767 pp. ISBN: 9781118753651.
- [2] David H. Huang and Dieter K. Huzel. *Modern Engineering for Design of Liquid-Propellant Rocket Engines*. American Institute of Aeronautics and Astronautics, Jan. 1992. DOI: [10.2514/4.866197](https://doi.org/10.2514/4.866197).
- [3] *MEMBER STATE COMMITTEE SUPPORT DOCUMENT FOR IDENTIFICATION OF HYDRAZINE AS A SUBSTANCE OF VERY HIGH CONCERN BECAUSE OF ITS CMR PROPERTIES*. Tech. rep. EC number: 206-114-9. CAS number: 302-01-2. European Chemicals Agency, 2011.
- [4] B. Nufer. "A Summary of NASA and USAF Hypergolic Propellant Related Spills and Fires". In: (). DOI: [10.2514/6.2010-1994](https://doi.org/10.2514/6.2010-1994). URL: <https://arc.aiaa.org/doi/abs/10.2514/6.2010-1994>.
- [5] Felix Lauck et al. "Green bipropellant development – A study on the hypergolicity of imidazole thiocyanate ionic liquids with hydrogen peroxide in an automated drop test setup". In: *Combustion and Flame* 226 (2021), pp. 87–97. ISSN: 0010-2180. DOI: <https://doi.org/10.1016>.
- [6] R. K. Palmer and J. J. Rusek. "Low-Toxicity Reactive Hypergolic Fuels for Use with Hydrogen Peroxide". In: *ESA Special Publication*. Ed. by A. Wilson. Vol. 557. ESA Special Publication. Oct. 2004, 32.1, p. 32.1.
- [7] Sebastian Schuh et al. "Results of material compatibility investigation of hydrogen peroxide". In: *51st AIAA/SAE/ASEE Joint Propulsion Conference*. American Institute of Aeronautics and Astronautics, July 2015. DOI: [10.2514/6.2015-4252](https://doi.org/10.2514/6.2015-4252).
- [8] S. Mustafi et al. "Cryogenic propulsion for the Titan Orbiter Polar Surveyor (TOPS) mission". In: *Cryogenics* 74 (Mar. 2016), pp. 81–87. ISSN: 0011-2275. DOI: [10.1016/j.cryogenics.2015.11.009](https://doi.org/10.1016/j.cryogenics.2015.11.009).
- [9] G. A. Repas. *Hydrogen-Oxygen Torch Ignitor*. Tech. rep. NASA Technical Memorandum 106493, 1994.
- [10] William Marshall, Robin Osborne, and Sandra Greene. "Development of Augmented Spark Impinging Igniter System for Methane Engines". In: July 2017. DOI: [10.2514/6.2017-4665](https://doi.org/10.2514/6.2017-4665).
- [11] Darren C Tinker. "Compact Augmented Spark Igniters for Liquid Rocket Engines". PhD thesis. Vanderbilt University, 2021.
- [12] Christian BAUER, Paul LUNGU, and Oskar J. HAIDN. "Numerical Study on a Resonance Ignition System". In: (2019). DOI: [10.13009/EUCASS2019-360](https://doi.org/10.13009/EUCASS2019-360).
- [13] Jul Hartmann. "On a New Method for the Generation of Sound-Waves". In: *Physical Review* 20.6 (Dec. 1922), pp. 719–727. DOI: [10.1103/physrev.20.719](https://doi.org/10.1103/physrev.20.719).
- [14] M. Sprenger. "Ueber thermische Effekte in Resonanzrohren". In: *Mitteilungen aus dem Institute für Aerodynamik au der E.T.H. Zurich, Vol. 21, pp. 18-35.* (1954).
- [15] A. J. Pavli E. E. Conrad. *Resonance-Tube Igniter For Hydrogen-Oxygen Rocket Engines*. Tech. rep. TM X-1460, NASA, 1967.
- [16] Edward M. Greitzer, Choon Sooi Tan, and Martin B. Graf. *Internal flow. Concepts and applications*. Digitally printed 1. paperback version. Cambridge engine technology series 3. Cambridge: Cambridge Univ. Press, 2006. 706 pp. ISBN: 9780521036726.
- [17] John David Anderson. *Modern compressible flow. With historical perspective*. 3. ed., internat. ed. McGraw-Hill series in aeronautical and aerospace engineering. Boston, Mass. [u.a.]: McGraw-Hill, 2003. 760 pp. ISBN: 0072424435.

- [18] Hadi Samsam-Khayani et al. "Visualization of supersonic free jet flow structures subjected to various temperature and pressure ratio conditions". In: *Optics and Lasers in Engineering* 158 (Nov. 2022), p. 107144. DOI: [10.1016/j.optlaseng.2022.107144](https://doi.org/10.1016/j.optlaseng.2022.107144).
- [19] Francesco Duronio, Carlo Villante, and Angelo De Vita. "Under-Expanded Jets in Advanced Propulsion Systems—A Review of Latest Theoretical and Experimental Research Activities". In: *Energies* 16.18 (Sept. 2023), p. 6471. DOI: [10.3390/en16186471](https://doi.org/10.3390/en16186471).
- [20] TJB Smith and Alan Powell. *Experiments concerning the Hartmann whistle*. University of California, Department of Engineering, 1964.
- [21] V. Sarohia and L. Back. "Experimental Investigation of Flow and Heating in a Resonance Tube". In: *J. FluidMech.*, no. 94 (1979).
- [22] Christian BAUER, Martin HAUSER, and Oskar J. HAIDN. "Investigation of Stabilization Effects in Hartmann-Sprenger Tubes". In: *TRANSACTIONS OF THE JAPAN SOCIETY FOR AERONAUTICAL AND SPACE SCIENCES, AEROSPACE TECHNOLOGY JAPAN* 14.ists30 (2016), Pa_95–Pa_100. DOI: [10.2322/tastj.14.pa_95](https://doi.org/10.2322/tastj.14.pa_95).
- [23] Shekhar Sarpotdar, Ganesh Raman, and Alan B. Cain. "Powered resonance tubes: resonance characteristics and actuation signal directivity". In: *Experiments in Fluids* 39.6 (Sept. 2005), pp. 1084–1095. DOI: [10.1007/s00348-005-0041-5](https://doi.org/10.1007/s00348-005-0041-5).
- [24] G.B. Sobieraj and A.P. Szumowski. "Experimental investigations of an underexpanded jet from a convergent nozzle impinging on a cavity". In: *Journal of Sound and Vibration* 149.3 (Sept. 1991), pp. 375–396. DOI: [10.1016/0022-460x\(91\)90443-n](https://doi.org/10.1016/0022-460x(91)90443-n).
- [25] Dustin Bouch and Andrew Cutler. "Investigation of a Hartmann-Sprenger Tube for Passive Heating of Scramjet Injectant Gases". In: *41st Aerospace Sciences Meeting and Exhibit*. American Institute of Aeronautics and Astronautics, Jan. 2003. DOI: [10.2514/6.2003-1275](https://doi.org/10.2514/6.2003-1275).
- [26] Junjiro Iwamoto. "Necessary conditions for starting and maintaining a stable oscillatory flow in a Hartmann-Sprenger tube". In: *Flow Visualization IV*. Jan. 1987, pp. 507–512.
- [27] E. Brocher and C. Maresca. "Etude des phenomenes thermiques dans un tube de Hartmann-Sprenger". In: *International Journal of Heat and Mass Transfer* 16.3 (Mar. 1973), pp. 529–538. DOI: [10.1016/0017-9310\(73\)90221-4](https://doi.org/10.1016/0017-9310(73)90221-4).
- [28] Roman A. Marchan. "Small-Scale Supersonic Combustion Chamber with a Gas-Dynamic Ignition System". In: *Combustion Science and Technology* 183.11 (Nov. 2011), pp. 1236–1265. DOI: [10.1080/00102202.2011.589874](https://doi.org/10.1080/00102202.2011.589874).
- [29] K. Grogan and M. Ihme. "StanShock: a gas-dynamic model for shock tube simulations with non-ideal effects and chemical kinetics". In: *Shock Waves* 30.4 (Jan. 2020), pp. 425–438. DOI: [10.1007/s00193-019-00935-x](https://doi.org/10.1007/s00193-019-00935-x).
- [30] PHILIP A. THOMPSON. "Jet-driven resonance tube". In: *AIAA Journal* 2.7 (July 1964), pp. 1230–1233. DOI: [10.2514/3.2526](https://doi.org/10.2514/3.2526).
- [31] Masaaki KAWAHASHI and Makoto SUZUKI. "Thermal Effects in a Hartmann-Sprenger Tube". In: *Bulletin of JSME* 22.167 (1979), pp. 685–692. DOI: [10.1299/jsme1958.22.685](https://doi.org/10.1299/jsme1958.22.685).
- [32] Virendra Sarohia et al. "An Experimental Investigation of Fluid Flow and Heating in Various Resonance Tube Modes". In: 1976. URL: <https://api.semanticscholar.org/CorpusID:94366724>.
- [33] Brian R. Phillips and Albert J. Pavli. "RESONANCE TUBE IGNITION OF HYDROGEN-OXYGEN MIXTURES". In: 1971. URL: <https://api.semanticscholar.org/CorpusID:94163327>.
- [34] Roman MARCHAN et al. "3D printed acoustic igniter of oxygen-kerosene mixtures for aerospace applications". In: (2019). DOI: [10.13009/EUCASS2019-238](https://doi.org/10.13009/EUCASS2019-238).
- [35] V. Marchese E. Rakowsky A. Corrado. "Fluidic Explosive Initiator". In: *Fluidics quarterly*, vol. 6, no. 1 (1974).
- [36] Ian H. Bell et al. "Pure and Pseudo-pure Fluid Thermophysical Property Evaluation and the Open-Source Thermophysical Property Library CoolProp". In: *Industrial & Engineering Chemistry Research* 53.6 (Jan. 2014), pp. 2498–2508. ISSN: 1520-5045. DOI: [10.1021/ie4033999](https://doi.org/10.1021/ie4033999).

- [37] C. E. G. Przirembel and L. S. Fletcher. "Aerothermodynamics of a Simple Resonance Tube". In: *AIAA Journal* 15.1 (Jan. 1977), pp. 101–104. DOI: [10.2514/3.60606](https://doi.org/10.2514/3.60606).
- [38] MG Lebedev and OV Bocharova. "Self-oscillatory flow in the Hartmann resonator – Numerical simulation". In: *International Journal of Aeroacoustics* 19.1-2 (Feb. 2020), pp. 119–154. DOI: [10.1177/1475472x20905037](https://doi.org/10.1177/1475472x20905037).
- [39] Ganesh Raman and K. Srinivasan. "The powered resonance tube: From Hartmann's discovery to current active flow control applications". In: *Progress in Aerospace Sciences* 45.4-5 (May 2009), pp. 97–123. DOI: [10.1016/j.paerosci.2009.05.001](https://doi.org/10.1016/j.paerosci.2009.05.001).
- [40] ROBERT F. MCALEVY and ALEX PAVLAK. "Tapered resonance tubes - Some experiments". In: *AIAA Journal* 8.3 (Mar. 1970), pp. 571–572. DOI: [10.2514/3.5710](https://doi.org/10.2514/3.5710).
- [41] S Sembian and M Liverts. "On using converging shock waves for pressure amplification in shock tubes". In: *Metrologia* 57.3 (Apr. 2020), p. 035008. ISSN: 1681-7575. DOI: [10.1088/1681-7575/ab7f99](https://doi.org/10.1088/1681-7575/ab7f99).
- [42] Roda Bounaceur et al. "Prediction of Auto-Ignition Temperatures and Delays for Gas Turbine Applications". In: *Journal of Engineering for Gas Turbines and Power* 138.2 (Sept. 2015). ISSN: 1528-8919. DOI: [10.1115/1.4031264](https://doi.org/10.1115/1.4031264).
- [43] S. Gordon and B. J. McBride. *Computer Program for Calculation of Complex Chemical Equilibrium Compositions and Applications*. Tech. rep. NASA Reference Publication 1311, 1996.
- [44] Chad V. Mashuga and Daniel A. Crowl. "Application of the flammability diagram for evaluation of fire and explosion hazards of flammable vapors". In: *Process Safety Progress* 17.3 (Sept. 1998), pp. 176–183. DOI: [10.1002/prs.680170305](https://doi.org/10.1002/prs.680170305).
- [45] T. Asaba et al. "A shock tube study of ignition of methane-oxygen mixtures". In: *Symposium (International) on Combustion* 9.1 (Jan. 1963), pp. 193–200. ISSN: 0082-0784. DOI: [10.1016/s0082-0784\(63\)80026-0](https://doi.org/10.1016/s0082-0784(63)80026-0).
- [46] S.-M. CHANG and S. LEE. "ON THE JET REGURGITANT MODE OF A RESONANT TUBE". In: *Journal of Sound and Vibration* 246.4 (Sept. 2001), pp. 567–581. DOI: [10.1006/jsvi.2000.3646](https://doi.org/10.1006/jsvi.2000.3646).
- [47] Stephen B. Pope. *Turbulent flows*. 1. publ., 12. print. Literaturverz. S. 727 - 748. Cambridge [u.a.]: Cambridge Univ. Press, 2015. 771 pp. ISBN: 9780521598866.
- [48] Paul LUNGU, Christian BAUER, and Oskar J. HAIDN. "Design aspects and characterisation of a resonance igniter for oxygen/methane in-orbit propulsion systems". In: (2019). DOI: [10.13009/EUCASS2019-651](https://doi.org/10.13009/EUCASS2019-651).
- [49] Babak Afzali and Hassan Karimi. "Numerical investigation on thermo-acoustic effects and flow characteristics in semi-conical Hartmann–Sprenger resonance tube". In: *Proceedings of the Institution of Mechanical Engineers, Part G: Journal of Aerospace Engineering* 231.14 (Sept. 2016), pp. 2706–2722. DOI: [10.1177/0954410016670419](https://doi.org/10.1177/0954410016670419).
- [50] Christian Bauer and Oskar J. Haidn. "Numerical Investigation of 3D Effects in Hartmann-Sprenger Tubes". In: (2015).
- [51] Meng-Sing Liou. "The Evolution of AUSM Schemes". In: *Defence Science Journal* 60.6 (Nov. 2010), pp. 606–613. ISSN: 0976-464X. DOI: [10.14429/dsj.60.580](https://doi.org/10.14429/dsj.60.580).
- [52] Thomas D. Economon et al. "SU2: An Open-Source Suite for Multiphysics Simulation and Design". In: *AIAA Journal* 54.3 (Mar. 2016), pp. 828–846. ISSN: 1533-385X. DOI: [10.2514/1.j053813](https://doi.org/10.2514/1.j053813).
- [53] Vance F. Dippold. "Computational Simulations of Convergent Nozzles for the AIAA 1st Propulsion Aerodynamics Workshop". In: 2014. URL: <https://api.semanticscholar.org/CorpusID:13997215>.
- [54] A. F. Mills. *Basic Heat and Mass Transfer Pearson New International Edition. Pearson New International Edition*. Pearson Education, Limited, 2013, p. 1032. ISBN: 9781292042480.
- [55] Heinrich Kuttruff. *Acoustics. An introduction*. Includes bibliographical references (p. [451]) and index. London [u.a.]: Taylor & Francis, 2007. 457 pp. ISBN: 9780415386807.

- [56] Timothy C. Lieuwen. *Unsteady combustor physics*. Online-Ausg. Includes bibliographical references and index. - Description based on print version record. Cambridge: Cambridge University Press, 2013. 1405 pp. ISBN: 9781283638647.
- [57] P.L. Roe. "Approximate Riemann solvers, parameter vectors, and difference schemes". In: *Journal of Computational Physics* 43.2 (Oct. 1981), pp. 357–372. ISSN: 0021-9991. DOI: [10.1016/0021-9991\(81\)90128-5](https://doi.org/10.1016/0021-9991(81)90128-5).
- [58] Z. Wang. "A fast nested multi-grid viscous flow solver for adaptive Cartesian/Quad grids". In: *Fluid Dynamics Conference*. American Institute of Aeronautics and Astronautics, June 1996. DOI: [10.2514/6.1996-2091](https://doi.org/10.2514/6.1996-2091).
- [59] Florian Menter, M. Kuntz, and RB Langtry. "Ten years of industrial experience with the SST turbulence model". In: *Heat and Mass Transfer* 4 (Jan. 2003).
- [60] F. R. Menter. "Performance of popular turbulence model for attached and separated adverse pressure gradient flows". In: *AIAA Journal* 30.8 (Aug. 1992), pp. 2066–2072. ISSN: 1533-385X. DOI: [10.2514/3.11180](https://doi.org/10.2514/3.11180).
- [61] Salvatore Vitale et al. "Extension of the SU2 open source CFD code to the simulation of turbulent flows of fluids modelled with complex thermophysical laws". In: *22nd AIAA Computational Fluid Dynamics Conference*. American Institute of Aeronautics and Astronautics, June 2015. DOI: [10.2514/6.2015-2760](https://doi.org/10.2514/6.2015-2760).
- [62] Bruce E. Poling. *Properties of Gases and Liquids, Fifth Edition*. Ed. by John M. Prausnitz and John P. O'Connell. Fifth edition. McGraw-Hill's AccessEngineering. Includes bibliographical references and index. - Description based on e-Publication PDF. New York, N.Y.: McGraw-Hill Education, 2020. 1803 pp. ISBN: 0070116822.
- [63] I. Celik et al. "Procedure of Estimation and Reporting of Uncertainty Due to Discretization in CFD Applications". In: *J. Fluids Eng.* 130 (July 2008), p. 078001. DOI: [10.1115/1.2960953](https://doi.org/10.1115/1.2960953).
- [64] A.V.S. Oliveira, A. Avrit, and M. Gradeck. "Thermocouple response time estimation and temperature signal correction for an accurate heat flux calculation in inverse heat conduction problems". In: *International Journal of Heat and Mass Transfer* 185 (Apr. 2022), p. 122398. ISSN: 0017-9310. DOI: [10.1016/j.ijheatmasstransfer.2021.122398](https://doi.org/10.1016/j.ijheatmasstransfer.2021.122398).
- [65] Stuart W. Churchill and Humbert H.S. Chu. "Correlating equations for laminar and turbulent free convection from a horizontal cylinder". In: *International Journal of Heat and Mass Transfer* 18.9 (Sept. 1975), pp. 1049–1053. ISSN: 0017-9310. DOI: [10.1016/0017-9310\(75\)90222-7](https://doi.org/10.1016/0017-9310(75)90222-7).
- [66] Ryota Muraoka and Toshihiko Hiejima. "Onset conditions for Mach disk formation in underexpanded jet flows". In: *Physics of Fluids* 34.11 (Nov. 2022). ISSN: 1089-7666. DOI: [10.1063/5.0122861](https://doi.org/10.1063/5.0122861).
- [67] Christophe Geuzaine and Jean-François Remacle. "Gmsh: A 3-D finite element mesh generator with built-in pre- and post-processing facilities". In: *International Journal for Numerical Methods in Engineering* 79.11 (May 2009), pp. 1309–1331. ISSN: 1097-0207. DOI: [10.1002/nme.2579](https://doi.org/10.1002/nme.2579).
- [68] Yu Shi et al. "Bi-Fo time scaling method in the numerical simulation of transient conjugate heat transfer". In: *Propulsion and Power Research* 10.3 (Sept. 2021), pp. 209–223. ISSN: 2212-540X. DOI: [10.1016/j.jprr.2021.05.005](https://doi.org/10.1016/j.jprr.2021.05.005).



Igniter Requirements

The validation of the numerical model, as well as the performance characterisation of the igniter require extensive testing of both resonance heating and ignition. Such tests involve some inherent hazards, such as the use of pressurised gases, strong oxidisers and combustion, that need to be understood and managed for all testing activities. This chapter covers the requirements set for the design of the igniter, its combustion chamber and feed system, as well as the requirements set for safe testing of a resonance igniter on the TU Delft campus. A comprehensive list of requirements is needed to define the design space and ensure that the design is in line with the stated research objective. The requirements are split into safety requirements, igniter design requirements, and requirements for the data acquisition system.

A.1. Safety Requirements

The most important set of requirements for this project are those concerning the safety of testing personnel, as well as that of spectators and bystanders. The implementation of these requirements is presented in the form of a detailed risk analysis in [Appendix F](#). Operational safety during the experiments is ensured using test procedures developed for these experiments (shown in [Appendix G](#)) and by the presence of an independent safety officer from DARE at the test campaigns. The safety aspects of the igniter and feed system design are also reviewed by the safety board of DARE before being approved for testing. The set of requirements outlined in [Table A.1](#) gives an overview of the physical design aspects and operational aspects that are to ensure a safe testing process.

Table A.1: Safety Requirements

Identifier	Requirement
SAFE-1	The test shall impose no significant risk of injury to anyone in the vicinity of the test setup.
SAFE-2	Every hot-fire test shall be supervised by an independent Safety Officer from DARE
SAFE-3	Operation of the test setup, while the system is under pressure, shall be performed from a distance of at least 20 m.
SAFE-4	The setup shall have provisions for purging the igniter with inert gas
SAFE-5	The igniter shall be contained within a shrapnel box that covers all lines of sight between the igniter and testing personnel.
SAFE-6	Both oxidiser and fuel lines shall have manual depressurisation valves
SAFE-7	The primary failure mode of the igniter shall be failure at the resonance cavity.
SAFE-8	The test setup and LabVIEW control shall be extensively validated using unit tests before ignition is attempted.

A.2. Design Requirements

This section outlines the requirements for igniter design, including the feed system and test bench. These are based on expected experiment outcome as well as expected design and operational constraints. The latter are driven by the need to be able to test a large operational envelope of the resonance igniter, with different driving gases.

Table A.2: Design Requirements

Identifier	Requirement
DES-1	The igniter shall use gaseous oxygen and gaseous methane as propellants.
DES-2	The igniter shall be capable of operating at a variable nozzle pressure ratio.
DES-3	The igniter shall be capable of operating at a variable of nozzle-to-resonator gap spacing
DES-4	The igniter shall have an oxygen inlet diameter of 2 mm.
DES-5	The igniter body and oxygen inlet shall be reusable components.
DES-6	The resonance cavity and the nozzle of the combustion chamber shall be replaceable using hand tools.

A.3. Sensor Requirements

The proposed research questions require the collection of different types of experimental data. The requirements for the data acquisition system are driven by the need to resolve rapid temperature changes in the resonance cavity, as well as the high frequency oscillations of the possible operating modes.

Table A.3: Sensor Requirements

Identifier	Requirement
SENS-1	The test setup shall feature one high-frequency microphone, near the resonance cavity with a sampling rate of 100 kHz
SENS-2	The igniter shall have pressure transducers, measuring upstream pressure of the propellants at 2 kHz
SENS-3	The igniter shall have a second combustion chamber pressure sensor, measuring at 2 kHz
SENS-4	The igniter shall use thermocouples to measure the wall temperature of the resonance cavity.
SENS-5	The thermocouple shall measure temperature at a frequency of 50 Hz

B

Additional Validation Cases

This appendix shows two additional validation cases for the numerical model presented in [section 5.4](#). The first is based on a shock tube mode introduced in [section 2.3](#). Here the inflow cycle of JRM, modelled by CFD, can be validated against analytical shock wave relations. The second validation case is based on the modified, conical, inlet geometry tested in [subsection 5.6.6](#). Two validation simulations are performed, with the mesh modified to represent the conical inlet. These are then compared to spectra from two experiments.

B.1. Shock Tube Model

Closed form equations exist that can relate the maximum pressure and temperature to the initial pressure ratio in the shock tube. This results in a lumped parameter model that assumes inviscid, adiabatic flow. It is helpful for understanding the influence parameters on the heat generation as a result of the incident and reflected shock wave. These equations assume a calorically perfect gas, with $e = C_v T$ and $p = \rho RT$ [17]. C_p and C_v are assumed constant. [Equation B.1](#) relates the Mach number of the incident shock wave (M_S) to the initial pressure ratio (p_1/p_0), where p_1 is the higher pressure and p_0 the lower pressure. It is assumed that γ and the molecular weight on either side of the diaphragm is the same.

$$\frac{p_1}{p_0} = \frac{2\gamma M_S^2 + 1 - \gamma}{\gamma + 1} \left[1 - \frac{\gamma + 1}{\gamma - 1} \left(M_S - \frac{1}{M_S} \right) \right]^{-\frac{2\gamma}{\gamma - 1}} \quad (\text{B.1})$$

The temperature ratio over a normal shock wave is given in [Equation B.2](#), taken from [17].

$$\frac{T_2}{T_1} = \frac{p_1}{p_0} \left(\frac{\frac{\gamma + 1}{\gamma - 1} + \frac{p_1}{p_0}}{1 + \frac{\gamma + 1}{\gamma - 1} \frac{p_1}{p_0}} \right) \quad (\text{B.2})$$

[Equation B.2](#) only depends on the initial pressure ratio and the ratio of specific heats. As a result, a higher pressure ratio directly correlates with a higher temperature ratio. The Mach number of the reflected shock wave is taken relative to the incoming particle velocity. It depends on the incident Mach number and γ . According to Anderson [17] the reflected Mach number can be determined using [Equation B.3](#).

$$\frac{M_R}{M_R^2 - 1} = \frac{M_S}{M_S^2 - 1} \sqrt{1 + \frac{2(\gamma - 1)}{(\gamma + 1)^2} (M_S^2 - 1) \left(\gamma + \frac{1}{M_S^2} \right)} \quad (\text{B.3})$$

Where M_R is the reflected Mach number. The subsequent pressure rise of the flow due to the reflected Mach number can be computed using [Equation B.4](#). It can be related directly to the incident Mach number, M_S .

$$\frac{p_3}{p_0} = \frac{2\gamma M_S^2 - \gamma + 1}{\gamma + 1} \left[\frac{(3\gamma - 1)M_S^2 - 2\gamma + 2}{(\gamma - 1)M_S^2 + 2} \right] \quad (\text{B.4})$$

Where p_3 is the pressure of the entrained gas after the reflected shock wave has passed over it. The corresponding temperature rise from the reflected shock wave is computed again using Equation B.2, but using the new pressure ratio over the reflected Mach number. As the incident shock wave moves over gas particles inside the shock tube, these begin to move towards the right side, as shown in Figure 2.6. Their movement is eventually halted by the reflected shock wave. This movement towards the closed end of the shock tube causes volumetric compression of the gas on the right side of the diaphragm. This is an isentropic process and can be modelled using Equation B.5 [17].

$$\frac{p'_1}{p_1} = \left(\frac{v_1}{v'_1} \right)^\gamma = \left(\frac{T'_1}{T_1} \right)^{\frac{\gamma}{\gamma-1}} \quad (\text{B.5})$$

The superscript ' denotes the state after compression. The specific volume fraction v_0/v_1 is a function of the particle velocity u_p and the time it takes between the initial movement of the particle front and its collision with the reflected shock wave. The particle velocity can be related to the incident Mach number using Equation B.6.

$$u_p = \frac{a_0}{\gamma} \left(\frac{p_1}{p_0} - 1 \right) \left(\frac{\frac{2\gamma}{\gamma+1}}{\frac{p_1}{p_0} + \frac{\gamma-1}{\gamma+1}} \right)^{0.5} \quad (\text{B.6})$$

Where a_0 is the speed of sound of the gas on the low pressure side of the shock tube.

B.2. Validation Against Shock Tube Model

The shock tube model is useful for estimating the flow profile of the inflow phase of JRM. However, it does not predict the following expansion and outflow from the resonance cavity. This means that the initial state of the cavity (as conditioned by the outflow phase) is not captured by the model and must be assumed. The upstream driving pressure of the gas entering the resonance cavity also needs to be approximated, using flow relations for the under expanded jet.

The Mach number of the under-expanded jet is estimated using the simple empirical correlation shown in Equation B.7 [66]. During the inflow phase the Mach number predicted by Equation B.7 matches that observed in CFD simulations.

$$M = 1.67X_c^{0.7} + 1.0 \quad (\text{B.7})$$

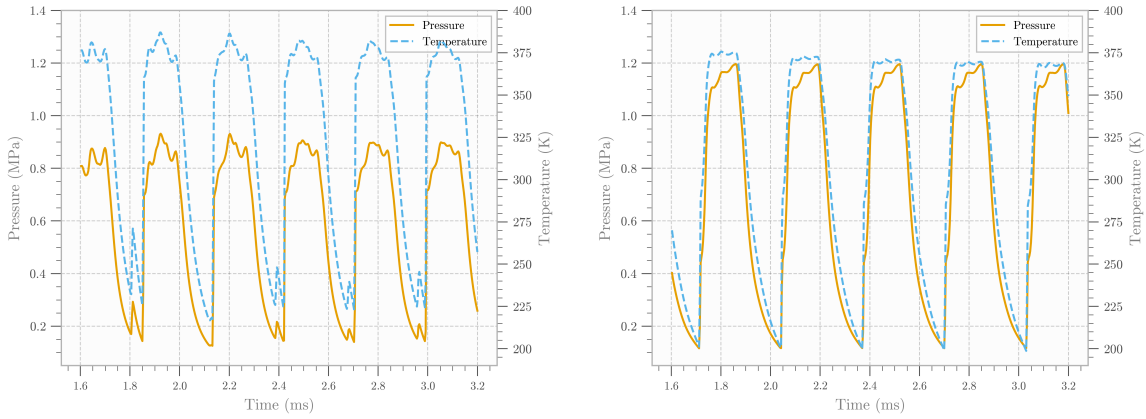
Here X_c is estimated using Equation 5.1. The Mach number can be used to estimate the static pressure after the Mach disk using shock wave relations. The static pressure ratio over the Mach disk is determined using Equation B.8.

$$\frac{p_1}{p_0} = \frac{(\gamma + 1)M^2}{(\gamma - 1)M^2 + 2} \quad (\text{B.8})$$

Where p_1 is the static pressure downstream of the Mach disk and p_0 the static pressure after the Mach disk. Equation B.8 determines the driving pressure p_1 . The pressure and temperature of the resonance cavity at the start of the inflow cycle, p_0 and T_0 , are a result of expansion during the preceding outflow cycle. This is not accounted for in the shock tube model and thus needs to be estimated. For the purposes of model validation p_0 and T_0 are set to the lowest pressure and temperature found in the CFD simulation at the tip of the resonance cavity. In this way the compression cycle predicted by the shock tube model and the CFD simulation can be compared.

For the validation cases, two simulations are run until the mean temperature and pressure inside the cavity reach steady state (when averaged over one flow cycle). The temperature and pressure at the

cavity tip are shown in [Figure B.1](#). The mesh of the resonator is modified to feature a cylindrical cavity with both $D_{tip}/d_{throat} = 1.5$ and $D_{inlet}/d_{throat} = 1.5$. $L/d_{throat} = 10$, with $s/d_{throat} = 3$ and NPR = 6 in both cases. The two validation simulations only differ in upstream total pressure, with one simulated at 10 bar and the other at 14 bar. The upstream total temperature is 293.15 K in both cases.

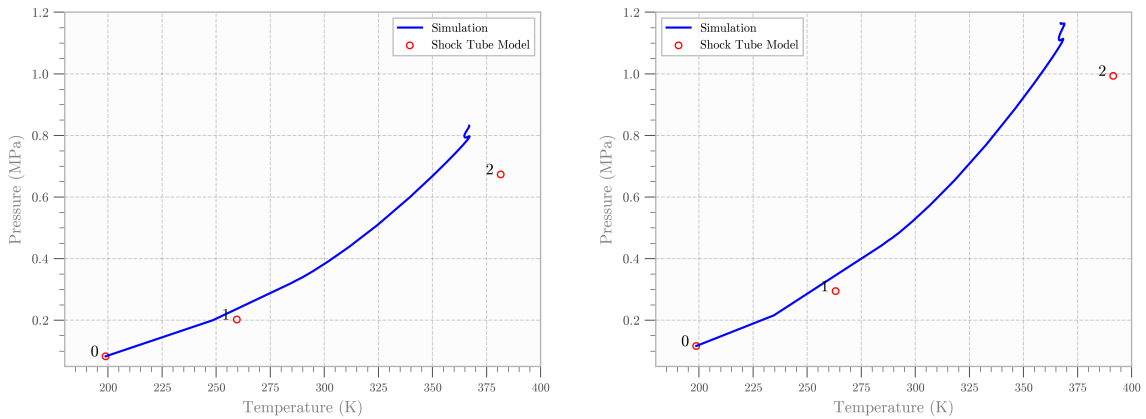


(a) Simulated temperature and pressure at the resonator tip at $s/d_{throat} = 3$, NPR=6 and $p_t = 10$ bar.

(b) Simulated temperature and pressure at the resonator tip at $s/d_{throat} = 3$, NPR=6 and $p_t = 14$ bar.

Figure B.1: Simulation of cylindrical resonance cavity for comparison with shock tube model.

Note that the temperature and pressure rise at the tip of the cavity is significantly lower compared to a conical resonator (as shown in [section D.2](#)). The inflow phase of the simulation is compared to the predicted temperature and pressure rise by the shock tube model in [Figure B.2](#).



(a) Simulated inflow phase and shock tube model at $s/d_{throat} = 3$, NPR=6 and $p_t = 10$ bar.

(b) Simulated inflow phase and shock tube model at $s/d_{throat} = 3$, NPR=6 and $p_t = 14$ bar.

Figure B.2: Validation against 0D shock tube model

In [Figure B.2a](#) and [Figure B.2b](#) point (0) represents the initial state in the cavity, at the start of the inflow phase. Point (1) represents the state of the flow after the first shock wave has reached the cavity tip. At point (2) the reflected shock wave has passed the particle interface. The comparison between the shock tube model and the CFD simulation is somewhat favourable. The simulation predicts a higher final pressure, at a lower final temperature. The lower temperature is likely a result of wall heat transfer, which is not accounted for in the shock tube model. The shock tube model used the simple empirical correlations to determine the mach number in the under-expanded jet and shock wave equations to determine the driving pressure of the incoming shock wave. This introduces additional error that leads to both a difference in the final end-wall pressure, but also the gas temperature, with the latter being

directly related to the initial pressure ratio. Of particular importance for this study is that [Figure B.2a](#) and [Figure B.2b](#) indicate that the first order ROE scheme, used for approximating convective fluxes, compares reasonably well to analytical shock wave relations.

The shock tube model on its own is only useful if given appropriate initial conditions for the state inside the cavity. In this case the initial state is provided by the numerical model. Analytical methods could be used to model the expansion and outflow from the cavity and provide a better estimate of the initial state. Adding the loss models presented in [section 2.4](#) would also improve the presented model.

B.3. Conical Inlet Geometry

A final model validation was carried out using experimental results with the modified, conical, resonator inlet geometry. A front view of the conical resonator is shown in [Figure B.3](#), comparable to [Figure 5.3a](#).

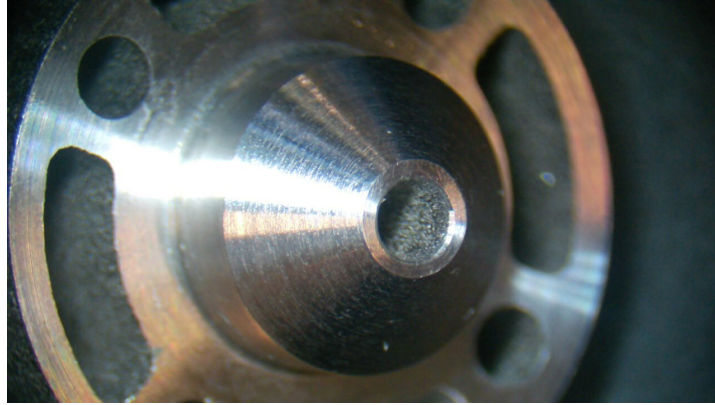
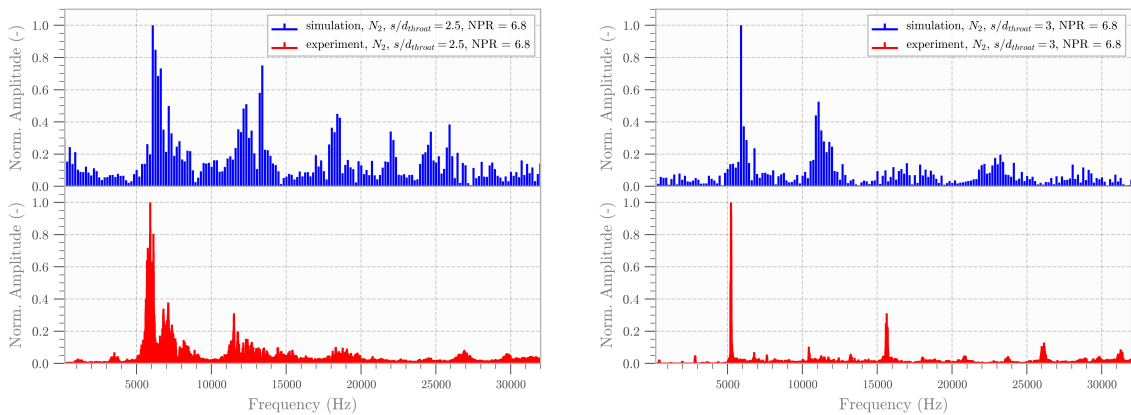


Figure B.3: Front view of resonator with conical inlet under a digital microscope, comparable to [Figure 5.3a](#).

The mesh, shown in [Figure 5.7a](#), is adapted to the conical inlet geometry. Two validation simulations are run for $1.6 \cdot 10^5$ time steps with upstream total temperature and pressure, as well as NPR set to those measured in experiments. The comparison of simulated and experimental spectra are shown in [Figure B.4](#).



(a) Comparison of simulated and experimental spectra at $s/d_{throat} = 2.5$, using nitrogen with a conical resonator inlet. **(b)** Comparison of simulated and experimental spectra at $s/d_{throat} = 3$, using nitrogen with a conical resonator inlet.

Figure B.4: Model validation for a conical resonator inlet.

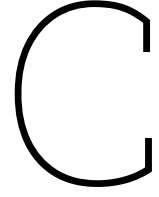
In experiments with the conical resonator inlet, the onset of JRM was found to occur around $s/d_{throat} = 2.5$. The spectrum at this gap spacing is shown in [Figure B.4a](#). Here both the simulation and the

experiment show a clear peak near the first harmonic of the resonance cavity, as well as its first overtone. The spectrum in both cases is noisy compared to those expected in JRM, indicating that at this s/d_{throat} the cavity is experiencing overlapping operating modes. The error between the simulation and experiment is only 2.833%, as shown in [Table B.1](#). The spectra taken for $s/d_{throat} = 3$ show a clear regurgitant mode in [Figure B.4b](#). Here the simulated spectra differs more than in the case of $s/d_{throat} = 3$. It shows the first overtone of the natural frequency very distinctly around 11 kHz, which is barely visible in the experimental spectrum. The second overtone, clearly visible in the experiment, is not clearly present in the simulation. The error in the first harmonic, as predicted by the simulation, is also larger, at 12.9%.

Table B.1: Error in Fundamental Frequency between Simulation and Experiment for Conical Resonator

s/d_{throat}	Experiment (-)	s/d_{throat}	Simulation (-)	Gas	f_0 error (%)
	2.5 ± 0.028		2.5	N_2	2.833 $\begin{smallmatrix} +1.69 \\ -2.56 \end{smallmatrix}$
	3.0 ± 0.028		3.0	N_2	12.9 $\begin{smallmatrix} +1.69 \\ -2.56 \end{smallmatrix}$

Validation of the simulation with a modified inlet geometry shows that it is still capable of predicting the onset of JRM. This indicates that the numerical model presented in [section 5.4](#) can be used for different resonator geometries.



Experimental Results

This appendix includes a selection the remaining experimental data gathered as part of the resonance heating and ignition test campaigns. The method for correcting for thermocouple response time is shown, as well as a derivation for estimating the inner wall temperature of the resonance cavity at steady state. Additional images of the test setup are show.

C.1. Data Acquisition Module

A cRIO from National Instruments provides the ability to actuate the valves individually or as part of an automatic sequence, as well as data logging and live display of pressure data. The solenoid valves will default to the closed position in case of a power loss. This will immediately stop the flow of propellants. An overview of the data acquisition system is shown in [Table C.1](#)

Table C.1: Elements of the Data Acquisition System

Application	Model	Specification
Main DAQ	NI cRIO-9035	CPU, FPGA
Pressure sensor Module	NI 9203	200 kS/s, ± 20 mA
Thermocouple Module	NI 9213	75 S/s Aggregate, ± 78 mV
Dynamic Signal Module	NI 9231	102.4 kS/s/channel

C.2. Thermocouple Response Time Correction

The thermocouple spot welded to the tip of the resonance cavity has a certain response time to a sudden temperature rise due to its own thermal inertia. In order to capture the rise in temperature due to resonance heating accurately, this response time needs to be corrected for. The actual temperature of the cavity wall can be related to the measured temperature by the thermocouple using [Equation C.1](#) [64].

$$T(t) = T_{TC}(t) + \tau \frac{\partial T_{TC}}{\partial t} \quad (\text{C.1})$$

Where T_{TC} represents the temperature measured by the thermocouple. The derivate of temperature with respect to time is calculated numerically using a central difference method. To reduce noise in the thermocouple measurements before taking the derivative, a gaussian filter is applied with a kernel standard deviation of 4. The filtering is only applied when taking the derivative and not for T_{TC} itself. τ is the time constant of the thermocouple and is estimated using [Equation C.2](#).

$$\tau = \frac{m_{TC} \cdot C_{pTC} \cdot t_w}{k_w \cdot A_{TC}} \quad (\text{C.2})$$

Here m_{TC} is the mass of the thermocouple tip in contact with the wall. A_{TC} is the surface area of the thermocouple tip and C_p is the specific heat capacity of the thermocouple material. t_w and k_w are the thickness and thermal conductivity of the wall, respectively. This results in a time constant of $\tau = 0.108$ seconds. [Figure C.1](#) shows the measured and corrected tip temperature for a representative resonance heating test.

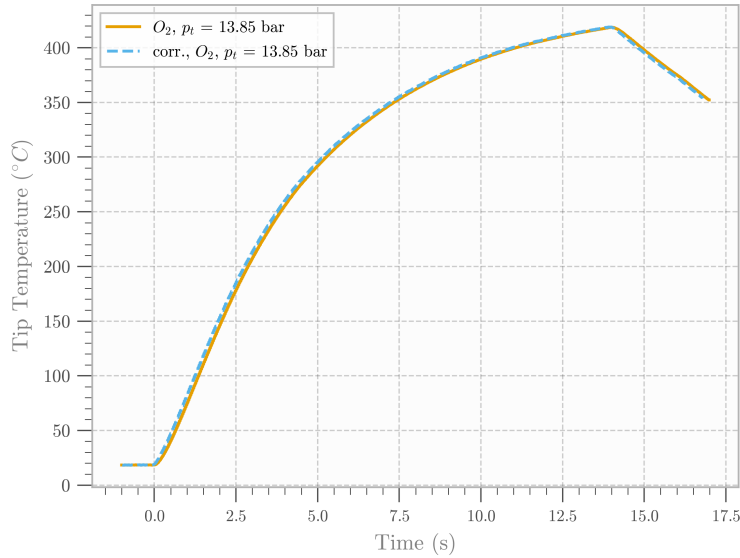


Figure C.1: Measured and corrected tip temperature at $s/d_{throat} = 3$ and NPR = 7.2 for oxygen

Note that the response time correction does not impact the maximum tip temperature (as expected). Instead the impact is most significant at the points where the temperature change is the fastest, such as during the first few seconds of resonance heating.

C.3. Estimating Inner Wall Temperature

The temperature of the inner wall of the resonator can be estimated using the steady state temperature measurement of the outer wall. In steady state, the heat transfer through the resonator tip can be approximated as a thermal resistance circuit. Acoustic heating is fundamentally an unsteady phenomenon, however, due to the slow response time of the cavity wall (as discussed in [subsection 5.4.2](#)), the temperature of the wall reaches a steady state. This means that the heat flux from the resonating gas can be considered constant for a time average over several JRM cycles.

The thermal resistance circuit consists of convective heat flux from the resonating gas into the cavity wall, conduction through the cavity wall and free convection from the cavity wall to the environment. The high temperature difference between the cavity tip and the environment means that radiative heat transfer to the environment cannot be neglected. The presence of an insulating cover over the outside of the resonator almost entirely removes the effect of forced convection to the environment. In steady state the free convection and radiation to the environment must be equal to the conduction through the wall.

$$\dot{Q}_{conv} + \dot{Q}_{rad} = \dot{Q}_{cond} \quad (C.3)$$

Where \dot{Q}_{conv} is the free convection and \dot{Q}_{rad} the radiation to the environment. \dot{Q}_{cond} is the conduction through the cavity wall. The small diameter of the resonator tip means that the conduction is estimated in radial coordinates, according to [Equation C.4](#) [54].

$$\dot{Q}_{cond} = 2\pi kL \frac{T_{w,i} - T_{w,o}}{\ln(r_o/r_i)} \quad (C.4)$$

Where k is the thermal conductivity and L is the length of the cylindrical segment (which eventually cancels out due to ??). $T_{w,i}$ and $T_{w,o}$ are the inner and outer wall temperature. r_i and r_o are the inner and outer radii. The inner diameter of cavity tip is 0.8 mm with a local wall thickness of 1 mm. The linearised radiative heat transfer is estimated using Equation C.5. The thermal conductivity of 17-4 PH stainless steel is taken as 19.5 W/m/K.

$$\dot{Q}_{rad} = \sigma \epsilon 2\pi r_o L (T_{w,o}^4 - T_\infty^4) \quad (C.5)$$

Here, σ is the Stefan-Boltzmann constant, ϵ is the emissivity of the wall material. T_∞ is the ambient temperature. The emissivity of 17-4 PH stainless steel is estimated as 0.51, with an ambient temperature of 288.15 K. The convective heat transfer to the environment is given by Equation C.6.

$$\dot{Q}_{conv} = h 2\pi r_o L (T_{w,o} - T_\infty) \quad (C.6)$$

The convective heat transfer coefficient, h is estimated for free convection according to Equation C.7 [65].

$$h = \frac{k_{air}}{2r_o} \left(0.6 + 0.387 \left(\frac{Ra}{(1 + (0.559/Pr_{air})^{9/16})^{16/9}} \right)^{1/6} \right)^2 \quad (C.7)$$

Where k_{air} is the thermal conductivity and Pr_{air} is the Prandtl number of air, taken from CoolProp [36]. The temperature at which the gas properties are determined is the average between ambient and outer wall temperature. Ra is the Rayleigh number of the air surrounding the cylinder. This leads to a $Ra = 104.6$. Solving the above system of equations at a measured outer wall temperature of 475.28°C leads to an estimated inner wall temperature of 477.1°C. The high heat flux over the very thin resonator wall explains the low temperature difference over the wall.

C.4. Shifting Natural Frequency with Tip Temperature

The rising wall temperature of the resonance cavity also produces a higher average temperature during the JRM cycle as less heat is transferred to the cavity wall. This causes the local speed of sound inside the resonance cavity to increase according to Equation C.8.

$$a = \sqrt{\gamma RT} \quad (C.8)$$

Where γ is the ratio of specific heats of the gas, T is the temperature and R is the specific gas constant. Figure C.2a shows how this causes a shift in the fundamental frequency of the resonance cavity, as well as its overtones. Here a spectrum is taken for every second of resonance heating during a 15 second heating test. Figure C.2b shows f_0 as a function of measured tip temperature. At tip temperatures above 380°C the fundamental frequency begins to drop again slightly. The reason for this slight drop is currently unknown and requires further investigation.

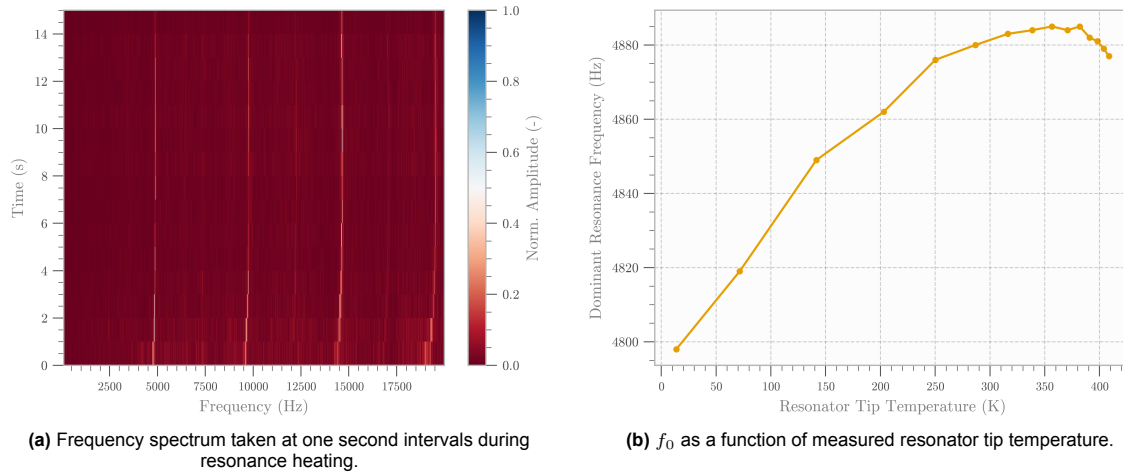


Figure C.2: Time dependent frequency for a 15 second resonance heating test at $s/d_{throat} = 3$ and NPR = 7.2 using oxygen.

C.5. Pressure Measurements During Combustion Tests

Figure C.3 shows the measured pressure during all six combustion experiments. The individual experiments show the variation in upstream pressure of O_2 and CH_4 used to test igniter behaviour at different mixture ratios. The pressure is displayed as a line indicating a moving average, with the surrounding shaded area representing two standard deviations above and below the average. Note that the pressure of methane line is measured upstream of main valve 2; as such it shows a pressure dip as the main valve is opened. The drop in methane pressure when the valve is opened, is a result of using a diaphragm regulator to reduce pressure coming from the gas cylinder. Flow through the regulator causes a reduction in static pressure keeping the diaphragm open, thus resulting in a lower pressure during expulsion compared to the set pressure of the regulator. In all cases the injection of methane causes a rise in chamber pressure, as the exhaust nozzle is already choked during resonance heating in all of these cases. Adding additional inflow, therefore, causes a distinct rise in chamber pressure.

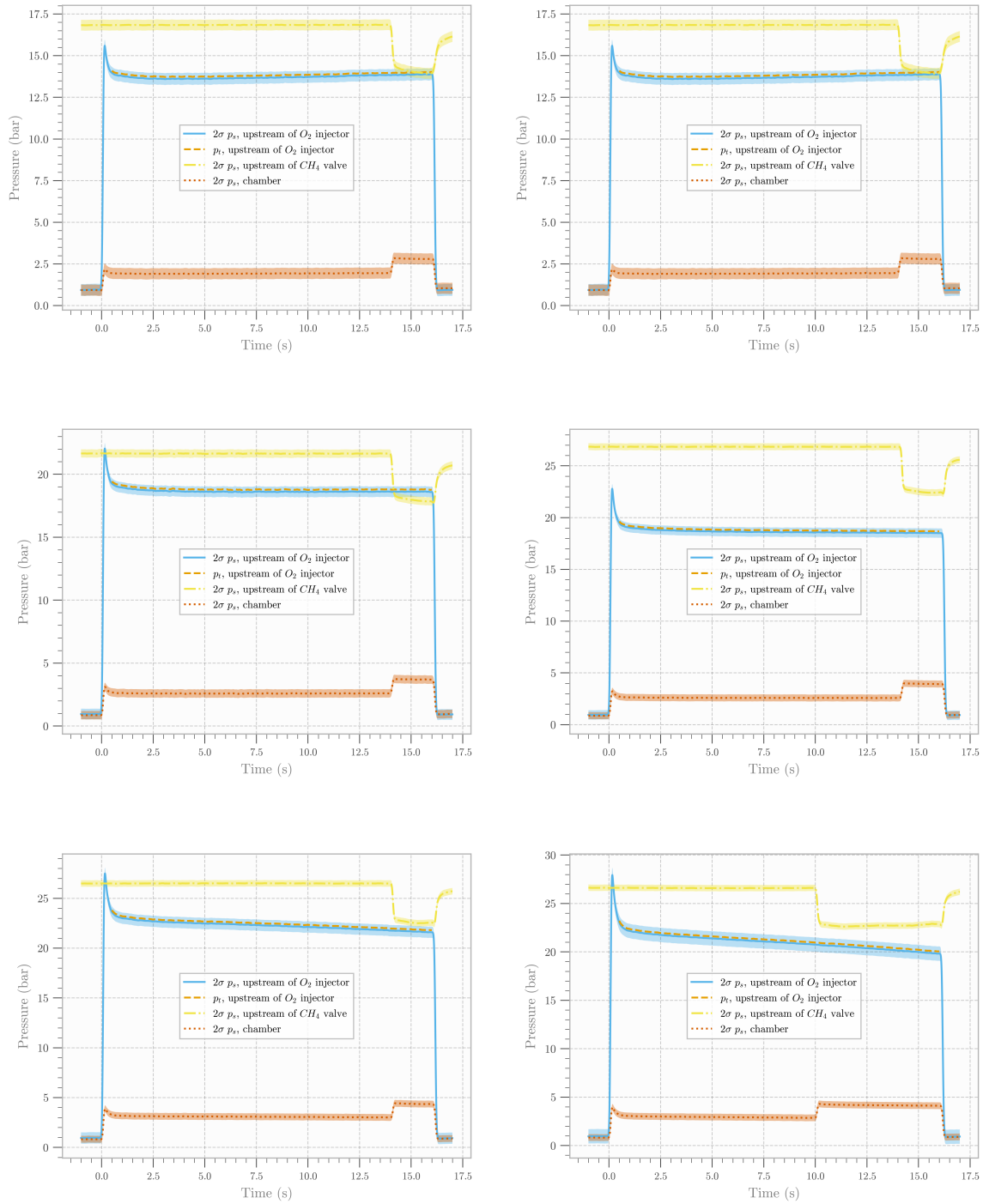


Figure C.3: Filtered oxygen, methane and chamber pressure data for all six combustion experiments.

C.6. Temperature Measurements

The temperature profiles at all tested nozzle gap spacings are shown in Figure C.4. Figure C.4a shows that all tested s/d_{throat} show a similar temperature rise, with the notable exception of $s/d_{throat} = 3.5$. At this point the resonance heating performance decays sharply. The full parameter range of s/d_{throat} was tested using nitrogen. The onset of JRM at $s/d_{throat} = 2$ shows a clear increase in temperature in Figure C.4b.

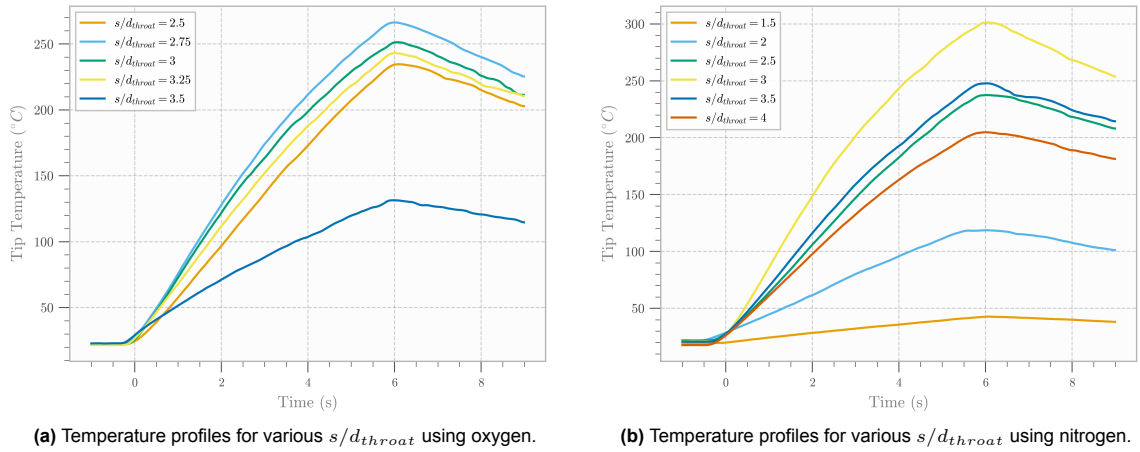


Figure C.4: Temperature profiles for select heating experiments.

C.7. Test Setup and Sensor Placement

This section shows two additional images of the test setup and propellant feed system. [Figure C.5](#) shows a top view of the propellant feed system. The oxygen valve is shown in the lower left corner. The valve for the nitrogen purge is shown in the top right corner. Just below the purge valve is the methane valve. The microphone is placed just to the left of the igniter.

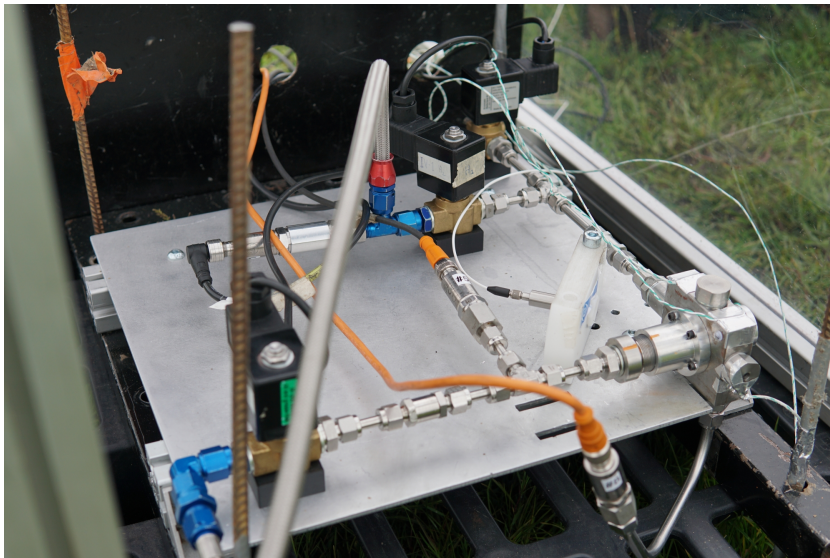


Figure C.5: Top view of the propellant feed system. Note the placement of the microphone to the left of the igniter. Three pressure transducers are visible. The methane PT and oxygen PT are attached directly to their respective propellant lines, with the chamber PT being mounted on a stand-off pipe.

A side view of the feed system, including gas cylinders and data acquisition system are shown in [Figure C.6](#). The oxygen and methane cylinders are seen the lower right of the image, with the nitrogen cylinder on the far left. This image also shows the plexiglass blast shielding placed around the igniter, as well as the steel back plate (discussed in [Appendix F](#)). The data acquisition and valve control system is shown above the nitrogen cylinder.

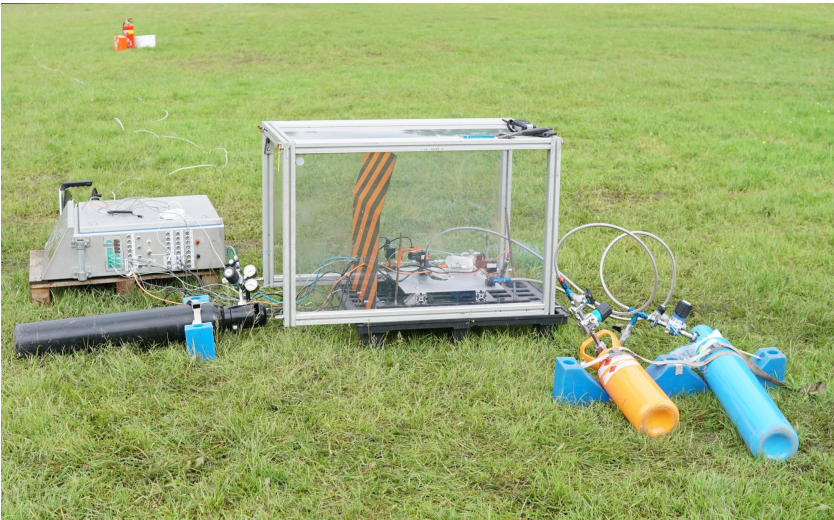


Figure C.6: Overview of the test setup showing the gas cylinders and data acquisition system.

D

Numerical Results

This appendix shows some additional numerical results that are not directly relevant to the main conclusions of the thesis. The mesh quality parameters are presented, as well as a convergence plot of a typical simulation.

D.1. Mesh Parameters and Convergence

The structured mesh, presented in [section 5.4](#), is generated using the Python API of GMSH [67]. It can be refined using a global mesh refinement parameter, which also inversely scales the mesh stretch factor. This means that the proportions between mesh sections remain the same as the number of elements in each section is increased. A summary of some mesh quality parameters is shown in [Table D.1](#) for the nominal number of nodes (100% refinement).

Table D.1: Mesh quality parameters at nominal refinement

Parameter	Minimum Value	Maximum Value
Orthogonality Angle (°)	47.84	90.0
CV Face Area Aspect Ratio	1.0	865.35
CV Sub-Volume Ratio	1.0	11.42

The orthogonality angle of two mesh elements describes angle between the cell face and a line drawn between the two cell centres. Orthogonality close to 90° indicates very good alignment between cells. If the cells are aligned with the mean flow direction, a good alignment between cells produces less numerical diffusion. The use of corner rounding at the nozzle exit and cavity inlet improves the orthogonality significantly. Without the rounding the minimum orthogonality angle drops below 0.15, impacting both simulation stability and accuracy.

The aspect ratio describes the ratio of the width to the height of a cell in a 2D structured grid. The high aspect ratio of some cells occur at the boundary layer elements of the resonance cavity. Here the flow is almost entirely axial, as such the high aspect ratio is less critical if aligned with the mean flow direction. A point of mesh improvement would be to increase the number of cells along the length of the resonator to decrease the aspect ratio of the boundary layer elements.

The volume ratio describes the area ratio of two adjacent cells in the case, of a 2D grid. Values close to 1 are desirable. In this case, the maximum volume ratio occurs at the inlet of the resonator where the rounded inlet transitions into the resonance cavity.

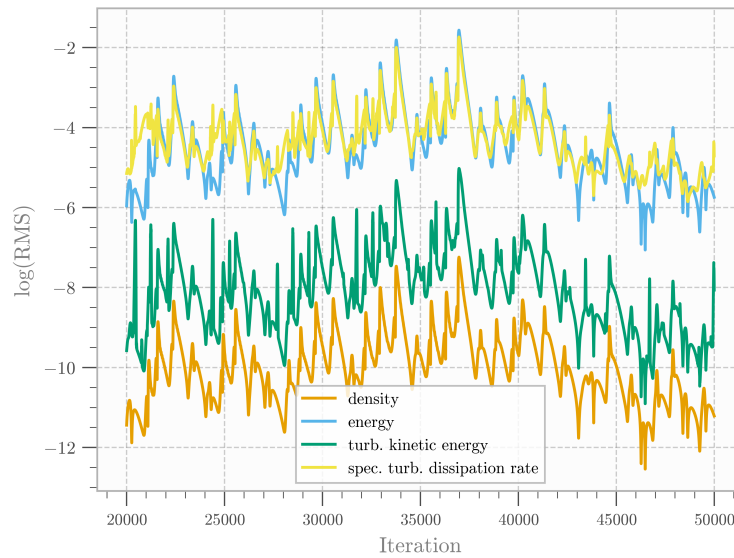


Figure D.1: Residuals of flow and turbulence variables for a simulation of $s/d_{throat} = 2$ and $NPR = 6.8$.

A typical convergence plot for a simulation of a cavity in JRM, using the grid described above, is shown in [Figure D.1](#). The startup transient is not shown as it is neglected from any analysis. The initial conditions of the flow field are set as a uniform temperature and pressure over the entire domain. This results in very high gradients near the inlet and outlet at the start of the simulation and correspondingly high residuals. After two flow cycles the results become usable for analysis.

D.2. Additional Simulation Results

This section presents additional results of one CFD simulation for $s/d_{throat} = 3$ and $NPR = 6.8$, using nitrogen. As with the simulations used for [subsection 5.6.3](#), a startup transient of four JRM cycles (equivalent to 0.8 ms) is removed from the results. [Figure D.2](#) shows the pressure and corresponding FFT at a point along the centre-line of the tip of the resonance cavity near $x/L = 0.99$. This represents the very tip of the cavity while not being within the boundary layer of the cavity tip.

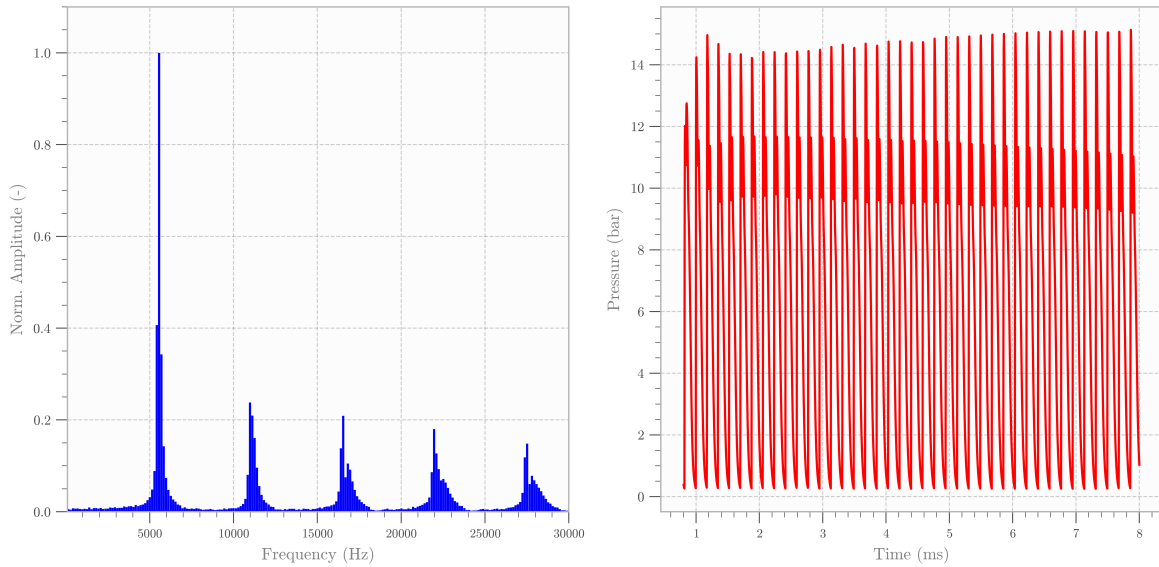


Figure D.2: Pressure and FFT of pressure at the resonator tip for $s/d_{throat} = 3$ and NPR = 6.8.

The pressure profile shows a clear jet regurgitant mode. The total pressure at the inlet of the nozzle is set to 10.2 bar, with the maximum pressure at the cavity tip reaching up to 15 bar. [Figure D.3a](#) shows the temperature at the same location and [Figure D.3b](#) shows the dimensionless wall distance at the resonator wall, very close to the tip.

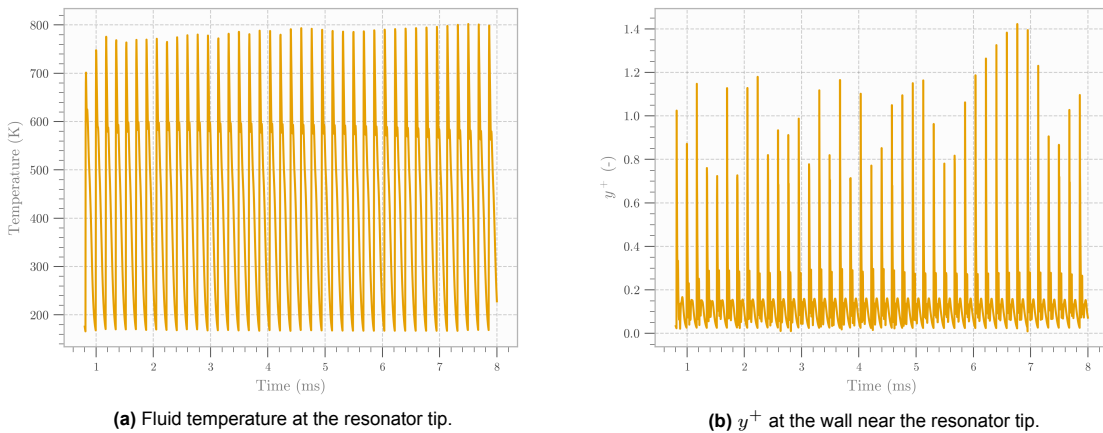


Figure D.3: Temperature and dimensionless wall distance near $x/L = 0.99$ for $s/d_{throat} = 3$ and NPR = 6.8.

The compression in JRM causes gas temperatures up to 800 K in the resonator tip. Over the compression and expansion cycle heat is constantly lost to the isothermal resonator wall. As the wall temperature increases, as seen in experiments, this gas temperature is expected to increase as well. [Figure D.3b](#) shows that average y^+ near the resonator tip remains well below 1 for the majority of the JRM cycle. Only when a shock wave is passing over that wall coordinate does it increase to a maximum of 1.41. [Figure D.2](#) shows the pressure and corresponding FFT at a point along the centre-line of the inlet of the resonance cavity, near $x/L = 0.05$.

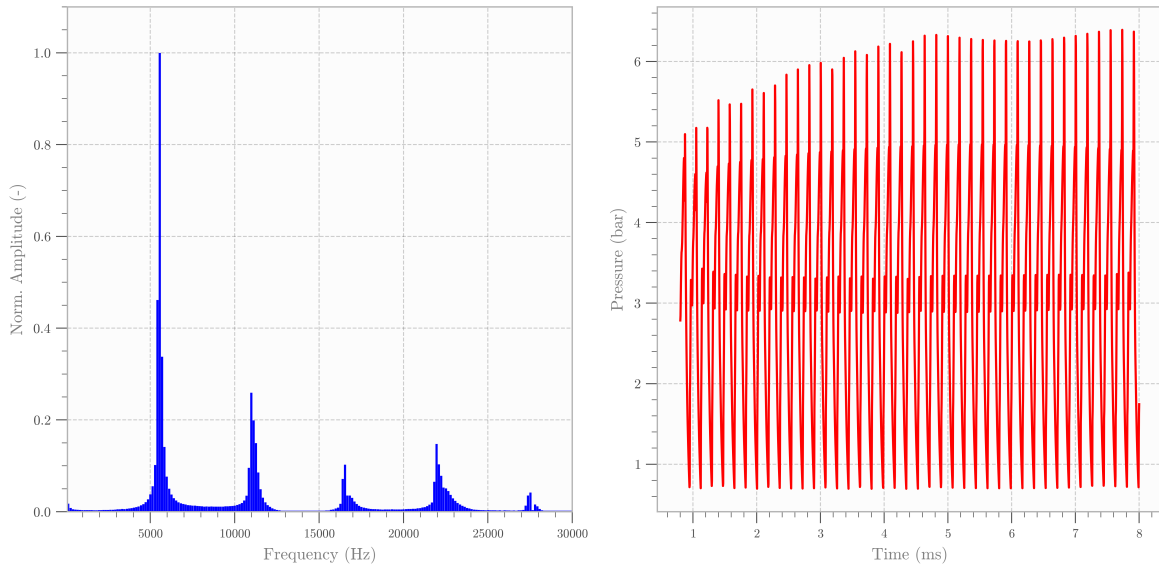


Figure D.4: Pressure and FFT of pressure at the resonator inlet for $s/d_{throat} = 3$ and NPR = 6.8.

The inlet of the cavity sees lower amplitude fluctuations in pressure compared to the tip of the cavity. This is partly a result of using a conical resonator. The frequency of the oscillations remains identical for f_0 and its overtones. The amplitude of these overtones varies slightly between this and [Figure D.2](#). [Figure D.5a](#) shows the temperature at the same inlet location. [Figure D.5b](#) shows y^+ at the wall near the cavity inlet.

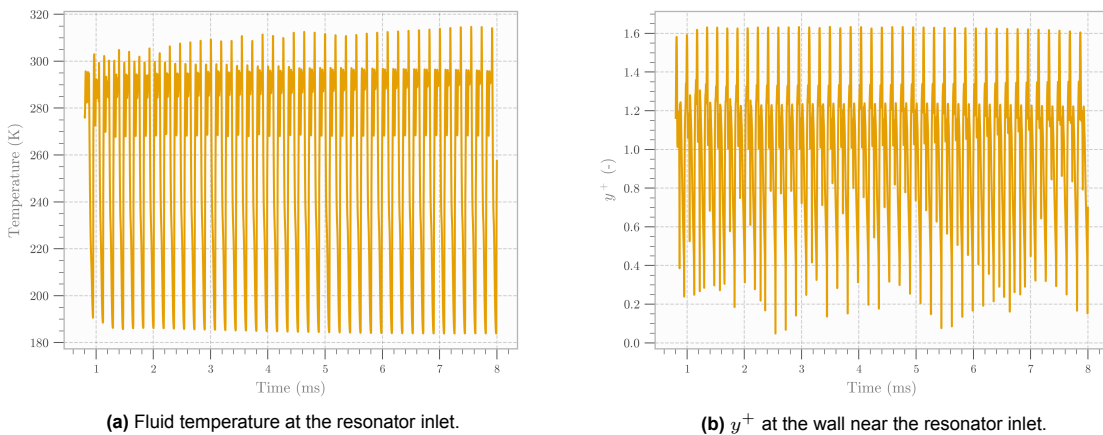


Figure D.5: Temperature and dimensionless wall distance near $x/L = 0.05$ for $s/d_{throat} = 3$ and NPR = 6.8.

The temperature fluctuations at the inlet are also significantly less pronounced than at the tip. Significantly more mixing occurs between the gas inside the cavity and the flow around the inlet, reducing both its temperature and pressure. Here the y^+ is, on average, higher than at the resonator tip, $\bar{y}^+ \approx 1$. This is a result of the mesh in this area having the same number of boundary layer elements as at the tip, but at a larger cavity radius at this location. With the lower flow temperature in this area, it is also less relevant for cavity heat transfer compared to the tip.

D.3. Time Scales for Conjugate Heat Transfer Simulations

The difference between flow and conductive time scales, shown in [subsection 5.4.2](#), pose an inherent challenge for multi-physics simulations of thermo-acoustic resonance. A conjugate simulation of flow

and heat transfer through the resonator wall is necessary to accurately predict both gas and wall temperature at the cavity tip [48]. This means that the heat flux through the wall, as well as the thermal inertia of the wall, need to be modelled. In a fully coupled simulation this would require a simulation resolving several seconds of flow time. Using the time step employed in this study, $\Delta t = 4 \cdot 10^{-8} s$, this results in an order of magnitude of 10^7 time steps. Such a simulation is not only impractical but does not contribute any additional information about the flow field, simulating thousands of nearly identical flow cycles.

A simulation of heat transfer in the cavity wall was not part of this study, however, a method was tested for reducing the computational cost of a conjugate simulation. This method is documented here for future reference and as a suggestion for future work. This is done by artificially reducing the time scale of the heat transfer problem, while maintaining a constant Fourier number and wall heat flux. Such a method will reduce the response time of the wall to the temperature of the fluid. The magnitude of the time scale reduction constitutes a trade-off between accuracy and simulation time.

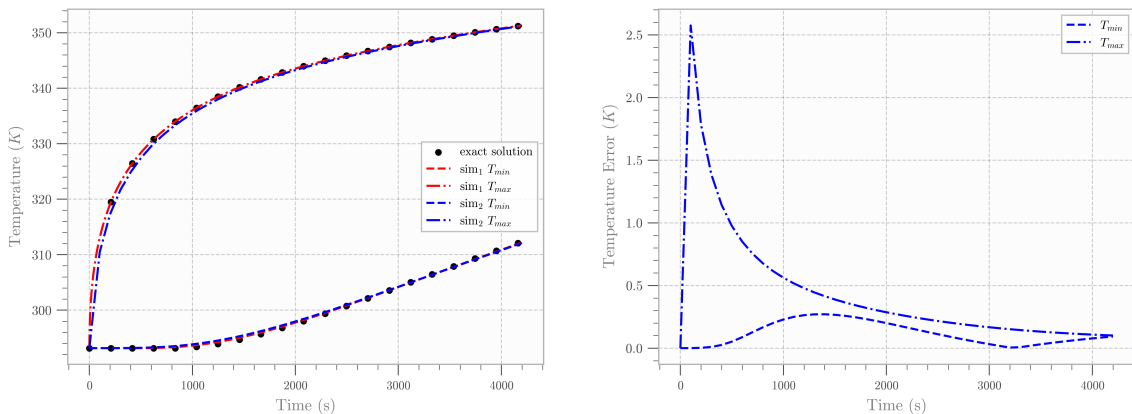
The Fourier number of an unsteady heat transfer problem is shown in Equation D.1. It represents the ratio of time to the time scale of thermal diffusion.

$$Fo = \frac{\alpha t}{L^2} = \frac{kt}{\rho CL^2} \quad (D.1)$$

Where α is the thermal diffusivity, k the thermal conductivity, ρ the density and C the specific heat capacity of the resonator wall. L is a length scale; in this case the the wall thickness of the cavity. In order to maintain a constant Fourier number while reducing the time t by a factor n , either the density or the specific heat capacity need to be divided by the same factor n Shi et al. [68].

$$\frac{k_1 t_1}{\rho_1 C_1 L_1^2} = \frac{k_1 t_2}{\rho_2 C_1 L_1^2} \quad \text{with} \quad t_2 = \frac{t_1}{n} \quad \text{and} \quad \rho_2 = \frac{\rho_1}{n} \quad (D.2)$$

By dividing either the density or the specific heat capacity by the same factor, the heat flux into the wall also remains constant. An example of the effect of this method is shown in Figure D.6. Here a time dependent one dimensional heat transfer problem from Mills [54, p.208] is solved using a second order central finite difference scheme. One simulation is run using the original material parameters and the other using a reduction factor n of 100.



(a) Finite difference solution to a sample heat transfer problem from Mills [54, p.208]. Sim₁ represents the baseline simulation and Sim₂ the same simulation, but with the time scale reduced by a factor of $n = 100$. The time dependent temperature profile from Sim₂ is scaled to the time axis of Sim₁ for better comparison.

(b) Error between Sim₁ and Sim₂ in Figure D.6a

Figure D.6: Example of reduction in conductive time scale while maintaining a constant Fourier number.

Both simulations are discretised in time using an implicit Backward Euler method. The baseline simulation, Sim_1 , is run for 4200 time steps. The reduced time scale simulation, Sim_2 , is run for 42 time steps. Sim_2 is scaled back to the time axis of Sim_1 for comparative purposes in [Figure D.6a](#). Here the results of both simulations are very similar, with any difference being a result of increased numerical error in the time discretisation at the reduced time scale, shown in [Figure D.6b](#).

E

Manufacturing and Technical Drawings

This appendix explains the manufacturing steps taken to ensure the critical alignment between the oxygen injector and the resonator. Technical drawings are shown detailing the igniter assembly. Part drawings are shown for all components, including the post machining of the SLM printed resonator. All other components were manufactured by the author on a manual mill and lathe.

E.1. Critical Dimensions and Manufacturing Tolerance

Some steps in the manufacturing process and operation of the igniter are identified as critical for the repeatability of the results of this study. The nozzle gap spacing is adjusted using an M24x1.0 screw thread. This allows for changing s/d_{throat} in between heating tests with only minor adjustment of the test setup. The use of metric fine pitch threads allows for some backlash between the oxygen injector and the injector support. As a result, gauge pins are used while setting the nozzle gap spacing to confirm the correct s/d_{throat} . The gauge pins can be inserted into the chamber by removing the exhaust nozzle.



Figure E.1: Machining the bore that interfaces with both the oxygen injector and the resonator.

The most important alignment tolerance of the assembly is between the oxygen injector and the inlet to the resonance cavity. Alignment between these two parts has a direct impact on the symmetry of

the pressure field upstream of the resonator inlet. The combustion chamber is used to align both parts. A 12 mm bore in the centre of the chamber interacts with the resonator on one side and the oxygen injector on the other. The alignment of these two parts is ensured by mandating a tolerance on the diameters of the injector and resonator that ensure a close fit with the bore in the chamber. The bore inside the chamber is machined with an H7 tolerance using a reamer. This is shown in [Figure E.1](#). The perpendicularity of the bore with respect to the igniter body is ensured using a dial indicator mounted in the mill spindle.

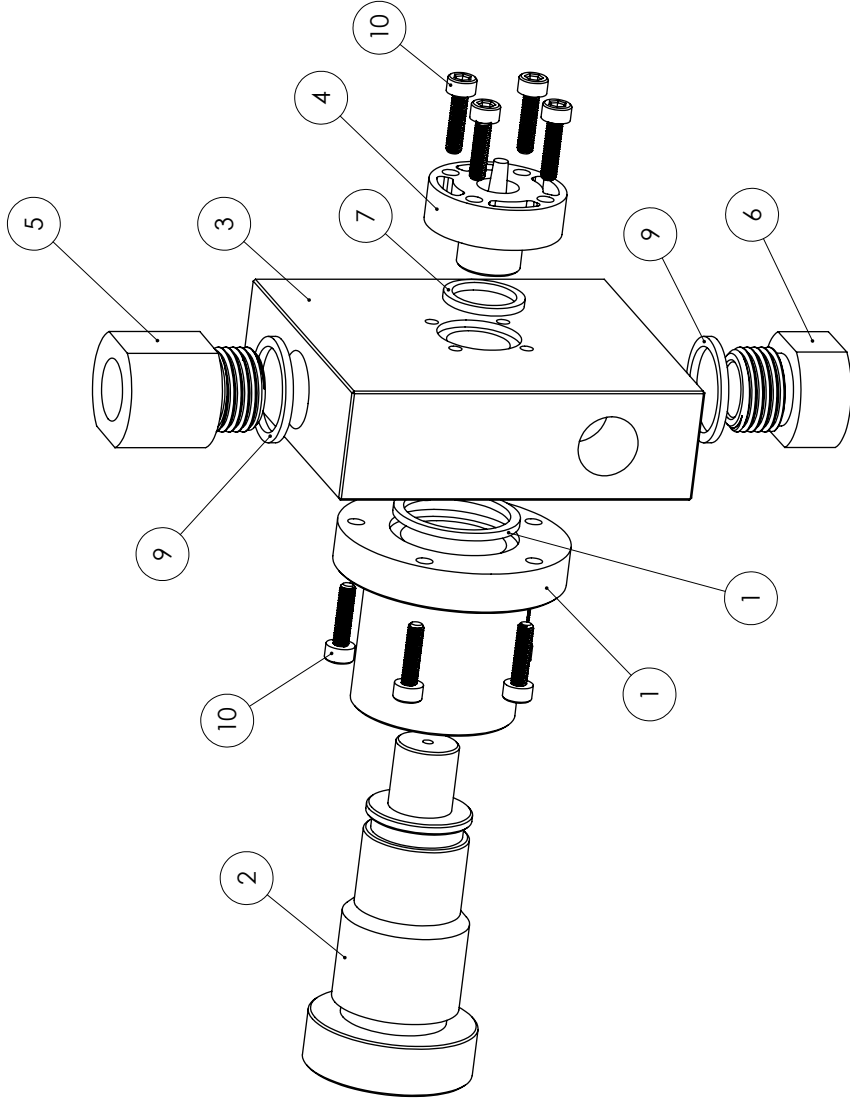
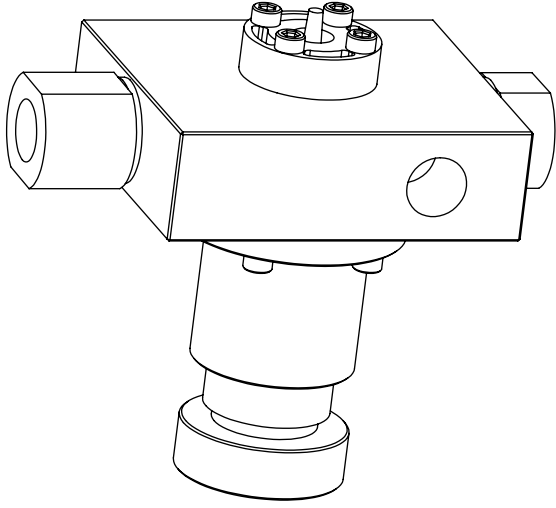


Figure E.2: Measuring concentricity between the cavity inlet and the interface between the resonator and combustion chamber using a small dial indicator.

Another important step in ensuring the alignment between the inlet of the resonance cavity and the under expanded jet is the concentricity of the cavity inlet. The 3D printed resonator is mounted in a collet with a small dial indicator placed inside the cavity inlet. This shows how concentric the resonance cavity is to the spindle of the lathe, and is critical to ensure before post-machining the interface with the combustion chamber. This is shown in [Figure E.2](#).

E.2. Drawings

The first drawing shows an exploded view of the igniter assembly, including a bill of materials. The assembly process is outlined as part of the second drawing. This includes multiple section views of the assembly and the area around the resonator and oxygen injector. The remaining technical drawings show the individual igniter components, starting with the combustion chamber, followed by the methane injector, exhaust nozzle, oxygen injector and injector support. Finally a drawing is shown for post-machining operations for the SLM printed resonator tip.



ITEM NO.	PART NAME	QTY.
1	Oxygen Injector Support	1
2	Oxygen Injector	1
3	Combustion Chamber	1
4	Resonance Chamber	1
5	Methane Injector	1
6	Exhaust Nozzle	1
7	Resonator Gasket	1
8	Oxygen Injector Gasket	1
9	Nozzle Gasket	2
10	M3x12 Bolt Grade 8.8	9

ALL DIMENSIONS IN mm
UNLESS OTHERWISE NOTED

TOLERANCES

LINEAR: .XX ± 0.05
ANGULAR: X ± 1°

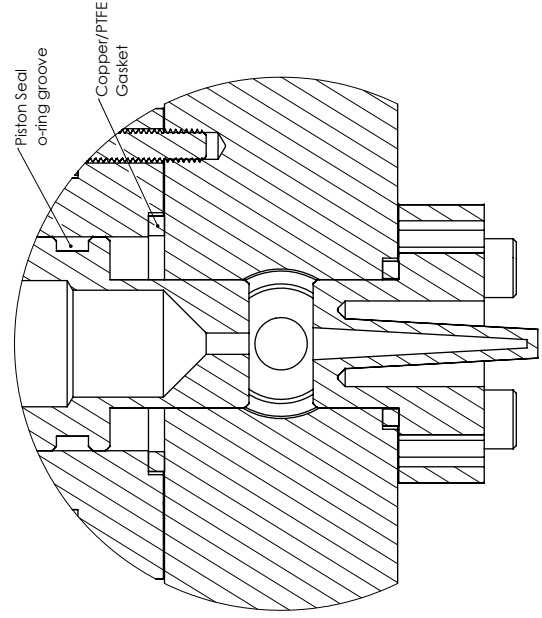
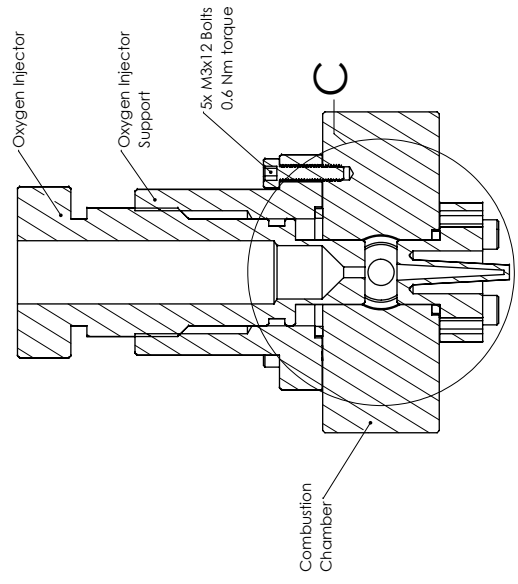
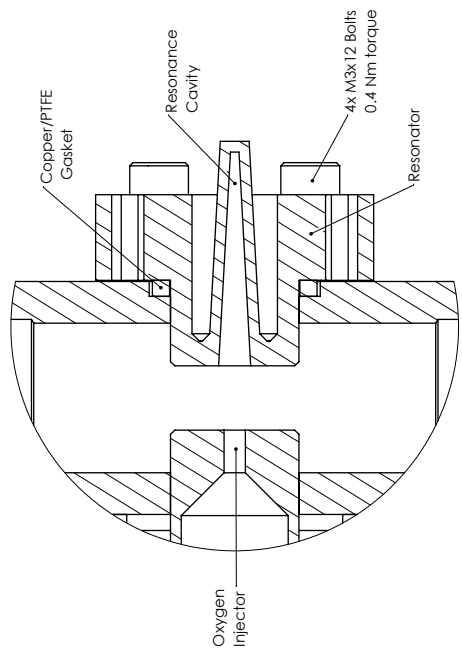
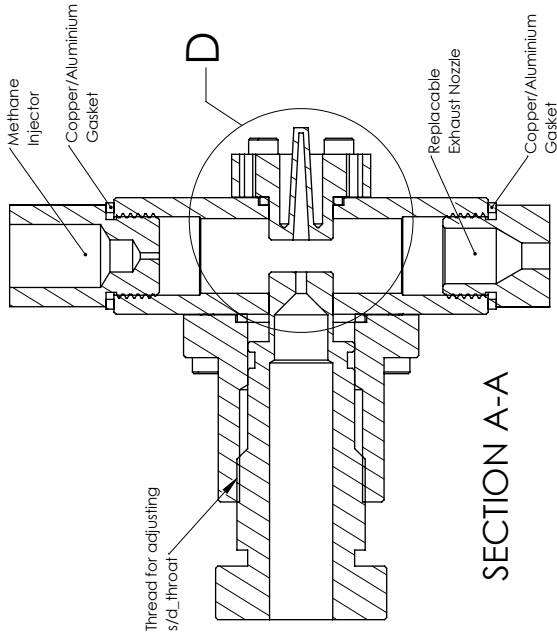
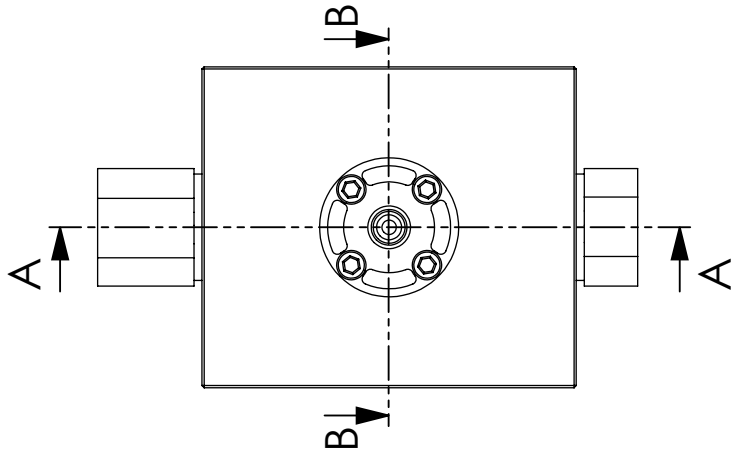


ASSEMBLY: Resonance Igniter

AUTHOR: Jonathan Neeser

VERSION: 1.1

SHEET: 1 OF 1



Assembly Instructions

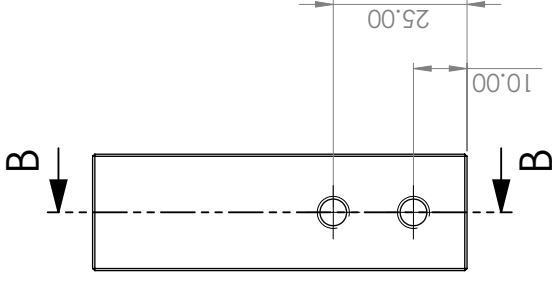
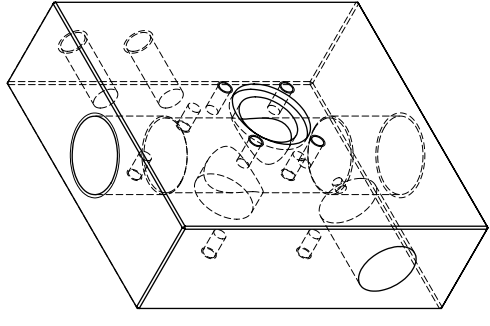
1. Apply Krytox to the piston seal o-ring and insert it onto the oxygen injector
2. Apply a small amount of bearing grease (or Krytox) to the thread on the oxygen injector
3. Insert the oxygen injector into the injector support until the thread engages and turn another two revolutions
4. Apply Krytox to the copper or PTFE gasket for the injector support. Mount the injector and support peice to the chamber using 5 M3 bolts
5. Apply Krytox to the copper or PTFE gasket for the resonator. Mount the resonator to the chamber using 4 M3 bolts
6. Mount the methane injector to the chamber with a copper or aluminium gasket
7. Using the screw thread on the oxygen injector, set the desired nozzle gap spacing and measure it with a gauge pin
8. Mount the nozzle to the chamber with a copper or aluminium gasket
9. **NOT SHOWN HERE:** Mount chamber pressure sensor and stand-off pipe to the chamber
10. **NOT SHOWN HERE:** Mount igniter assembly to test bench

ALL DIMENSIONS IN mm UNLESS OTHERWISE NOTED	
TOLERANCES	
LINEAR: XX ± 0.05	ANGULAR: X ± 1°

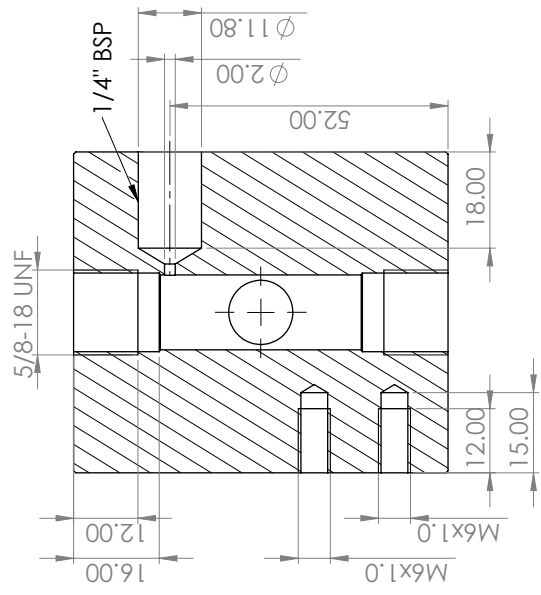
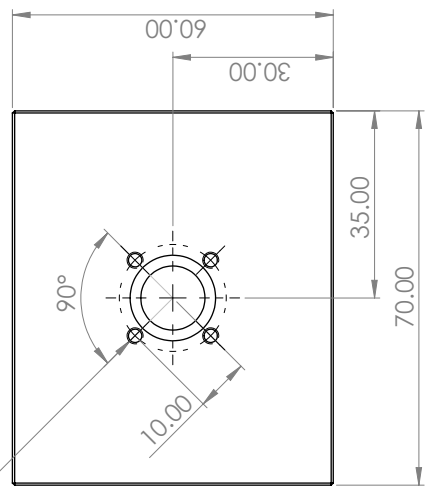
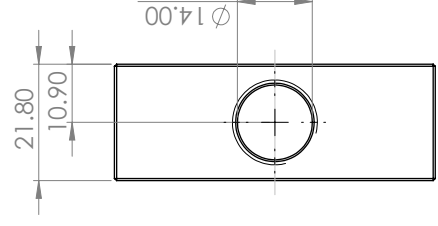
Resonance Igniter Assembly Drawing

AUTHOR: Jonathan Neeser
VERSION: 1.0

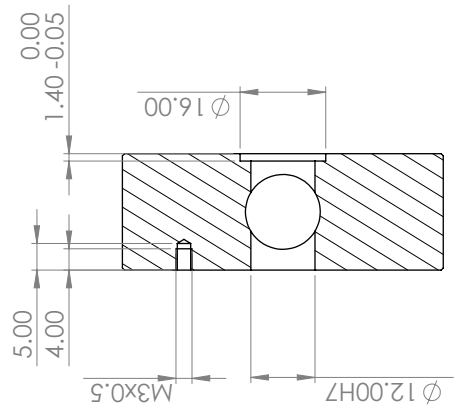




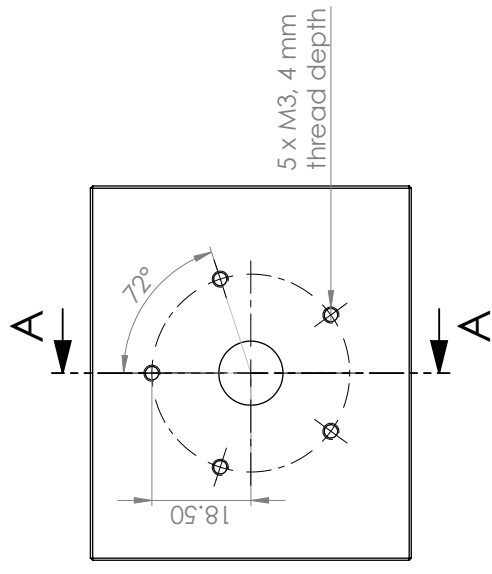
4 x M3, 5 mm thread depth



SECTION B-B



SECTION A-A



ALL DIMENSIONS IN mm UNLESS OTHERWISE NOTED	
TOLERANCES	
LINEAR: XX ± 0.05	ANGULAR: X ± 1°

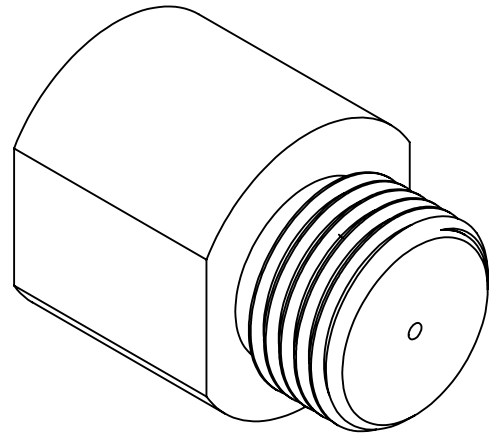
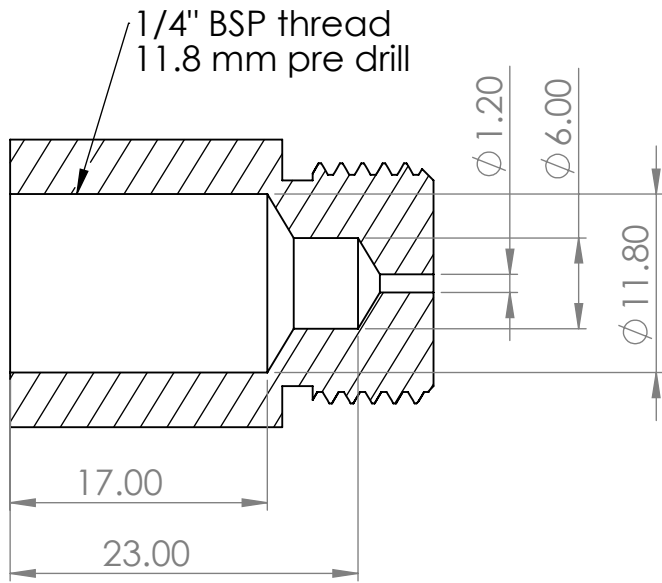
PART: Combustion Chamber

AUTHOR: Jonathan Neeser

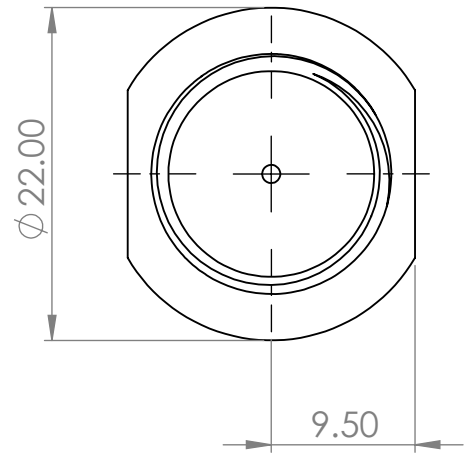
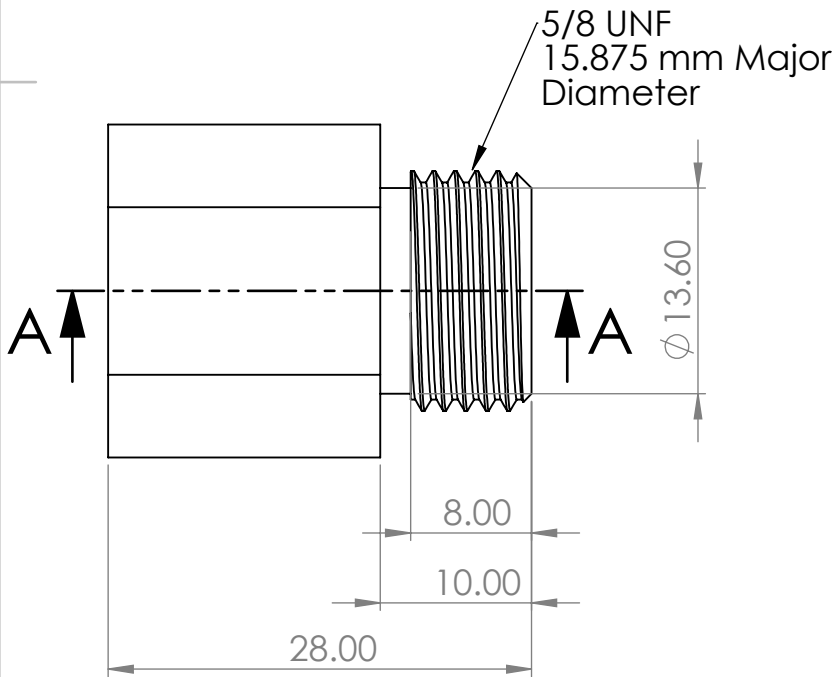
VERSION: 1.1

MATERIAL: Stainless Steel 1.4305 SHEET: 1 OF 1





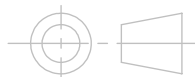
SECTION A-A



ALL DIMENSIONS IN mm
UNLESS OTHERWISE NOTED

TOLERANCES

LINEAR: .XX \pm 0.05
ANGULAR: X \pm 1°



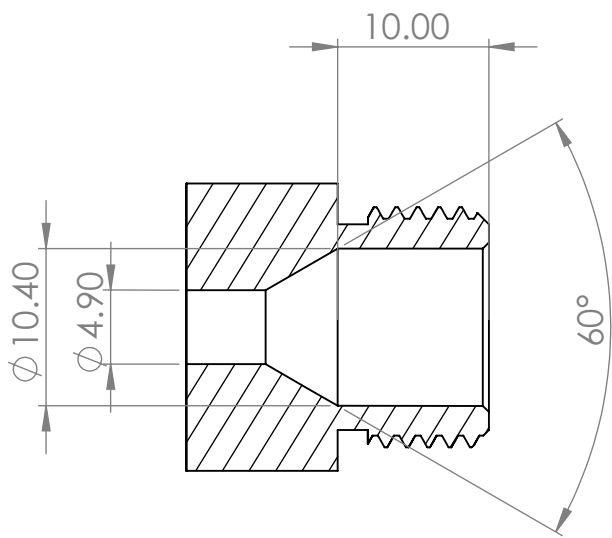
PART: Methane Injector

AUTHOR: Jonathan Neeser

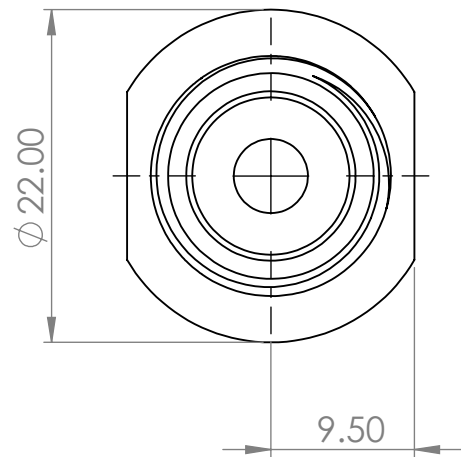
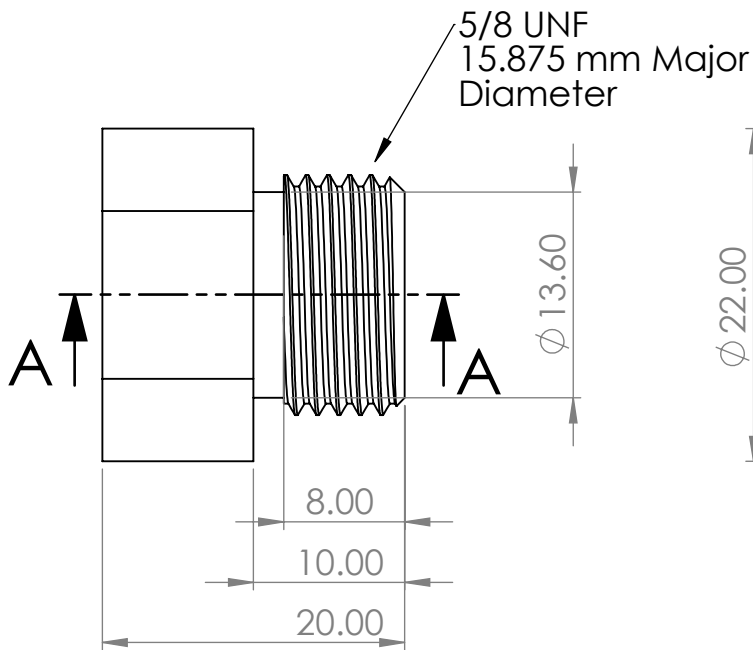
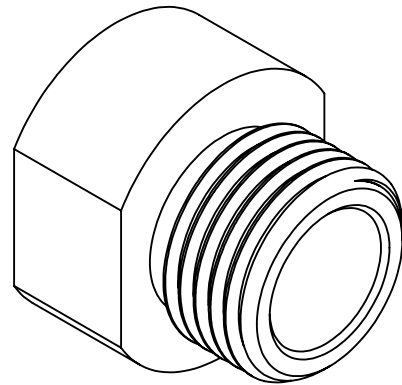
VERSION: 1.3

MATERIAL: Stainless Steel 1.4305

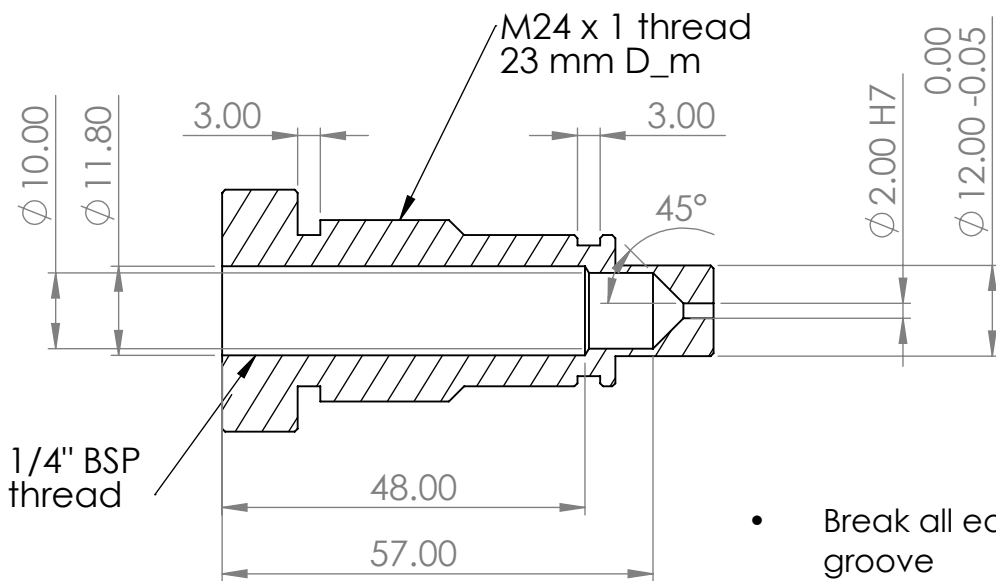
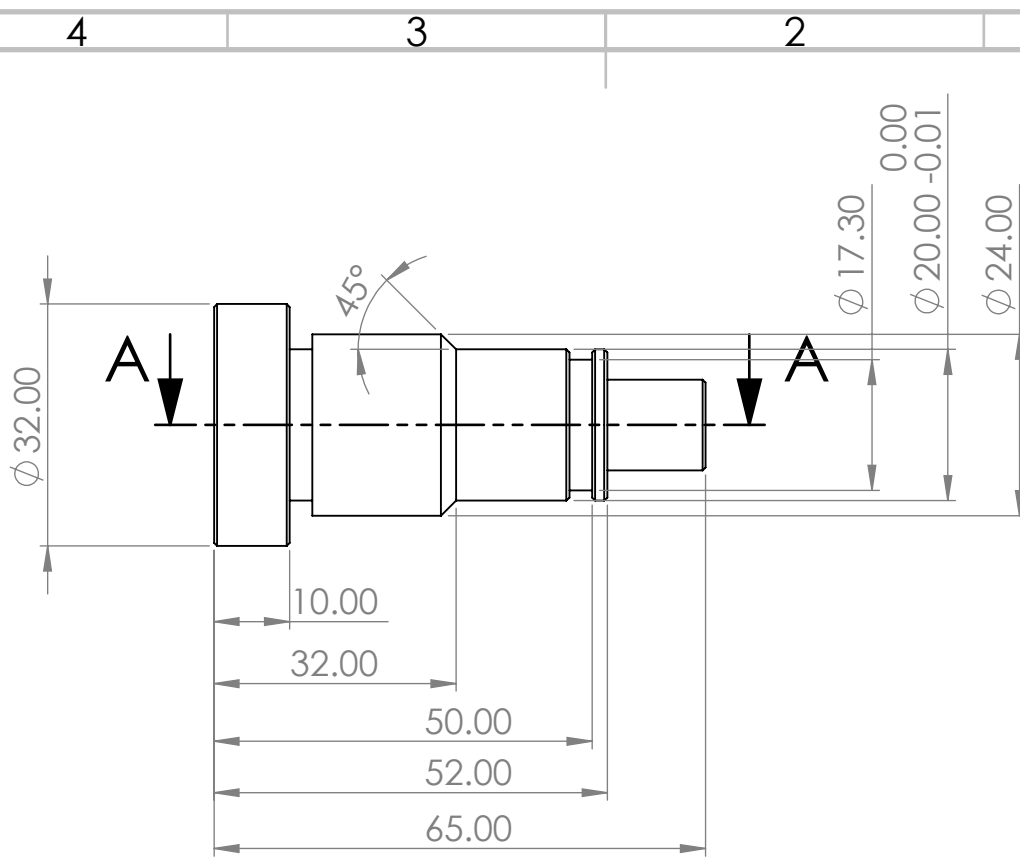
SHEET: 1 OF 1



SECTION A-A



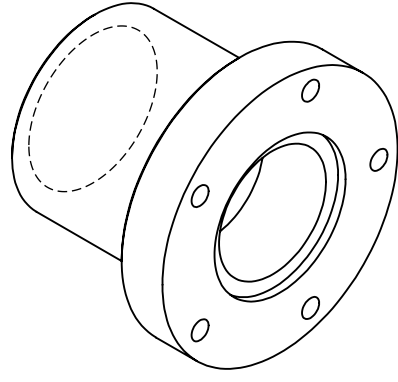
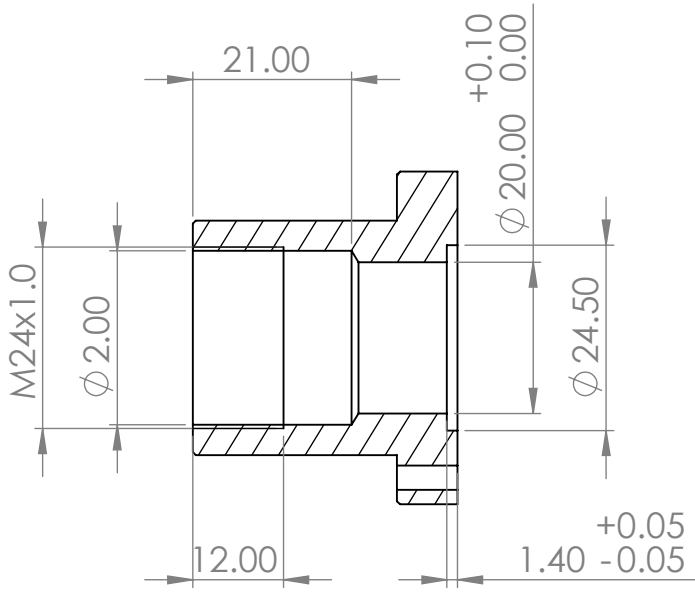
ALL DIMENSIONS IN mm UNLESS OTHERWISE NOTED		PART: Exhaust Nozzle	
TOLERANCES		AUTHOR: Jonathan Neeser	
LINEAR: .XX ± 0.05	ANGULAR: X ± 1°	VERSION: 1.1	
		MATERIAL: Stainless Steel 1.4305	
		SHEET: 1 OF 1	



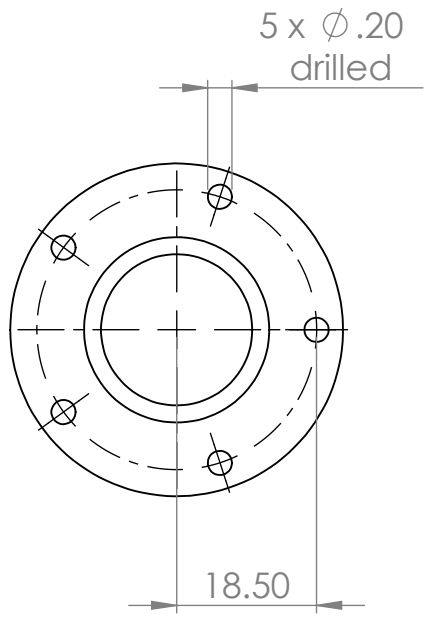
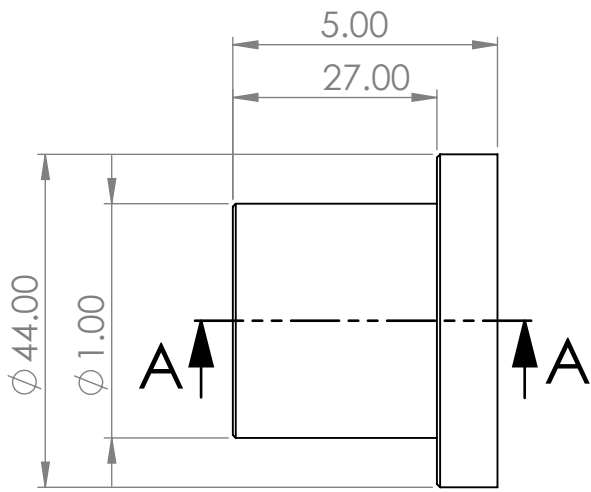
SECTION A-A

- Break all edges at the o-ring groove
- Use reamer for 2mm throat
- Use long 45 deg. chamfer mill to form converging section of the inlet

ALL DIMENSIONS IN mm UNLESS OTHERWISE NOTED		PART: Oxygen Injector	
TOLERANCES			
LINEAR: .XX ± 0.05	ANGULAR: X ± 1°	AUTHOR: Jonathan Neeser	
		VERSION: 1.0	
		MATERIAL: Stainless Steel 1.4305	SHEET: 1 OF 1



SECTION A-A

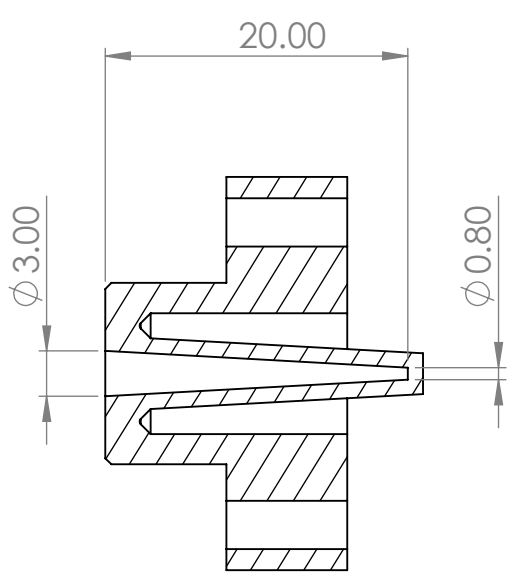


ALL DIMENSIONS IN mm UNLESS OTHERWISE NOTED		PART: Oxygen Injector Support	
TOLERANCES			
LINEAR: .XX ± 0.05	ANGULAR: X ± 1°	AUTHOR: Jonathan Neeser	
		VERSION: 1.2	
		MATERIAL: Al 7075 T6	SHEET: 1 OF 1

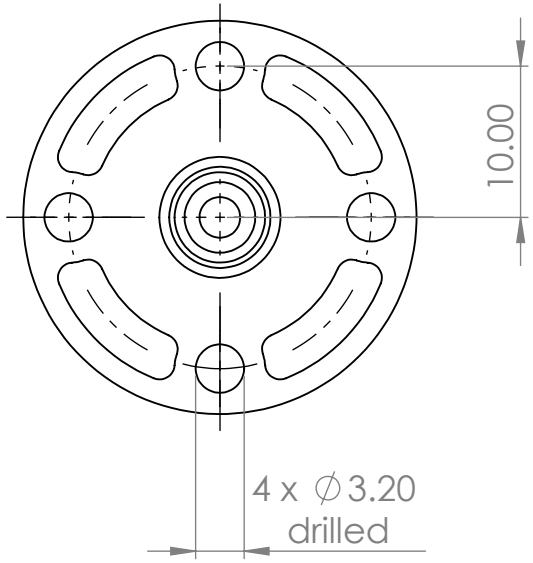
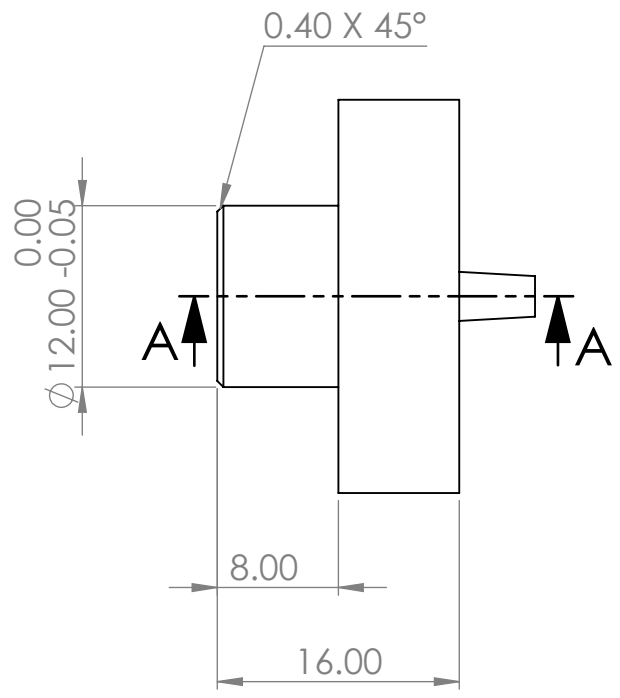
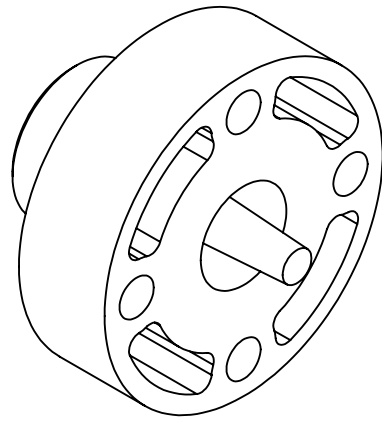
4 3 2 1

F
E
D
C
B
A

F
E
D
C
B
A



SECTION A-A



ALL DIMENSIONS IN mm UNLESS OTHERWISE NOTED		PART: Resonance Chamber	
TOLERANCES			
LINEAR: .XX ± 0.05	ANGULAR: X ± 1°	AUTHOR: Jonathan Neeser	
		VERSION: 1.1	
		MATERIAL: 17-4 PH	SHEET: 1 OF 1

2 1

F

Risk Assessment

This appendix shows some key aspects of the operational and design safety of the resonance igniter test setup. These are outlined specifically for the combustion experiments but broadly apply to the heating tests as well, especially when using oxygen as the driving gas. The design failure modes of the igniter are presented, along with the blast shielding required for the test setup. The full risk maps associated with combustion tests are shown, which form the basis of the operational safety measures implemented in the test procedures, shown in [Appendix G](#).

F.1. Igniter Design and Safety

An overview of the expected failure modes and the pressures at which they occur is shown in [Table F.1](#). These represent the most likely points of failure of the design. Tensile failure of the resonator or the oxygen injector is desirable as this causes shrapnel to be ejected in a predictable direction. The effect of which can be mitigated using blast shielding. A radial burst of the combustion chamber is to be avoided as this could cause the release of shrapnel in multiple directions and is considered significantly less predictable.

Table F.1: Igniter Failure Modes

Failure Mode	Pressure (MPa)	Safety Factor
Tensile bolt failure of oxygen injector	23.67	12.94
Tensile bolt failure of resonator	84.71	52.08
Combustion chamber burst	118.57	84.69

The safety factor is determined from the nominal combustion chamber pressure of 1.8 MPa. The tensile failure modes of the oxygen injector and the resonator describe the tensile failure of the M3 bolts that attach these parts to the combustion chamber. Here the failure pressure is calculated from the yield strength of the bolts, taking into account the pre-tensioning required to compress the aluminium sealing rings (present at the interface of both parts with the combustion chamber). The failure pressure can then be described using [Equation F.1](#).

$$p_{failure} = \frac{\sigma_y \cdot A_b \cdot n - F_c}{A} \quad (F.1)$$

Where σ_y is the yield strength of the bolts, A_b is the bolt cross sectional area, A is the area the chamber pressure is acting on, n is the number of bolts and F_c is the required pre-tension force on the seal. M3 bolts at grade 8.8 have a minimum proof load of 2920 N¹. For the resonator the compressive force

¹Proof load of grade 8.8 M3 bolts (last accessed 25.08.2024): https://www.engineeringtoolbox.com/metric-bolts-minimum-ultimate-tensile-proof-loads-d_2026.html

required for the seal is 2100 N and it is attached using four M3 bolts. The area on which pressure acts (1.13 cm^2) is the cross sectional area around the resonator inlet, in addition to the inlet area resonator. This results in a safety factor of 52.08.

The oxygen injector support features five bolts and a required seal compression force of 3890 N. The area on which pressure acts is the cross sectional area around the oxygen injector, 4.52 cm^2 . This results in a safety factor of 12.94. The burst pressure of the combustion chamber is estimated using the minimum wall thickness of the combustion chamber and basic cylindrical hoop stress.

$$p_{failure} = \frac{\sigma_y \cdot 2 \cdot t}{D} \quad (\text{F.2})$$

Where t is the minimum wall thickness, 2 mm, and D the internal diameter of the combustion chamber, 14 mm. With a yield strength of 1.4305 stainless steel of 415 MPa ², this results in a burst pressure of 118.57 MPa and a safety factor of 84.69. This value is likely optimistic, as the cylinder features several openings that act as locations of stress concentrations. However, the safety factor of a radial burst is deemed sufficiently above that of the other failure modes.

The order of failure modes means that radial ejection of shrapnel is unlikely. Despite this, blast shielding in the form of plexiglass and steel plates is added around the test setup to cover lines of sight to testing personnel. An overview of the experimental setup is shown in Figure F.1. It shows the placement of the igniter relative to the blast shielding, gas cylinders and data acquisition system.

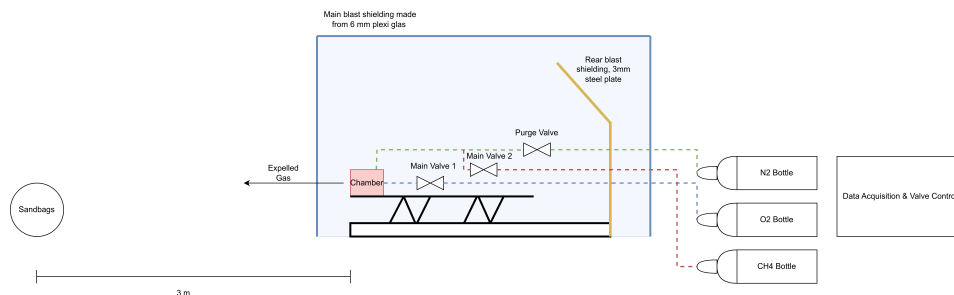


Figure F.1: Diagram of side view of the test setup including blast shielding, gas cylinders and data acquisition system. Note that the plexiglass shielding covers all lines of sight to the test setup.

F.2. Risk Maps

This section shows the risk maps associated with testing an acoustic resonance igniter on the TU Delft campus. Each risk is given a score of severity and probability of it occurring. The impact of any given risk is a combination of its severity and likelihood. The mitigation strategies are aimed at reducing either severity or probability. Reducing either, or both, can be sufficient to bring the risk to an acceptable level. The categories of severity are shown in Table F.2. The acceptable area of the risk map is denoted by the fields shaded in green.

²Mechanical properties of 1.4305 stainless steel (last accessed 25.08.2024): <https://asm.matweb.com/search/SpecificMaterial.asp?bassnum=MQ303H>

Table F.2: Severity Categories for Risk Maps

Score	Severity	Explanation
A	Insignificant damage to property	Insignificant damage: Damage caused does not impact the continuation of the test or the functioning of the system in any way, or damage that can be fixed at the test site
B	Non-reportable injury to personnel or significant damage to property	Non-reportable injury: Anything that requires minor first aid treatment (scratches, bruises etc.) Significant Damage: Damage that impacts the performance of the system but can be fixed after the test.
C	Reportable injury to personnel or severe damage to property	Reportable Injury: Anything requiring first aid but not calling emergency services (fractures, major sprains, small burns, minor wounds etc.) Severe Damage: Damage to the test setup that prevents all further testing and requires a major rebuild of the system.
D	Major injury or possible fatalities, extreme damage to property	Major injury: calling emergency services Extreme damage: Damage that goes beyond the system (major damage to the test site)

[Table F.3](#) assigns a score to the estimated probability of a single event occurring. The probability assigned to any risk needs to be understood as an estimate, based on experience with similar systems and conjecture.

Table F.3: Severity Categories for Risk Maps

Score	Likelihood	Defined Probability
5	Almost certain	approximately 1:5
4	Will probably occur	approximately 1:20
3	Will possibly occur	approximately 1:100
2	Remotely possible	approximately 1:1000
1	Extremely unlikely	approximately 1:10000

It is also important to note that while determining the likelihood and severity of the risks, a standard level of safe operations is assumed. This includes measures that can be found on all tests conducted by DARE, such as the use of safety glasses when near a pressurised system, and minimum safety distances between personnel and an active test setup. This assessment assumes the presence of a test operator with experience with pressurised systems and rocket engine tests. It is further assumed that during resonance heating and firing operations, all personnel are at least 20m away from the test setup.

RISK MAP BEFORE MITIGATION					
		Insignificant damage to property or no injury to personnel	Non-reportable injury or significant damage to property	Reportable injury or severe damage to property	Major injury or possible fatalities or extreme damage to property
		A	B	C	D
Almost Certain	5				
Will Probably Occur	4		R10	R1, R4, R6	
Will Possibly Occur	3		R3, R5	R2, R7, R8, R9	
Remotely Possible	2				
Extremely Unlikely	1				

RISK MAP AFTER MITIGATION					
		Insignificant damage to property or no injury to personnel	Non-reportable injury or significant damage to property	Reportable injury or severe damage to property	Major injury or possible fatalities or extreme damage to property
		A	B	C	D
Almost Certain	5				
Will Probably Occur	4				
Will Possibly Occur	3	R5	R4, R9		
Remotely Possible	2	R3	R1, R2, R8, R10		
Extremely Unlikely	1		R7	R6	

RISK ID	EVENT	EXPLANATION	CATEGORY	MITIGATION	Pre-mitigation	Post-mitigation
R1	Oxygen Leak leading to secondary fires on the test setup or Fellowship Field	Leak in the oxygen feed system as a result of a damaged connector or improper assembly. Such leaks can be dangerous to personnel near the test setup. Oxygen leaking also significantly increases the risk of fire due to electric arcing.	Probability	Each feed system connection is visually inspected for damage or anomalies before the test begins. The feed system is tested for leaks under operational pressure on fellowship field on the day of the test.	4	2
			Severity	Type ABC fire extinguisher and a water bucket are present on the field during testing	C	B
R2	Loss of Connection to the Valve Control System	A loss of connection results in all valves remaining in the state set before the loss of connection occurred. If a valve is open, it will remain open, potentially venting gas	Probability	The LabVIEW software controlling the valves is extensively validated before the test day.	3	2
			Severity	The main valve and purge valve are normally closed. In case of loss, both valves will automatically closed (spring assisted solenoid valves), preventing gas from venting uncontrollably. This means that in case of a loss of connection, power to the system can be cut to put it into a safe state	C	B
R3	Loss of Connection to the Data Acquisition System	A loss of connection means that the pressure inside the oxygen line and inside the chamber are no longer known	Probability	Cable management on the field reduces the chance of anyone tripping over cables and accidental disconnection. Loss of connection without external factors remains very unlikely	3	2
			Severity	In case of a connection loss, power to the system can be cut, causing the system to remain in a safe state until connection can be restored. See R2	B	A
R4	Thermal Failure of the Resonator Tip	High temperatures cause a significant reduction of mechanical properties of metals. During heating the resonator may experience wall temperatures up to 400 C in a very small region near the tip. During combustion this temperature will likely rise rapidly. Thermal failure can cause damage to the test setup. Any damage oxidiser line can also cause secondary fires	Probability	Limit of burn time to < 2 seconds, resulting in lower chance of resonance cavity failing from melting or structural weakening due to the high temperature. Resonator is allowed to cool back to ambient temperature before another test is attempted. The resonator is made from 17-4 PH stainless steel. This will begin to anneal at temperatures above 900 C	4	3
			Severity	Blast shielding to limit the spread of debris particularly in direction of testing personnel and bystanders. Additional blast shielding to cover the rear of the test setup	C	B
R5	Tensile Failure of the Resonator	A rapid pressure increase in the chamber could cause tensile failure of the resonator	Probability		3	3
			Severity	Blast shielding to limit the spread of debris particularly in direction of testing personnel and bystanders. Additional blast shielding to cover the rear of the test setup. Sand bags placed downrange of the nozzle	B	A
R6	Unauthorised Personnel Entering the Test Area	When testing on Fellowship Field it is possible that unauthorised personnel enter the testing area, despite the presence of demarcations. This could be hazardous for the persons approaching.	Probability	Multiple corner guards to ensure that bystanders are aware of the test and who can stop people from entering the restricted area. Bystanders are informed of when dangerous activities begin. Countdowns shall go to a HOLD in case someone is in parking lot	4	1
			Severity		C	C
R7	Secondary fires on the Fellowship field after ignition	Hot exhaust from combustion can set fire to dry grass on Fellowship field. Additionally flammable items left near the setup can contribute to this hazard.	Probability	All flammable items not needed for the test are cleared from the test setup prior to starting final pre-fire procedures. On especially dry conditions, the grass downrange of the exhaust nozzle is dowsed with water before testing	3	1
			Severity	A fire extinguisher and water bucket must be present on the field during the test	C	B
R8	Overpressure in combustion chamber leading to flash back into the propellant lines	A high pressure differential over the injector of both oxygen and methane prevents combustion propagating upstream into the propellant supply lines. If the chamber pressure rises unexpectedly, ignition could propagate upstream, potentially causing the destruction of the test setup and release of shrapnel.	Probability	Check valves are placed on both the oxygen and methane lines just upstream of the injector (see figure 1 in the Dragonfly_CombustionProcedures document). These prevent flow upstream in case of an adverse pressure gradient.	3	2
			Severity	Blast shielding to limit the spread of debris particularly in direction of testing personnel and bystanders. Additional blast shielding to cover the rear of the test setup.	C	B

R9	Overpressure leading to the failure of the Nozzle	A failure of the exhaust nozzle can cause shrapnel to be ejected in the direction of the L&M building.	Probability		3	3
			Severity	Two sand bags placed downrange of the nozzle exhaust to catch ejected shrapnel	C	B
R10	Methane leak leading to secondary fires on the test setup or Fellowship Field	Leak in the methane feed system through improper assembly or a damaged connector. This can result in an increased risk of secondary fires, causing significant damage to the test setup	Probability	Each feed system connection is visually inspected for damage or anomalies before the test begins. The feed system is tested for leaks under operational pressure on fellowship field on the day of the test.	4	2
			Severity	Type ABC fire extinguisher and a water bucket are present on the field during testing	B	B

G

Test Procedures

Experimental procedures were written for both the thermo-acoustic heating and combustion tests. These are necessary to ensure the safe operation of the test setup during experiments and that all of the operational mitigation strategies suggested in [Appendix F](#) are implemented properly. The hazards with the system mainly revolve around the use of high pressure gases, in the form of a strong oxidiser (oxygen), a highly flammable gas (methane) and an asphyxiating gas (nitrogen). The procedures also serve as an indication of which risks are present in each section and which personal protective equipment is required for personnel near the test setup.

The procedures start with a instructions for setting up the system, including setup of the valve control and data acquisition, as well as a basic check of the electrical system (checklists A and B). The propellant feed system is first leak tested under operational pressure using nitrogen. This ensures that no oxygen or methane leaks are present once those gases are introduced. This leak testing is performed in steps of 10 bar and 30 bar on both propellant lines in checklist C. Once no more leaks are found in the system, the methane cylinder is attached to the methane line, and the CGR is set to operational pressure. The same is done for the oxygen side. Note that for the final leak testing on the oxygen side (around the gas regulator) an oxygen compatible leak detection agent is used. Checklist D describes the steps taken for each ignition test. These include the final preparation before a firing attempt, as well as contingencies in the case of off-nominal operation of the system. In between different tests the set pressure of the regulators or the nozzle gap spacing may be adjusted. The steps necessary to put the system into a safe state and to make the relevant changes are detailed in checklist E. The full depressurisation of the system is outlined in checklist F.

COMBUSTION TEST PROCEDURES

Test ID: Combustion Test 1
Project Dragonfly

Thursday 21st March, 2024

Test Location:

Fellowship Field
Anthony Fokkerweg
2629 HS Delft

SO: Jan Struziński
TC: Miguel Castro Gracia
TO: Jonathan Neeser
CP: Nick Eichman

Accompanying Documents:

Document ID	Version	Approved By SO
Dragonfly_CombustionProceduresV1.0	1.0	Roderick Wassenaar
Dragonfly_RiskMapV1.1	1.1	Roderick Wassenaar
Dragonfly_TestApplicationV1.1	1.1	Roderick Wassenaar

Authors:

Jonathan Neeser

Version:

V 1.0

TU Delft emergency: +31 (0) 15 27 81226
Non-emergency: +31 (0) 15 27 82777

Low risk	Medium risk	High risk
<ul style="list-style-type: none"> • Test-setup is safe to approach • No safety gear required 	<ul style="list-style-type: none"> • Only authorized personnel in test area • Wear appropriate safety gear 	<ul style="list-style-type: none"> • Clear all personnel from test area • Do not approach the test-setup



Abbreviations

BV	Bleed Valve (NO)	O2	Oxygen (gaseous)
CGR	Compressed Gas Regulator	NC	Normally Closed
CP	Command Post	NO	Normally Open
CV	Check Valve	SO	Safety Officer
DAQ	Data AcQuisition	PPS	Piezoelectric Pressure Sensor
PV	Purge Valve	PS	Pressure Sensor
MV	Main Valve (NC)	TC	Test Conductor
N2	Nitrogen (gaseous)	TO	Test Operator

Mitigation Strategies

Most important mitigation strategies identified in the risk map document. To be filled in by SO on the test day, once the relevant strategy has been implemented.

Measure	SO Signature After Inspection
ABC fire extinguisher is present on the field	
Blast shielding placed over the setup	
Blast shielding covering the rear of the setup	
A check valve is mounted on both oxygen and methane line	
Sandbag placed downrange of the nozzle	

In case of emergency: +31 (0) 15 27 81226

Test Location:
Fellowship Field
Anthony Fokkerweg
2629 HS Delft

Thursday 21st March, 2024
Project Dragonfly
Test ID: Combustion Test 1

cRIO Pinout

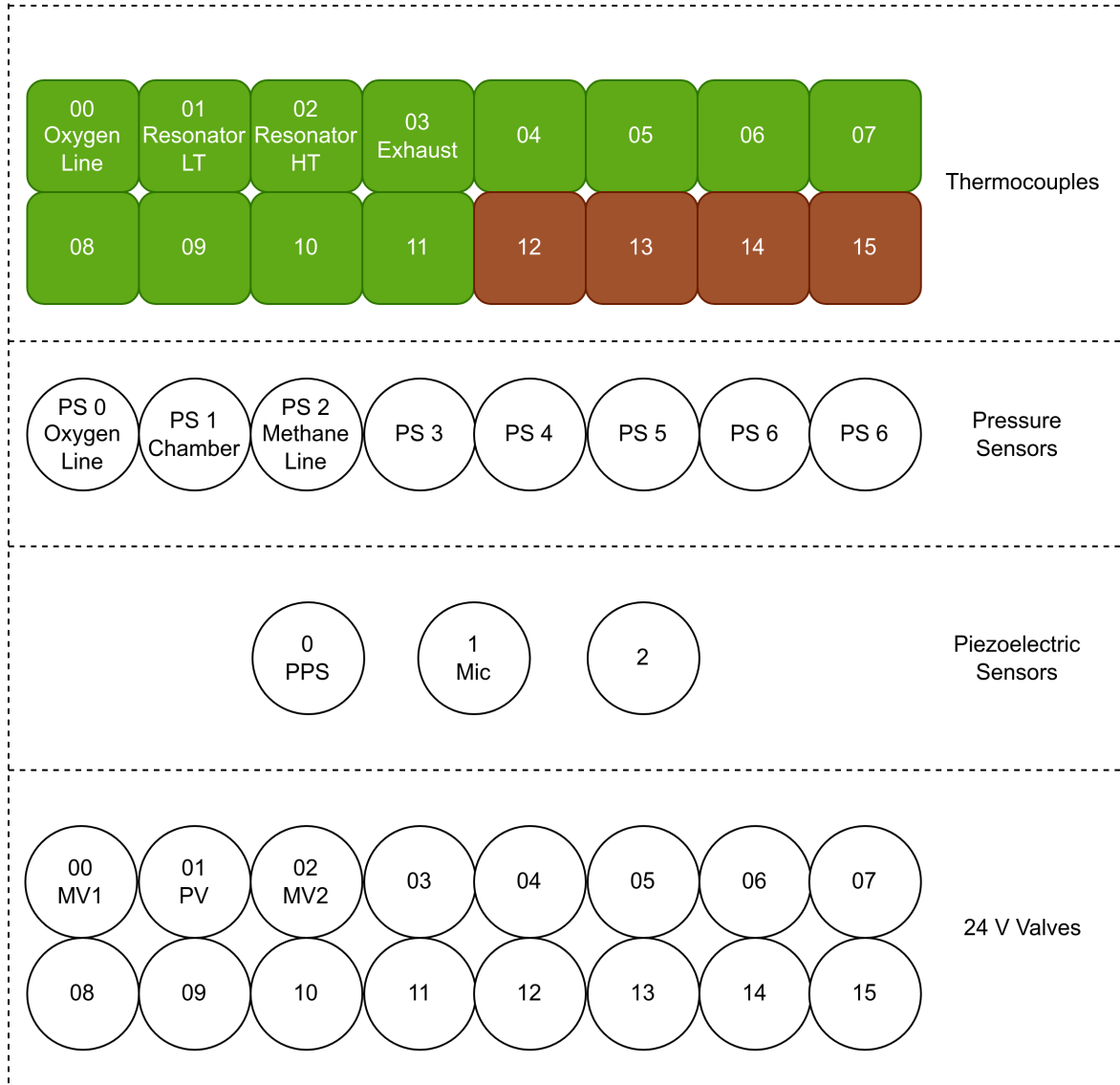


Figure 1: Pinout of the cRIO

Change Log

Version	Comment	Author	Date
1.0	Document adapted from heating procedures	J. Neeser	05.04.2024

In case of emergency: +31 (0) 15 27 81226

Test Location:
Fellowship Field
Anthony Fokkerweg
2629 HS Delft

Thursday 21st March, 2024
Project Dragonfly
Test ID: Combustion Test 1

A - Initial Setup			
ID	Check	Description	Comments
A1		Place 3 pallets on the field	1x Test Bench, 1x RIO, 1x Bottles
A2		Setup pyro tent over the pallets	Install max. 2 sides and into the wind
A3		Close entrances to field using red & white tape	
A4		Place generator	
A5		Hammer grounding pin deep into the ground and connect to generator	
A6		Lead one extension cord from generator to test setup and one to CP	No connectors in the mud!
A7		Lead RIO Ethernet cable from CP to setup	No connectors in the mud!
A8		Ensure that at least 2 filled sandbags are present	If not, use the shovel to fill them
A9		Fill empty bucket with water	
A10		Make sure a fire extinguisher is placed half way between CP and the test setup	
A11		Lay the nitrogen, oxygen and methane bottles on pallet	
A12		Connect high pressure nitrogen CGR to nitrogen bottle	
A13		Verify nitrogen CGR is closed	
A14		Verify nitrogen CGR valve is closed	
A15		Verify that there is no debris or dirt on the oxygen CGR sealing surface	If some is found, clean surface with isopropanol
A16		Connect oxygen CGR to oxygen bottle	
A17		Verify oxygen CGR is closed	
A18		Verify oxygen CGR valve is closed	
A19		Attach nitrogen CGR to main line flex hose	
A20		Connect methane CGR to methane bottle	
A21		Verify methane CGR is closed	
A22		Verify methane CGR valve is closed	
A23		Attach methane CGR to main line flex hose	
A24		CP: Open text file to log important events	keep a timestamp for each entry
A25		Secure test bench with 4 ground pegs	
A26		Verify RIO is SAFE	
Continued			

In case of emergency: +31 (0) 15 27 81226

Test Location:
Fellowship Field
Anthony Fokkerweg
2629 HS Delft

Thursday 21st March, 2024

Project Dragonfly
Test ID: Combustion Test 1

ID	Check	Description	Comments
A27		Connect RIO power cable	
A28		Connect RIO and CP	
A29		CP: Check connection to RIO	
A30		Refer to figure 1 on page 2 for an overview of the cRIO sensor and actuator connections	
A31		Connect TC0 cable to port	Oxygen line near check valve
A32		Connect TC1 cable to port	resonator tip high temperature
A33		Connect TC2 cable to port	resonator tip low temperature
A34		Connect Oxygen PS cable to port PS0	
A35		Connect Chamber cable to port PS1	Make sure standoff is included!
A36		Connect Microphone to RIO	VIB1
A37		Connect main valve 1 to RIO	24V port 0
A38		Connect the purge valve to RIO	24V port 1
A39		Connect main valve 2 to RIO	24V port 2
A40		Check that all fittings on the oxygen line are hand tight	
A41		Check that all fittings on the methane line are hand tight	
A42		Check that all fittings on the purge line are hand tight	
A43		CP: Mark down time of end system setup in log	
A44		Mark down time of end system setup	
<p>System Status:</p> <ul style="list-style-type: none"> • Test setup is fully assembled and secured • Nitrogen bottle is connected but closed • Oxygen bottle is closed • Methane bottle is connected but closed • RIO is connected and powered • RIO is SAFE 			

In case of emergency: +31 (0) 15 27 81226

Test Location:
Fellowship Field
Anthony Fokkerweg
2629 HS Delft

Thursday 21st March, 2024
Project Dragonfly
Test ID: Combustion Test 1

B - System Checkout			
ID	Check	Description	Comments
B1		CP: Fill in correct pressure sensor calibration data	1. PS offset: -24 2. PS slope: 6250
B2		Ask CP to call out pressure sensor values	Should all read ~0.8-1.2bar
B3		Ask CP to call out thermocouple values	Should all read ambient
B4		Heat up each TC with a finger sequentially and check if number matches physical location	
B5		Set RIO to ARMED	
B6		Ask CP to cycle main valve 1 while holding valve to confirm actuation	
B7		Ask CP to cycle main valve 2 while holding valve to confirm actuation	
B8		Ask CP to cycle purge valve while holding valve to confirm actuation	
B9		CP: Start data logging	
B10		Ask CP to perform nominal firing sequence while holding the MV and PV while listening to confirm firing sequence is correct.	
B11		Turn DAQ logging off	
B12		CP: Restart data logging in new file	
B13		Take pictures of the entire setup before continuing!	<input type="checkbox"/> Thermocouple locations <input type="checkbox"/> Cable management/layout <input type="checkbox"/> Cables inserted in the cRIO <input type="checkbox"/> Detailed pictures of chamber
B14		CP: Mark down time of end system checkout in log	
Continued			

In case of emergency: +31 (0) 15 27 81226

Test Location:
Fellowship Field
Anthony Fokkerweg
2629 HS Delft

Thursday 21st March, 2024

Project Dragonfly
Test ID: Combustion Test 1

ID	Check	Description	Comments
<p>System Status:</p> <ul style="list-style-type: none"> • Test setup is fully assembled and secured • Nitrogen bottle is connected but closed • Oxygen bottle is closed • Methane bottle is connected but closed • RIO is connected and powered • RIO is ARMED • Valves are operational • Sensors are calibrated and give correct values 			

C - Leak Testing			
ID	Check	Description	Comments
C1		Announce that 10 bar pressure test of the oxygen line will begin	using nitrogen
C2		Verify that everyone near the test setup is wearing safety glasses	
Low pressure testing			
C3		Physically check all connectors if they are tight	
C4		CP: Make sure that MV 1 is closed	
C5		Verify that nitrogen CGR and CGR Valve are closed	
C6		Open nitrogen bottle	
C7		Ask CP to record pressure of nitrogen bottle	
C8		Check nitrogen CGR connection with leak detection fluid	
C9		<p>If leaks found continue, otherwise skip to C10:</p> <ol style="list-style-type: none"> 1. Close the nitrogen bottle 2. Open N2 CGR 3. Open N2 CGR Valve 4. Close CGR and CGR Valve 5. Fix leak 6. Return to C6 	
C10		Set nitrogen CGR to 10 bar	
C11		Check for leaks using leak detection spray	
C12		Open nitrogen CGR valve	System is now pressurised up to MV 1
C13		Check for leaks with leak detection spray	
Continued			

In case of emergency: +31 (0) 15 27 81226

Test Location:
Fellowship Field
Anthony Fokkerweg
2629 HS Delft

Thursday 21st March, 2024
Project Dragonfly
Test ID: Combustion Test 1

ID	Check	Description	Comments
C14		If leaks found continue, otherwise skip to C15: 1. Close the nitrogen CGR valve 2. Carefully open DV 1 3. Wait until pressure returns to ambient 4. Close DV 1 5. Fix leak 6. Return to C12	
High pressure testing			
C15		Announce that 25 bar pressure test will begin	
C16		close N2 CGR Valve	
C17		Set nitrogen CGR to 25 bar	
C18		Check for leaks using leak detection spray	
C19		Open nitrogen CGR valve	System is now pressurised up to MV 1
C20		Check for leaks with leak detection spray	
C21		If leaks found continue, otherwise skip to C22: 1. Close the nitrogen CGR valve 2. Carefully open DV 1 3. Wait until pressure returns to ambient 4. Close DV 1 5. Fix leak 6. Return to C19	
C22		Close nitrogen bottle	
C23		Carefully open DV 1	
C24		Carefully remove oxygen line from N2 CGR	Make sure the line stays clean
C25		Remove N2 CGR from the nitrogen bottle	
C26		Move N2 bottle aside and replace it with oxygen bottle	
Leak Testing of Purge Line			
C27		Announce that 15 bar pressure test of the purge line will begin	
C28		Mount low pressure N2 CGR on N2 bottle	
C29		Verify that low pressure CGR and CGR Valve are closed	
C30		Open Nitrogen bottle	
C31		Check Nitrogen CGR connection with leak detection spray	
C32		Set low pressure nitrogen CGR to 15 bar	
Continued			

In case of emergency: +31 (0) 15 27 81226

Test Location:
Fellowship Field
Anthony Fokkerweg
2629 HS Delft

Thursday 21st March, 2024

Project Dragonfly
Test ID: Combustion Test 1

ID	Check	Description	Comments
C33		Check for leaks using leak detection spray	
C34		Open low pressure nitrogen CGR valve	System is now pressurised up to PV
C35		Check for leaks with leak detection spray	
C36		If leaks found continue, otherwise skip to C39: 1. Close the low pressure nitrogen CGR valve 2. Ask CP to open PV 3. Wait till pressure returns to ambient 4. Ask CP to close PV 5. Fix leak 6. Return to C34	
C37		Close N2 CGR valve	System is now pressurised up to PV
C38		Announce that 10 bar pressure test of the methane line will begin	
Low pressure testing			
C39		CP: Make sure that MV 2 is closed	
C40		Verify that methane CGR and CGR Valve are closed	
C41		Open methane bottle	
C42		Ask CP to record pressure of methane bottle	
C43		Check methane CGR connection with leak detection spray	
C44		If leaks found continue, otherwise skip to C45: 1. Close the methane bottle 2. Open CH4 CGR 3. Open CH4 CGR Valve 4. Close CGR and CGR Valve 5. Fix leak 6. Return to C41	
C45		Set methane CGR to 10 bar	
C46		Check for leaks using leak detection spray	
C47		Open methane CGR valve	System is now pressurised up to MV 2
C48		Check for leaks with leak detection spray	
Continued			

In case of emergency: +31 (0) 15 27 81226

Test Location:
Fellowship Field
Anthony Fokkerweg
2629 HS Delft

Thursday 21st March, 2024
Project Dragonfly
Test ID: Combustion Test 1

ID	Check	Description	Comments
C49		If leaks found continue, otherwise skip to C50: 1. Close the methane CGR valve 2. Carefully open DV 2 3. Wait till pressure returns to ambient 4. Close DV 2 5. Fix leak 6. Return to C47	
High pressure testing			
C50		Announce that 25 bar pressure test will begin	
C51		close CH4 CGR Valve	
C52		Set methane CGR to 25 bar	
C53		Check for leaks using leak detection spray	
C54		Open methane CGR valve	System is now pressurised up to MV 1
C55		Check for leaks with leak detection spray	
C56		If leaks found continue, otherwise skip to C57: 1. Close the methane CGR valve 2. Carefully open DV 2 3. Wait till pressure returns to ambient 4. Close DV 2 5. Fix leak 6. Return to C54	
C57		Close CH4 CGR valve	System is now pressurised up to MV2
C58		Announce that 10 bar pressure test of the oxygen line will begin	Using oxygen
C59		Ensure that oxygen rated leak detection fluid is present	snoop
Low pressure testing			
C60		Connect oxygen line to the oxygen CGR	
C61		Physically check all connectors if they are tight	
C62		CP: Make sure that MV 1 is closed	
C63		Verify that oxygen CGR and CGR Valve are closed	
C64		Open oxygen bottle	
C65		Ask CP to record pressure of oxygen bottle	
C66		Check oxygen CGR connection with leak detection fluid	
Continued			

In case of emergency: +31 (0) 15 27 81226

Test Location:
Fellowship Field
Anthony Fokkerweg
2629 HS Delft

Thursday 21st March, 2024

Project Dragonfly
Test ID: Combustion Test 1

ID	Check	Description	Comments
C67		If leaks found continue, otherwise skip to C68: 1. Close the oxygen bottle 2. Open O2 CGR 3. Open O2 CGR Valve 4. Close CGR and CGR Valve 5. Fix leak 6. Return to C64	
C68		Set oxygen CGR to 10 bar	
C69		Check for leaks using leak detection fluid	
C70		Open oxygen CGR valve	System is now pressurised up to MV 1
C71		Check for leaks with leak detection fluid	
C72		If leaks found continue, otherwise skip to C73: 1. Close the oxygen CGR valve 2. Carefully open DV 1 3. Wait till pressure returns to ambient 4. Close DV 1 5. Fix leak 6. Return to C70	
High pressure testing			
C73		Announce that 25 bar pressure test will begin	
C74		close O2 CGR Valve	
C75		Set oxygen CGR to 25 bar	
C76		Check for leaks using leak detection fluid	
C77		Open oxygen CGR valve	System is now pressurised up to MV 1
C78		Check for leaks with leak detection fluid	
C79		If leaks found continue, otherwise skip to C80: 1. Close the oxygen CGR valve 2. Carefully open DV 1 3. Wait till pressure returns to ambient 4. Close DV 1 5. Fix leak 6. Return to C77	
C80		Close O2 CGR valve	System is now pressurised up to MV1
C81		Take pictures of the entire setup	
C82		CP: Mark down time of end leak testing in log	
C83		Mark down time of end leak testing	
Continued			

In case of emergency: +31 (0) 15 27 81226

Test Location:
Fellowship Field
Anthony Fokkerweg
2629 HS Delft

Thursday 21st March, 2024

Project Dragonfly
Test ID: Combustion Test 1

ID	Check	Description	Comments
<p>System Status:</p> <ul style="list-style-type: none"> • All leaks have been fixed • All systems are checked out and are proven to work • Oxygen CGR is set to 25 bar and the CGR valve is closed • Nitrogen CGR is set to 15 bar and the CGR valve is closed • Methane CGR is set to 25 bar and the CGR valve is closed • Oxygen line is pressurised to 25 bar • Low pressure line is pressurised to 15 bar • Methane line is pressurised to 25 bar 			



D - Ignition Test			
ID	Check	Description	Comments
D1		CP: Mark down technical details of this test in the log	if applicable, also include changes made w.r.t. last attempt
D2		Verify that MV 1 is closed	
D3		Verify that MV 2 is closed	
D4		Verify that PV is closed	
D5		CP: Check valve timing 1. MV 1: OPEN at T+0s, CLOSE at T+16s 2. MV 2: OPEN at T+14s, CLOSE at T+16s 3. PV: OPEN at T+16s, CLOSE at T+18s	
D6		Start cameras	
D7		Place Shrapnel Box over the system	
D8		Announce to bystanders that ignition tests will soon commence	
D9		Open oxygen CGR valve	
D10		Open nitrogen CGR valve	
D11		Open methane CGR valve	
D12		Retreat in a controlled and distinctive manner	
D13		CP: Stop and restart LabVIEW program	
D14		CP: Arm automated sequence	
D15		SO verify that the field is secure	
D16		Ask SO for final go	
D17		Ask TC for final go	
D18		Ask TO for final go	
System is ready			
Continued			

In case of emergency: +31 (0) 15 27 81226

Test Location:
Fellowship Field
Anthony Fokkerweg
2629 HS Delft

Thursday 21st March, 2024

Project Dragonfly
Test ID: Combustion Test 1

ID	Check	Description	Comments
 			
D19		TC: Start countdown from t-15	
D20		CP: Start data-logging	Start at ~ 12 seconds
D21		CP: Start firing sequence	Start at 10 seconds
Igniter is firing			
D22		CP: Stop highspeed data logging	
D23		CP: Verify that MV1, MV2 and PV are closed	
D24		CP: call out pressure and system temperature	
D25		Wait for 1 min or until resonator tip is below 100 °C	
D26		Approach test setup	WARNING: system may be very hot
D27		Stop cameras	
D28		Inspect the system for damage	
D29		Take pictures of the setup	
D30		Use Test Data Analysis script to view test data on the spot	If needed
D31		If performing another burn, assess system state by reviewing produced plots 1. Pressure spectra (for combustion instabilities) 2. Temperature of the resonator tip	
D32		If performing another burn/attempt:	
Discuss possibility of further testing. In case of another test, move to D6 In case the test configuration needs to be changed, move to E1 In case this is the last test, move to F1			

E - Change Nozzle Gap Spacing			
ID	Check	Description	Comments
E1		Close O2 CGR Valve	
E2		Close N2 CGR Valve	
E3		Close CH4 CGR Valve	
E4		Remove shrapnel box	Caution the resonator might still be hot
E5		Loosen the fitting upstream of the oxygen inlet	
Continued			

In case of emergency: +31 (0) 15 27 81226

Test Location:
Fellowship Field
Anthony Fokkerweg
2629 HS Delft

Thursday 21st March, 2024

Project Dragonfly
Test ID: Combustion Test 1

ID	Check	Description	Comments
E6		Loosen the retaining nut on the oxygen inlet	
E7		Rotate the oxygen inlet to the desired position	
E8		Tighten the locking nut on the oxygen inlet	this will fix it in position
E9		Tighten the fitting upstream of the oxygen inlet	
E10		SO: check that the recently adjusted fittings are hand tight	
E11		return to D6	

F - Depressurising			
ID	Check	Description	Comments
F1		Approach the system	
F2		Close O2 bottle	
F3		Close N2 bottle	
F4		Close CH4 bottle	
F5		Carefully open manual DV 1	
F6		Carefully open manual DV 2	
F7		Ask CP to open PV until all gas is vented	
F8		Ask CP to unpower all valves	
F9		Set RIO to SAFE	
F10		Retrieve all data from the RIO	
F11		Retrieve all camera SD cards	
<p>System Status:</p> <ul style="list-style-type: none"> • Chamber assembly may be hot • RIO is SAFE • Oxygen bottle is closed • Methane bottle is closed • Nitrogen bottle is closed • Valves are unpowered • System is depressurised 			
F12		Detach Nitrogen bottle	
F13		Detach Oxygen bottle	
F14		Detach Methane bottle	
F15		Return bottles to L&M	
F16		Pack up and debrief!	

In case of emergency: +31 (0) 15 27 81226

Test Location:
Fellowship Field
Anthony Fokkerweg
2629 HS Delft

Thursday 21st March, 2024

Project Dragonfly
Test ID: Combustion Test 1